University of Alberta

The Experimental Investigation of the Effect of Chamber Length on Jet Precession

by

Adam Martin Madej

A thesis submitted to the Faculty of Graduate Studies and Research
in partial fulfillment of the requirements for the degree of

Master of Science

Department of Mechanical Engineering

Fall 2010
Edmonton, Alberta

Examining Committee

David S. Nobes (Supervisor), Mechanical Engineering

C. R. (Bob) Koch, Mechanical Engineering

Suzanne M. Kresta, Chemical and Materials Engineering

ABSTRACT

The effect of chamber length and Reynolds number on the stability and behavior of the flow field generated by a precessing jet nozzle was studied using stereoscopic particle image velocimetry (StereoPIV). An algorithm was developed to determine the mode of the flow based on the distribution of axial velocity. The optimal chamber length for precession to occur was found to be between 2 and 2.75 chamber-diameters. There is no precession at a chamber length of one diameter, and the occurrence of precession was found to be strongly related to Reynolds number. Conditionally averaged velocity distributions for the flow in precessing mode were calculated.

The effect of initial condition on downstream behavior of axisymmetric jets was examined. Variations in spread and decay rates were found for jets issuing from different nozzles. Self-similar solutions for axisymmetric jets are therefore not universal, and are instead dependent upon initial conditions at the source.

TABLE OF CONTENT

LIST OF TABLES

LIST OF FIGURES

LIST OF NOMENCLATURE

Latin Symbols

A_c	Area of chamber exit [mm^2]
A_j	Cross sectional area of jet along light-sheet plane [mm^2]
A_n	Area of nozzle exit [mm^2]
B	Original coordinate system basis
B'	Rotated coordinate system basis
d	Nozzle exit diameter [mm]
D	Precession chamber diameter [mm]
D_s	Supply pipe diameter [mm]
E	Entrainment ratio of fluid into the precession chamber
$f(\eta)$	Arbitrary function of length scale, η, representing radial variation of $U(x,r)$
$g(\eta)$	Arbitrary function of length scale, η, representing radial variation of $\tau(x,r)$

$F_{1,2,3}, G$	Arbitrary functions of a single length-scale used in the self-similarity derivation
$\mathbf{f}$	Boolean array of size $I \times J$. True if there is positive axial velocity, false otherwise.
i, j	Positional indices of arrays
i', j'	Positional indices of arrays after rotation
i_0	Streamwise offset between two vector fields
I, J	Vector field size in grid points
$\mathbf{I_n}$	Intensity distribution of nth image on camera CCD plane [intensity counts]
$\mathbf{I'_n}$	Intensity distribution of nth image on camera CCD plane after image preprocessing step [intensity counts]
K_1	Centerline velocity decay coefficient
K_2	Jet half-width coefficient
j_0	Spanwise offset between two vector fields
L	Precession chamber length [mm]

L_d	Development length of long pipe nozzle [mm]
m	Fraction of light sheet thickness through which a particle is desired to pass
$\dot{m}_0$	Initial mass flow rate out of jet nozzle [kg/s]
$\dot{m}_{in}, \dot{m}_{out}$	Mass flow into and out of the precession chamber [kg/s]
M	Magnification between image plane and camera CCD plane [mm/px]
$\dot{M}_0$	Initial momentum flux [kg·m/s²]
n	Index number of image/vector field
N	Number of images/vector fields in a dataset (i.e. at a given Reynolds number and inlet condition/chamber length)
N_{PJ}, N_{AJ}	Number of vector fields in precessing mode and axial mode.
$\mathbf{P}$	Transformation matrix between coordinate bases, used for velocity component array rotation
P_{PJ}	Probability of precession mode
$p(x, r, \theta)$	Pressure distribution [Pa]

$q_{1,2}$	Volume flow rate through inner and outer areas of precession chamber [m^3/s]
Q	Volume flow rate of working fluid through system [L/min]
r,θ	Positional coordinates in cylindrical coordinates [mm, rad]
$\tilde{r},\tilde{\theta}$	Location of jet centroid in cylindrical coordinates [mm, rad]
$\delta r,\delta\theta$	Grid spacing of positional coordinate arrays $\mathbf{R}$ and $\mathbf{\Theta}$ [mm, rad]
R	Precession chamber radius [mm]
R_c	Cutoff radius used for precession mode finding [mm]
$\overline{R}_c$	Average cutoff radius [mm]
$R_s(x)$	Characteristic scale for Reynolds stress in axial-radial direction $[\mathrm{kg/m\cdot s^2}]$
$\mathbf{R},\mathbf{\Theta}$	Positional coordinate arrays in cylindrical coordinates [mm, rad]
Re	Reynolds number based on the nozzle exit diameter
$\vec{s}$	Position vector [mm]
s,t	Position indices for arrays in cylindrical coordinate system

Δt	Time step between two successive image frames [μs]
t_0	Reference time [s]
T	Light sheet thickness [mm]
u, v, w	Instantaneous velocity components [m/s]
$\mathbf{u}, \mathbf{v}, \mathbf{w}$	$I \times J$ arrays containing instantaneous u, v, and w velocity components [m/s]
$\vec{u}$	Velocity vector [m/s]
u', v', w'	RMS velocity components [m/s]
$\mathbf{u}', \mathbf{v}', \mathbf{w}'$	$I \times J$ arrays containing RMS velocity components [m/s]
U, V, W	Averaged velocity components [m/s]
$\mathbf{U}, \mathbf{V}, \mathbf{W}$	$I \times J$ arrays containing instantaneous u, v, and w velocity components [m/s]
$U_{cl}(x)$	Axisymmetric jet centerline velocity at axial distance x from nozzle [m/s]
U_0	Axisymmetric jet centerline velocity at nozzle exit [m/s]
$U_s(x)$	Characteristic scale for axial velocity [m/s]

$\breve{\mathbf{w}}$	Axial velocity field array after data masking [m/s]
$\mathbf{w_{cyl}}$	Axial velocity field, in cylindrical coordinates [m/s]
$\mathbf{w_{rot}}$	Rotated axial velocity field array [m/s]
$\vec{x}$	Position vector [mm]
x, y	Positional coordinates [mm]
$\hat{x}, \hat{y}$	Unit vectors in the coordinate system before rotation [mm]
x', y'	Positional coordinates in rotated image plane [mm]
$\hat{x}', \hat{y}'$	Unit vectors in the rotated coordinate system [mm]
x_i, y_j	Positional coordinates x and y at discretized grid positions i and j [mm]
x_c, y_c	Position of chamber center [mm]
$x_{o,1}$	Position of virtual origin determined from centerline velocity decay [mm]
$x_{o,2}$	Position of virtual origin determined from jet half-velocity [mm]
x_p	Length of potential core [mm]

$\delta x, \delta y$	Grid spacing of *x*- and *y*-coordinate arrays [mm]
$\Delta x, \Delta y, \Delta z$	Particle displacements in real-world coordinates [mm]
$\Delta x'$	Mapped particle displacement onto a plane parallel to the camera CCD plane [mm]
$\mathbf{X}, \mathbf{Y}$	Arrays containing positional coordinates [mm]
$y_{1/2}$	Axisymmetric jet half-width [mm]

Greek Symbols

α	Angle between camera and jet centerline [deg]
γ_c	Ratio between the cross sectional area of the jet and the chamber exit area
$\delta(x)$	Arbitrary length scale [mm]
η	Nondimensionalized spanwise position coordinate
λ_0	Chamber radius [px]
ν	Kinematic viscosity [m^2/s]
ξ, ψ	Positional coordinates on camera CCD plane [px]

ξ_0, ψ_0	Position of chamber center on camera CCD plane [px]
$\Delta\xi$	Pixelwise displacement on camera CCD plane [px]
$\Delta\xi_0$	Desired pixelwise displacement on CCD plane (one-quarter of interrogation window size) [px]
Ξ, Ψ	Size of camera CCD array [px]
ρ	Fluid density [kg/m³]
$\sigma_{\overline{R}_c}$	Standard deviation in cutoff radius [mm]
$\tau(x,r) = -\rho\overline{u'v'}$	Simplification term used in the derivation of the self-similar solutions for the axisymmetric jet [$\mathrm{kg}/\mathrm{m}\cdot\mathrm{s}^2$]
υ_e	Bulk inlet velocity [m/s]
ϕ	Angle formed between y^+-axis and position of highest outflow in precessing jet axial velocity field [rad]
χ	Nondimensionalized axial position coordinate for the axisymmetric jet
θ_0	Angular position from which coordinate system mapping from Cartesian to cylindrical begins [rad]

Ω ....Pump rotation speed [rpm]

Mathematical Symbols

$\forall$ ....For all values of…

э ....Such that…

Abbreviations

AJ ....Axial jet mode

FOV............................Field of view

LP ....Long pipe

OP ....Orifice

PJ ....Precessing jet mode

ROI............................Region of interest

RMS ....Root mean square

SC...............................Smooth contraction

PIV ....Particle image velocimetry

StereoPIV...................Stereoscopic particle image velocimetry

CHAPTER 1: INTRODUCTION

1.1 Introduction

Jets are devices used in engineering practices to mix and transport fluids (White, 2003). The mixing field may be reacting, as in combustion processes, or non-reacting. In the former case, the type of mixing can affect the performance of combustion (Newbold, 1997). Research has shown that the properties of the nozzle can be used to passively control the fluid mixing in the region where the reaction occurs, thereby allowing for the control of combustion. Precessing jets (Nathan, 1998) are a class of these devices, which have been shown to greatly increase mixing in their near field (Wong et al., 2003) and have found applications in industrial burners (Manias, 1994; Manias et al., 1996). Further research of the flow phenomenon generated by a precessing jet is needed to fully understand these flows and allow for their optimal design.

1.2 The Precessing Jet

In its simplest form, a precessing jet refers to an axisymmetric jet flow issuing through a nozzle-chamber assembly, as shown in Figure 1.1. This is the basic configuration shown by Nathan et al. (1998). The flow exits through a nozzle of diameter d through a sudden expansion into a chamber of inner diameter D and length L. If these dimensions are appropriately chosen, the flow may destabilize, resulting in a precessing flow, where the axis of the issuing jet rotates about the chamber axis (Nathan et al., 1998). The optimal dimensions to generate this instability have been found to be

$L/D = 2.75$, with precession occurring over the range $2 \le L/D \le 3.5$ (Newbold, 1997), and an expansion ratio of $D/d = 5$ (Nathan et al., 1998). This flow is bistable, intermittently and chaotically switching between this precessing mode (PJ mode) and an axial mode (AJ mode), where the exiting jet closely resembles an axisymmetric jet. This flow differs from a swirl flow, where the jet is rotating about its own axis. Instead, the axis of the jet is rotating about the axis of the chamber in a gyroscopic-like motion. Similar configurations with non-circular nozzles have been shown to exhibit flapping behavior (Mi et al., 2001c), where the position of the jet moves around the chamber exit plane. The motion is however not rotational in nature and therefore not considered to be precessing.

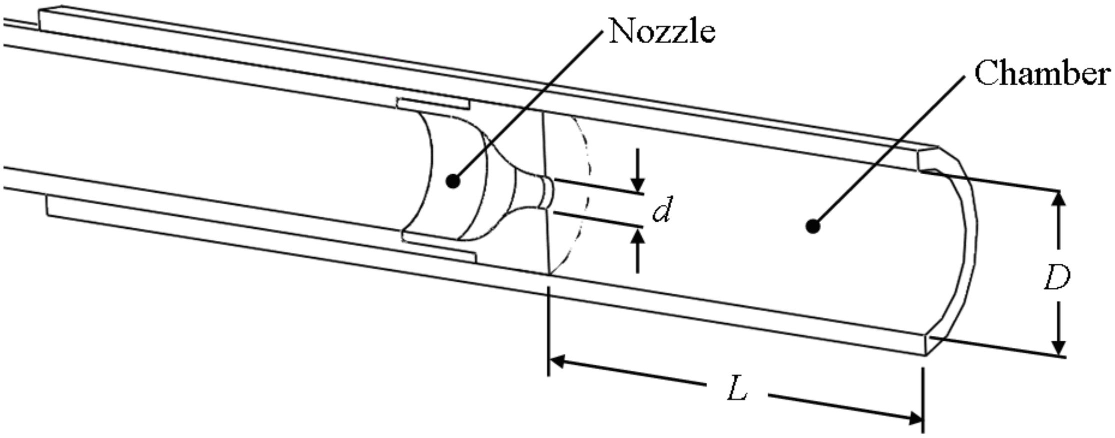

Figure 1.1 Sectioned view of a precessing jet nozzle in its simplest configuration (without a lip or center body), showing relevant dimensions and components.

The flow field of a precessing jet enhances mixing downstream from its nozzle, with the velocity decaying more rapidly than its axisymmetric counterpart (Wong et al., 2003). This flow instability has found applications in industrial processes, such as industrial burners (Manias, 1994). Use of precessing nozzles has shown improvement in flame stability, increased burner efficiency, and decreased pollutant emissions (Newbold, 1997). The use of such nozzles in lime kiln burners has shown increased flame luminosity resulting in increased radiant heat transfer, while reducing the flame temperature, which in turn reduces NO_x production. Such installations have shown 5-20% reductions in specific fuel consumption, 5-10% increases in kiln output, and 40-70% reductions in NO_x emissions (Manias et al., 1996).

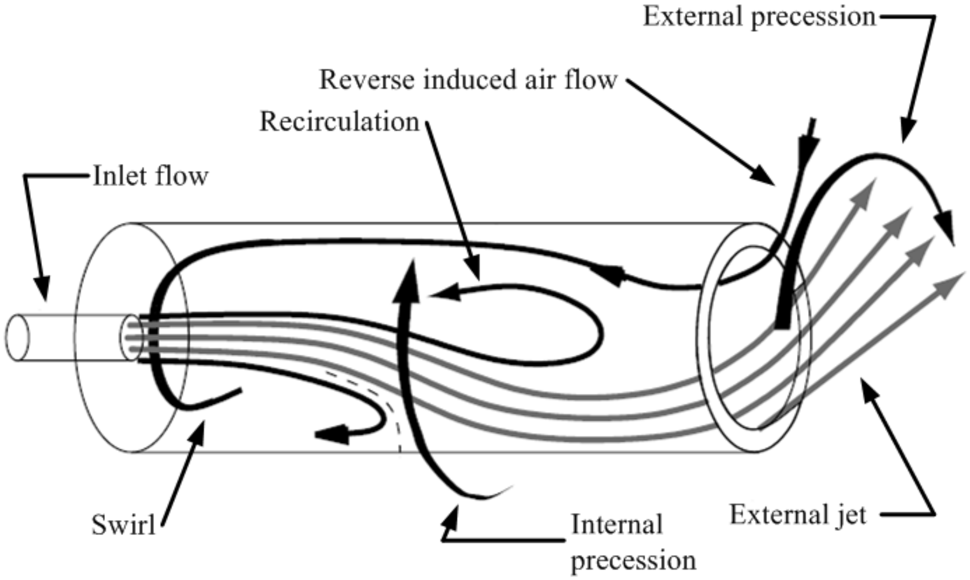

Figure 1.2 Representation of the flow field occurring within and beyond the precession chamber when in precessing flow mode. Reproduced from Wong et al., (2004).

Nathan et al. (1998) give the first thorough description of the mechanics driving this flow phenomenon through their qualitative flow visualization technique, which is illustrated in Figure 1.2. After exiting the nozzle into the chamber, the inlet flow separates as it passes the sudden expansion, spreading as it entrains chamber fluid and then asymmetrically reattaches to the chamber wall. Fluid is drawn from outside of the chamber, inducing a rotating pressure field. This causes the reattaching flow to precess along the inside wall of the chamber, also precessing as it exits the chamber. The transverse pressure gradient causes the jet to deflect, achieving an initial deflection of approximately 50° with the chamber axis, and decreasing to approximately 30° within $x/D = 0.4$ (Wong et al., 2003), where x is the axial distance from the chamber exit. The exiting jet has been shown to be kidney-bean in shape along a plane parallel to the chamber exit and be dominated by a pair of counter-rotating vortices. Beyond an axial distance of $x/D \cong 0.5$, the shape characteristic of precessing mode disappears, and the jet closely resembles an axisymmetric jet flow (Wong et al., 2008).

The nozzle exit condition has an effect on the probability of PJ mode (Wong et al., 2004), with smooth contraction nozzles resulting in lower probability than for long pipe and orifice nozzles. This has been attributed to the symmetry of large scale structures being shed at the nozzle exit plane which directly influence the stability of the downstream flow field within the chamber. The presence of a lip on the chamber greatly increases the dominance of precession mode, while the addition of a centerbody results in a near-unity precession probability, provided that the Reynolds number is sufficiently high and it is mounted upstream of the lip (Wong et al., 2004). The inlet flow condition also has been shown to influence the precession frequency of the jet (Wong et al., 2006), with the orifice nozzle producing the highest precession frequency and the long pipe the lowest.

There have been many studies on the flow field and mechanics of this flow phenomenon. Guo et al. (1999) carried out numerical simulations using the k-ε turbulence model of the downstream flow field of an axisymmetric jet issuing through expansion ratios $3.95 \leq D/d \leq 6$, observing both precession and oscillatory flapping motion. The relationship between precession frequency and chamber length and Reynolds number was studied by Mi and Nathan (2004) with pressure measurements along the nozzle axis using a mechanical analogue for the fluidic precessing nozzle. They found an almost linear increase of precessing frequency with chamber length and jet velocity, and the downstream mixing is strongly influenced by the Strouhal number of the flow. Wong et al. (2003) have performed laser Doppler anemometry (LDA) measurements within and beyond the precession chamber, and observed the asymmetric deflection of the jet and its reattachment to the wall of the chamber. Their methodology, however, was unable to accurately determine entrainment back into the chamber due to seeding losses in the reattachment region. England et al. (2010) used particle image velocimetry (PIV) and frequency measurements to determine the effect of the density ratio of fluid exiting the jet to surrounding fluid on the initial decay and spread of a precessing jet emanating from a triangular nozzle. They showed a strong relationship between the density ratio and the deflection angle of the jet, which directly influences the spread and decay rates, and that there is an inverse relationship between density ratio and precession frequency. Birzer et al. (2009) used planar nephelometry to determine the effect of flow mode (AJ or PJ) on the distribution of pulverized fuel particles used in rotary kilns. A recent study by Wong et al. (2008) took PIV measurements in transverse and longitudinal planes to examine the flow field within the chamber and immediately beyond it using a precession nozzle assembly with both a center body and lip, revealing the in-plane velocity distributions and the existence of pairs of vortical structures.

The mechanics of precessing flow are still, at best, poorly understood. There is no concrete definition of the optimal chamber length to generate precession, nor is there an established relationship between Reynolds number and the probability of this mode occurring. There is no understanding of the effect of these two parameters on the entrainment of surrounding fluid back into the chamber, and how it varies between the two modes of flow, and there is there no data on the appropriate length scale for scaling the flow. To address this, a parametric study is performed on the three-component flow field just beyond the exit plane of the precession at a number of chamber lengths and Reynolds numbers. In addition to the probability of precession, the effect of the two aforementioned parameters on entrainment and the size of the issuing jet is examined.

1.3 The Effect of Initial Conditions on an Axisymmetric, Turbulent Jet

It has been identified in Section 1.2 that the jet entering the precession chamber has an effect on the precession phenomenon and its stability. Therefore, a preliminary study of the effect of initial conditions of the downstream flow field for an axisymmetric jet is appropriate. Traditionally, turbulent free jets have been modeled as point-sources of momentum (Townsend, 1976), yielding self-similar solutions. In these models, it is assumed that sufficiently far downstream, initial conditions are ‘forgotten’, and the jet reaches an asymptotic state.

The flow field of an axisymmetric jet exists in three zones (Rajaratnam, 1976). Closest to its nozzle is the development region, where the jet’s centerline velocity is constant. Within this region is the cone-shaped potential core, in which the fluid velocity is equal to the fluid velocity at the nozzle. Beyond the development region, at the transition zone, the turbulence generated at the jet boundaries reaches the jet centerline, causing the centerline velocity to begin to decay. Downstream from this is the region of fully-developed flow, in which the self-similar solutions are often used to model the flow and predict velocity decay and the spread of the jet.

1.3.1 The Concept of Self-Similarity

To, illustrate the concept of self-similarity, consider an arbitrary function $F(x, y)$, where x and y are independent variables (Pope, 2000). It is possible to define characteristic scales for both the function itself and one of the independent variables which are functions of only the other variable, for example $F_0(x)$ and $\delta(x)$. These scales are appropriate to the system, usually have a power-law dependency on x, and are used to scale $F(x, y)$ and y, respectively. The scaled values are defined in equations (1.1) and (1.2).

$$\eta = \frac{y}{\delta(x)} \tag{1.1}$$

$$\widetilde{F}(x,\eta) = \frac{F(x, y)}{F_0(x)} \tag{1.2}$$

If $\widetilde{F}(x,\eta)$ is no longer a function of x, and instead only a function of η, thereby satisfying equation (1.3), then $F(x, y)$ is self-similar.

$$\widetilde{F}(x,\eta) = \hat{F}(\eta) \tag{1.3}$$

A self-similar solution allows then for $F(x, y)$ to be expressed in terms of a function of a single, independent variable (either x or η), essentially eliminating a dimension from the problem. It is important to note that self-similar behavior may only exist in a finite region of x's domain (George, 1989).

There are different possible forms of self-similarity (George, 1989). The flow may be fully self-similar, where self-similar behavior exists at all scales of motion and in all orders of turbulence moments, partially self-similar, where self-similar solutions exists only for the mean momentum equation and/or certain orders of turbulence moments, or locally self-similar, where only local profiles appear to scale with local quantities.

1.3.2 The Traditional Approach to Self-Similarity in an Axisymmetric Jet

The traditional approach to a self-similar solution for the axisymmetric jet begins with the simplified equations for a round, free jet, presented in equations (1.4) and (1.5). These equations are derived from the Reynolds-averaged Navier-Stokes (RANS) equations and continuity equation in a cylindrical coordinate system given in Appendix A-1. Here, x and r and axial and radial position coordinates, respectively, and U and V are their mean velocity components. The corresponding fluctuating velocity components are u' and v'. It is assumed that there is no swirl in the flow, and therefore there is no azimuthal component of velocity.

$$U\frac{\partial U}{\partial x}+V\frac{\partial U}{\partial r}=-\frac{1}{r}\frac{\partial}{\partial r}\left(r\overline{u'v'}\right) \tag{1.4}$$

$$\frac{\partial U}{\partial x}+\frac{1}{r}\frac{\partial rV}{\partial r}=0 \tag{1.5}$$

For simplicity, $\tau=\tau(x,y)$ is defined in equation (1.6), and represents the momentum associated with the Reynolds stress in the axial-radial direction.

$$\tau(x,r)=\rho\overline{u'v'} \tag{1.6}$$

Multiplying equation (1.4) by ρr, where ρ is the fluid density, and integrating yields the momentum equation for the jet, shown in equation (1.7), which states that the momentum flux must be constant in the axial direction. Integrating with respect to x yields equation (1.8), which is the momentum flux of the jet. Since this value is constant, the jet may be considered as originating from a point source of momentum, instead of a nozzle of finite dimension (Townsend, 1976).

$$\frac{d}{dx}\int_0^\infty 2\pi\rho r U^2 dr = 0 \tag{1.7}$$

$$\dot{M}_0 = \int_0^\infty 2\pi\rho r U^2 dr \tag{1.8}$$

Length scales $\delta = \delta(x)$, $U_{cl} = U_{cl}(x)$, and ρU_{cl}^2 are chosen for r, $U(x,r)$ and $\tau(x,r)$, respectively, which yield self-similar solutions of the form of equations (1.16)-(1.19). U_{cl} is chosen as the centerline velocity of the jet, as it is only a function of axial distance, and δ is an arbitrary length scale, provided that it satisfies a self-similar solution. Functions $f(\eta)$ and $g(\eta)$ account for any variation of $U(x,r)$ and $\tau(x,r)$ in the radial direction.

$$\eta = \frac{r}{\delta(x)} \tag{1.9}$$

$$\frac{U(x,r)}{U_{cl}(x)} = f(\eta) \tag{1.10}$$

$$\frac{\tau}{\rho U_{cl}^2} = g(\eta) \tag{1.11}$$

Equations (1.16)-(1.19) are substituted into equations (1.4) and (1.5). Following the simplifications and substitutions outlined in Appendix A-2, the power-law dependencies of length scales U_{cl} and δ are determined. These are shown in equations (1.12) and (1.13).

$$U_{cl}(x) \sim x^{-1} \tag{1.12}$$

$$\delta(x) \sim x \tag{1.13}$$

The length scales U_{cl} and δ are assumed to have functional dependencies on axial distance, *x*, momentum flux, $\dot{M}_0$ (shown in equation (1.7) to be invariant), and fluid density, ρ. It is assumed that if the flow regime is turbulent, the viscosity of the fluid can be neglected (Rajaratnam, 1976). Therefore, solutions of the form of equations (1.14) and (1.15) are sought.

$$U_{cl} = f\left(x, \dot{M}_0, \rho\right) \tag{1.14}$$

$$\delta = f\left(x, \dot{M}_0, \rho\right) \tag{1.15}$$

Dimensional analysis is performed on equations (1.14) and (1.15), yielding equations (1.16) and (1.17). The full dimensional analysis is presented in Appendix A-3. These equations relate quantities $U_{cl}(x)$ and $\delta(x)$ to axial distance, x. K_1 and K_2 are constants of proportionality, representing the velocity decay rate at the jet centerline and the spread rate of the jet, respectively.

$$U_{cl}(x)\sqrt{\frac{\rho}{\dot{M}_0}} = K_1 \tag{1.16}$$

$$\delta(x) = K_2 x \tag{1.17}$$

One final assumption is made, which allows for the momentum flux, $\dot{M}_0$, to be expressed in terms of the centerline velocity at the nozzle exit, U_0. Since the value of momentum flux is uniform at any axial position, and assuming a uniform velocity distribution throughout the nozzle exit plane, i.e. $U(r,x)\big|_{x=0} = U_0$, $\dot{M}_0$ is related to U_0 by equation (1.18).

$$\dot{M}_0 = \int_0^{d/2} U^2(x,r) r dr = \frac{\pi}{4} d^2 U_0^2 \tag{1.18}$$

It is important to note that the distance *x* is from a conceptualized point-source of momentum and not the true source of momentum, which normally is a nozzle of finite area. Therefore, it is necessary to offset it with the difference in position between the point and true sources of momentum, denoted by x_o, which is the virtual origin position relative to the nozzle ($x \mapsto x - x_o$). This axial distance is now scaled against the nozzle diameter, yielding dimensionless axial velocity χ, which is defined in equation (1.19).

$$\chi \equiv \frac{x - x_o}{d} \tag{1.19}$$

The offset for virtual origin, x_o is applied to equations (1.16) and (1.17), and (1.18) is substituted into (1.16), providing equations (1.20) and (1.21). The constant $\pi/4$ in equation (1.18) is absorbed into K_1 upon substitution. These are the self-similar solutions for the turbulent, axisymmetric jet.

$$\frac{U_0}{U_{cl}(\chi)} = \frac{1}{K_1} \chi \tag{1.20}$$

$$\frac{\delta(x)}{d} = K_2 \chi \tag{1.21}$$

1.3.3 The Effect of Initial Conditions on Self-Similar Behavior

In the self-similar solution derived in the previous section, there is no consideration or mention of the initial condition of the jet. Instead, every jet is modeled as a conceptualized point-source of momentum, disregarding what has happened at the true source, i.e. the nozzle, and after a region of dynamic readjustment, it reaches an asymptotic state. If all jets become asymptotically independent of the initial conditions, then it is obvious that they must all decay at the same rate and exhibit the same shape once an adjustment has been made for the location of the true origin, and these must correspond to the equivalent point source momentum (George, 1989).

George (1989) presents an alternative derivation of the self-similarity, in which he assumes that the momentum flux, which is assumed to originate at a point source, is not the only length scale. Instead, he provides a dimensional analysis considering also the mass flux at the source, $\dot{m}_0$, showing that there are many source-dependant possibilities for K_1 and K_2, which would result in different growth rates for different jets issuing from different nozzles. The derivation presented in his 1989 paper is shown in Appendix B.

The three most commonly encountered nozzles in engineering practices are the smooth contraction, long pipe, and orifice, each differing in the initial condition it provides to its flow field. The smooth contraction results in a 'top-hat' velocity profile, where axial velocity of the issuing jet is nearly uniform across the nozzle exit plane. There is a thin shear layer at the boundary of the nozzle (Mi et al., 2001b), shedding nearly symmetrical, large-scale, vortical structures (Tso and Hussain, 1989). The long pipe produces a '$\bigcap$'-shaped exit velocity profile, which follows a seventh-order polynomial empirical fit, and a thicker shear layer than the smooth contraction. The orifice generates a parabolic exit velocity profile in between that of a smooth contraction and a long pipe, and has been shown by Mi et al. (2007) to exhibit an acceleration of fluid just beyond the nozzle exit in the vena contracta region, as well as have complex and asymmetric vortical structures. These are large-scale, and have been shown to engulf ambient fluid and dominate the initial growth rate of the jet.

There have been a myriad of studies from the literature examining the flow-fields of axisymmetric jets. The most attention has been placed on the smooth contraction nozzle (Wygnanski and Fiedler, 1969; Dahm and Dimotakis, 1987; Cohen and Wygnanski, 1987; Peterson and Bayazitoglu, 1992; Hussein et al. 1994; Weisgraber and Liepman, 1998; Fellouah et al., 2009). There have also been studies using long pipe (Panchapakesan and Lumley, 1993; Papadopoulos and Pitts, 1998; Borg et al., 2001) and orifice type nozzles (Mi et al., 2007; Shinneeb et al, 2008). These investigations have reinforced the existence of local self-similarity in jets. There have been, however, variations reported in the values of the centerline velocity decay and spread coefficients. This may be attributed to errors resulting from different experimental methods and data processing techniques, or these may be due to incorrect scaling resulting from the assumption that jets behave universally, regardless of their initial conditions (George, 1989).

There has been some experimental work comparing the flow fields of jets issuing from different nozzle geometries. Malmström et al. (1997) showed the effect of the diameter of a smooth contraction nozzle on centerline velocity decay in low-velocity axisymmetric jets. The effect of differently shaped nozzles has also been investigated by Mi et al. (2003), showing variation in spreading and mixing rates.

There have also been numerous studies comparing jets issuing from nozzles of the same exit geometry but with different initial condition. Antonia and Zhao (2001) compared the flow fields produced by a smooth contraction and long pipe nozzle at $\mathrm{Re} = 16{,}000$ and found that these two jets reached self-similar behavior at approximately the same downstream distance from the nozzle. In a later paper, Xu and Antonia (2002) showed that the spreading rate of the smooth contraction jet is higher than that of a long pipe at $\mathrm{Re} \cong 86{,}000$. Mi et al. (2001b) compared the scalar fields of jets issuing from these two nozzles and found that the entire flow is influenced by initial conditions, resulting in a variety of self-similar states in the flow. They concluded that the turbulent scalar properties throughout the jet flow field do depend upon initial conditions and that the differences observed in the scalar field of the two jets can be related to differences in the underlying turbulent structure, even in the self-similar region. Mi et al. (2001a) also compared the mixing rates of jets issuing from long pipe, smooth contraction, and orifice nozzles, finding variation in mixing rates between them.

Recent numerical work also addresses the universality of jet self-similarity. Uddin and Pollard (2007) studied the position of the virtual origin in co-flowing jets using large eddy simulation (LES) and showed the ineffectiveness of traditional scaling approaches. Picano and Casciola (2007) used direct numerical simulation (DNS) to show that the accepted scaling methods, which assume universality between jets, conflict with the recovery of small-scale isotropy. These studies do support the influence of initial conditions on downstream flow behavior.

1.4 Summary and Thesis Outline

A review of the literature raises two questions which are relevant to a precessing jet. The first asks whether the self-similar solutions used to model an axisymmetric jet are universal and independent of the initial condition at the source, or whether the initial condition continues to affect the behavior of the jet far downstream from the nozzle. The second examines the effect of the chamber length and Reynolds number on the flow field produced by the precessing jet to determine the optimal chamber geometry to produce the highest occurrence of precession mode.

The following is an outline of this thesis: Chapter 2 describes the experimental method and apparatus used in this study, including an overview of the measurement technique which is used, as well as a thorough description of the flow facility and its relevant components. Chapter 3 examines the effect of initial conditions on the downstream flow field issuing from an axisymmetric jet to determine whether self-similar solutions for this jet are indeed universal or dependant upon source conditions. Chapter 4 contains a parametric study of the effect of chamber length and Reynolds number on the probability of precession mode, as well as parameters including entrainment ratio and the size of the jet. Conditionally averaged mean and RMS velocity fields at the chamber exit plane are also calculated and studied. Conclusions are presented in Chapter 5, as well as a discussion of future work to be performed.

CHAPTER 2: EXPERIMENTAL METHOD AND APPARATUS

2.1 Introduction

The experimental methodology used to examine the flow fields of the axisymmetric and precessing jets is outlined. Stereoscopic particle image velocimetry (StereoPIV) is employed in two configurations to measure the three-components of velocity along a two dimensional region of interest. The StereoPIV method is introduced, and a brief background is provided. The flow facility and all of its components are discussed, as well as the methodology which is used to acquire and process the experimental data.

2.2 Stereoscopic Particle Image Velocimetry

Stereoscopic particle image velocimetry (StereoPIV) is a well developed, non-intrusive flow measurement technique (Adrian, 2005), allowing for resolution of three components of velocity in a two-dimensional region. All StereoPIV configurations require tracer particles, illumination, and a method of imaging the illuminated particles (Raffel et al, 1998). The tracer particles, which are chosen to follow the flow faithfully (Melling, 1997), are illuminated by a light source at two discrete instants in time. The intensity distributions of the illuminated particles are captured in two camera frames. Typically, pulsed lasers are chosen for this application as they deliver high power density in a short period of time, thereby freezing particle motion with each flash. The laser beam is focused into a thin sheet of given width, which also defines the region of interest, as only the particles illuminated by the laser will be recorded by the cameras. A correlation algorithm is used to track the displacement of groups of particles, and this provides a first-order approximation to their velocity, as the time between their positions in the two camera frames is known.

Unlike in other forms of intrusive flow measurement, such as a hot-wire anemometer or a pitot tube which much be situated within the flow, StereoPIV allows for the study an entire flow region, usually bounded by the illumination source of the flow, to be analyzed. Although the point velocities determined with this technique are not true velocities but instead spatially averaged ones, a near continuous velocity map can still be created. This would not be possible with anemometers or pitot tubes since simultaneous and instantaneous point velocity measurements at discrete points within the flow would not only be impractical, they would also disrupt the flow field to the point that any values obtained from measurement would be invalid.

StereoPIV is normally configured so that the highest velocity component occurs along the light sheet plane (Prasad, 2001). In situations where only in-plane velocities are of interest, StereoPIV has been shown to provide a better representation of the flow velocity field than a single-camera PIV configuration would (Prasad, 2001). Studies of the flow fields of axisymmetric jets where the axial velocity of the jet was in-plane include Mi et al. (2008), van Wissen et al. (2005), and Weisgraber and Liepmann (1998).

It is also possible for the highest component of velocity to be out-of-plane, provided that the light-sheet is sufficiently thick and that there is a sufficiently large angle between the two cameras (van Doorne et al, 2003). Matsuda and Sakakibara (2005) used

StereoPIV with the light sheet oriented normal to the flow direction to measure turbulent vortical structures in the self-similar region of an axisymmetric jet. In a similar configuration, van Doorne and Westerveel (2007) measured the three-component velocity field over the exit plane of an axisymmetric jet issuing from a long pipe nozzle as it transitioned from laminar to turbulent flow. Both of these studies used water prisms to minimize the distortion caused by viewing the region of interest from a large angle.

2.3 Flow Facility

The flow facility comprises of a 240L acrylic tank (1.2 m length × 0.5 m height × 0.4 m width), which serves as a quiescent fluid environment into which the jet under study issues. The working fluid, water, is driven by a progressive-cavity, pulseless pump (Model 33204, Moyno) and fluid velocity is set with a variable-speed controller (Model ID15H201-E, Baldor). A schematic of the plumbing of the experimental facility is shown in Figure 2.1. Water exits the tank though a valve in a corner of the tank base, passes through the pump, and encounters a three-way valve which allows for the flow to either pass onto the flow meter (F400, Blue-White Industries), or be drained out of the system. The to-drain connection is also used to fill the system with tap water. After passing through the flow meter, water passes through a plenum, described in the following paragraph, before finally exiting into the tank through one of the nozzle or nozzle-chamber configurations that are studied in this thesis.

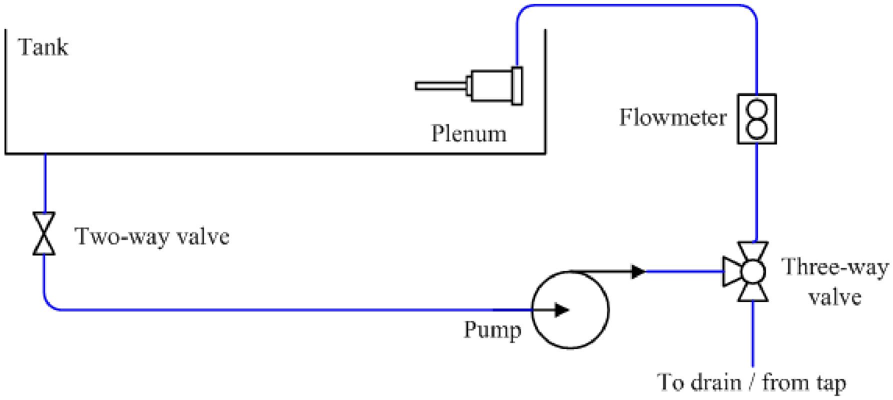

Figure 2.1 System plumbing diagram

The plenum[1], shown in Figure 2.2, is used to minimize any swirl or fluctuation in the incoming flow. Figure 2.3 shows a sectioned view of the plenum and highlights its components. Flow into the plenum enters a settling chamber and passes though four flow conditioning grids. The fluid then passes through a honeycomb grid and a steel mesh before finally passing though a smooth contraction nozzle into a 508 mm (20”) supply pipe of internal diameter 19.05 mm (0.75”). At the end of the supply pipe, the appropriate nozzle is attached with a pressure fit.

---

[1] The plenum was designed by Amanda Kotchon, a second-year undergraduate student at the University of Alberta, as an undergraduate project.

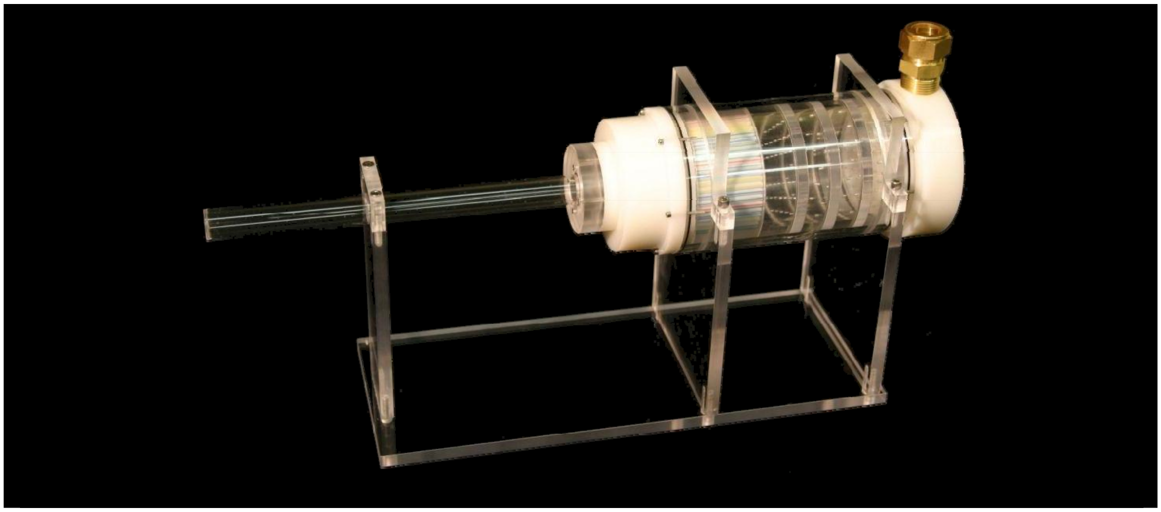

Figure 2.2 A photograph of the flow plenum just after construction.

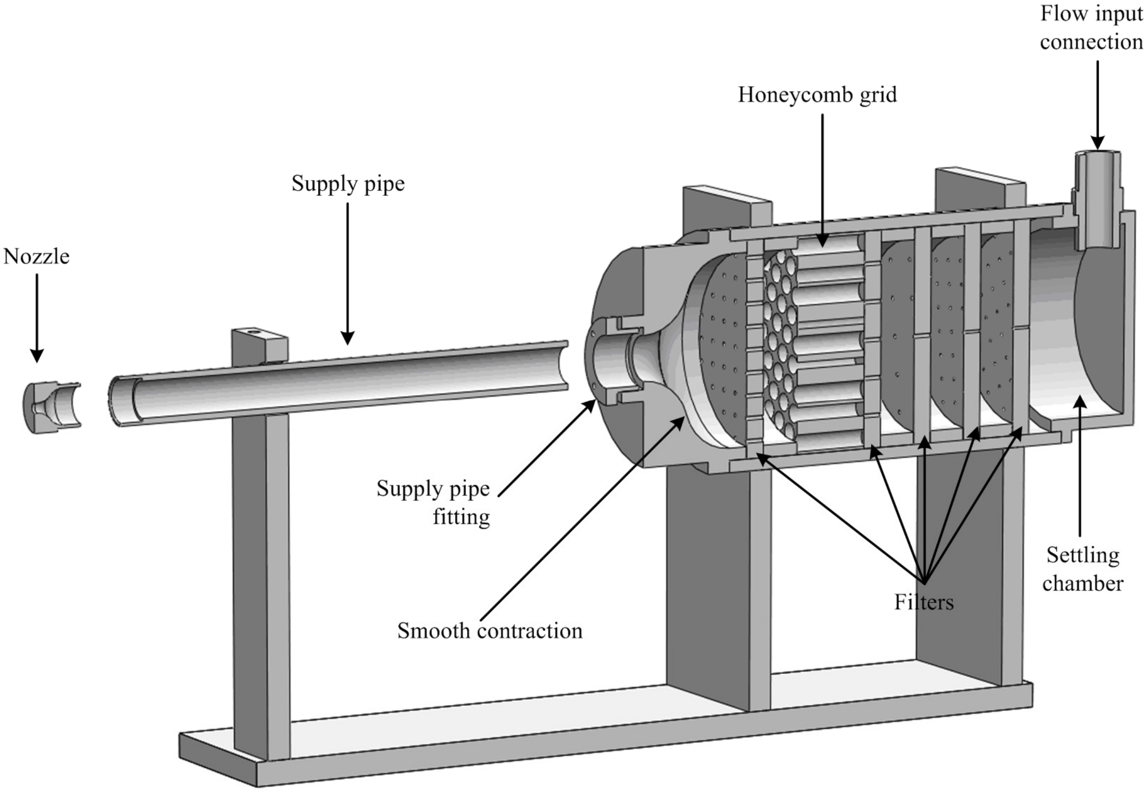

Figure 2.3 Sectioned view of plenum, supply pipe, and nozzle.

It was necessary to calibrate the pump, to relate its rotation speed to the volume flow rate passing through the system. With the volume flow rate known, it was possible to determine the bulk inlet velocity out of the nozzle. The pump was calibrated using an analog flow meter, which was located upstream from the plenum and had an accuracy of ±5% full-scale. Flow rates were observed over the full range of pump rotation speeds, resulting in the pump calibration curve shown in Figure 2.4. Performing a second-order polynomial least-squares fit, the relationship between pump rotation speed, Ω, and volume flow rate through the system, Q, was determined, and is shown in equation (2.1).

$$Q(\Omega) \cong -2\times10^{-6}\Omega^2 + 0.0118\Omega \text{ [L/min]} \tag{2.1}$$

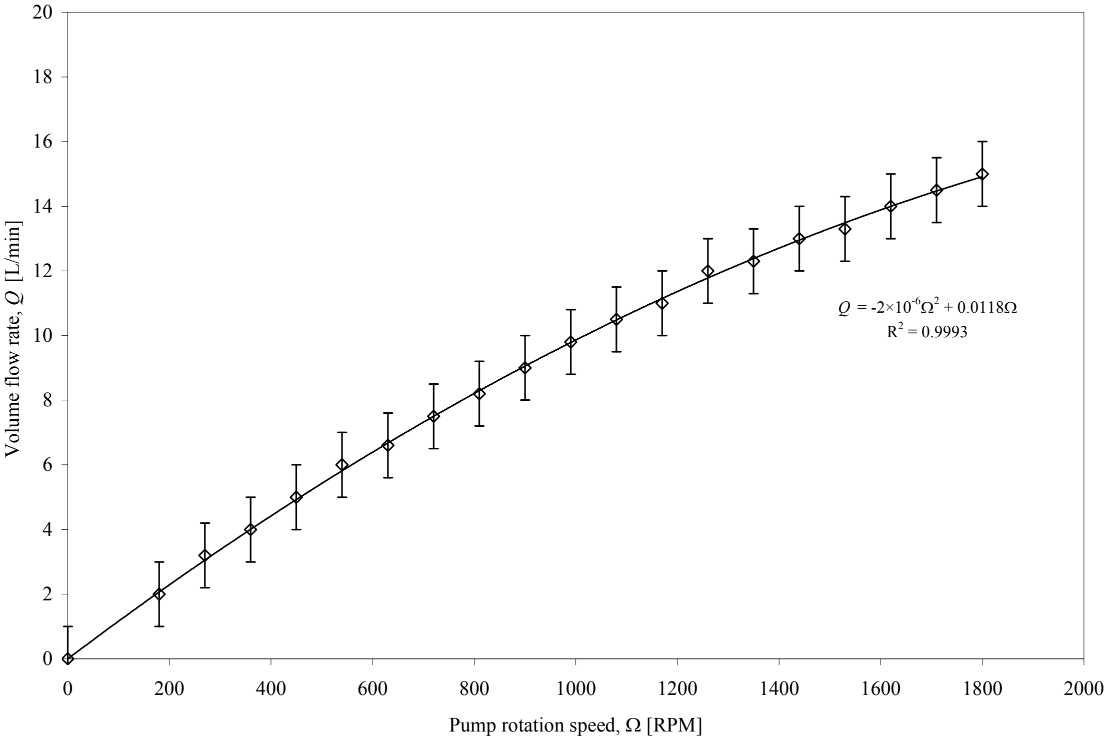

Figure 2.4 Pump calibration curve comparing pump rotation speed to observed flow rate.

Bulk inlet velocity, υ_e, can be calculated using equation (2.2), where A_n is the area of the nozzle exit and d is its diameter. Substituting equation (2.1) into (2.2) results in equation (2.3), which the approximation of bulk inlet velocity based on pump rotation speed. Here, Ω and υ_e carry units of [RPM] and [m/s], respectively.

$$\upsilon_e(\Omega) = \frac{Q}{A_n} = \frac{4}{\pi d^2} Q \tag{2.2}$$

$$\upsilon_e(\Omega) \cong -1.67 \times 10^{-6} \Omega^2 + 0.0098\Omega \tag{2.3}$$

Traditionally, bulk inlet velocity is denoted as U_e, which is the axial component of velocity subscripted with '*e*'. In this study, however, axial velocity carries the variable name *u* or *w*, depending on the orientation of the light sheet: In-plane velocities are always assigned variables *u* and *v*, and the out-of-plane component of velocity is *w*. Therefore, for consistency in the following sections of this thesis, bulk inlet velocity will be denoted as υ_e instead of U_e or W_e, as its value is always determined from equation (2.3).

2.4 Experimental Method

The flow was seeded with 18 μm hollow glass spheres (60P18, Potters Industries), which are assumed to follow the flow faithfully (Melling, 1997). Particle illumination was provided with a high-power, dual-cavity Nd:YAG laser (PIV-400, Spectra Physics), which nominally delivers 400mJ/pulse at an frequency-doubled output wavelength of 532nm and an operating frequency of 10Hz. A more complete specification list for the laser can be found in Table 2-1. The output beam was passed through commercially available light sheet generating optics (FlowMaster 3S, LaVision), which allowed for the adjustment of light sheet width and thickness. The light sheet was reflected off of a turning mirror positioned beneath the tank, and redirected upward through the bottom surface of the tank into the fluid as shown in Figure 2.5.

Table 2-1 Specifications of laser used for particle illumination.

Output Wavelength:	1064 nm, frequency doubled to 532 nm
Pulsed Energy at 532 nm:	400 mJ
Pulse Duration:	10 ns
Repetition Rate:	10 Hz
Beam Diameter:	9 mm
Tunability:	>30 GHz

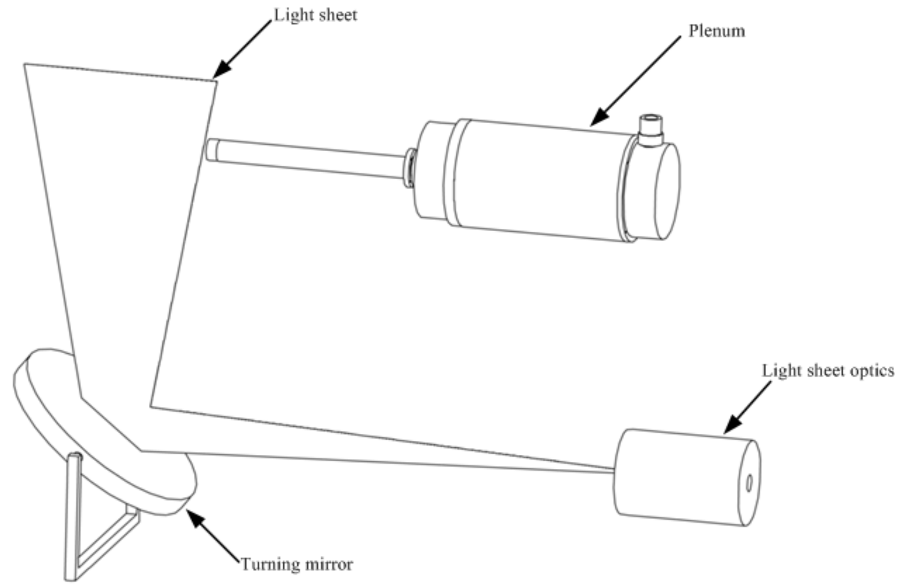

Figure 2.5 Formation of the light sheet, showing the relative positions of the components used.

Images of the illuminated particles were captured with two or four (depending on configuration) high-resolution, 16-bit, dual-frame cameras (LaVision, ImagerX Pro), with a charge coupled device (CCD) array size of 2048×2048 pixels (px). The cameras were mounted on a three-dimensional traverse (Isel), which allowed for translation in three normal directions. The number and location of cameras, as well as any other experiment-specific details are discussed in their respective experimental chapters (Section 3.2.1 for the study of the axisymmetric jet, Section 4.3.1 for the study of the precessing jet).

2.4.1 Calibration

The initial calibration was achieved by imaging a three-dimensional calibration target (LaVision, Type 11) with two cameras. The calibration target is shown in Figure 2.6 as viewed by two cameras in a stereoscopic configuration. It comprises of an array of machined dots in columns (or rows, depending on the orientation of the plate), which alternate in depth, i.e. one column of dots exists in one plane, and the second in another plane, approximately 1mm behind the first. The square and triangle markings in the figure are used as reference points: The dot located in the center of the calibration target is below the square and to the left of the triangle. The target is positioned so that the plane corresponding to the region of interest, which will be referred to as the calibration plane, occurs between the two planes of dots.

Using commercial PIV software (Lavision, DaVis 7.4), the calibration target is imaged with two cameras. Three dots are chosen in an ‘L’ arrangement, which define the origin of the coordinate system of the image and processed vector field. All circles in both planes are found. Comparing the positions of the imaged circles to their known distances on the calibration target, a third-order polynomial mapping function is calculated, allowing for the image obtained by the camera to be dewarped onto the calibration plane.

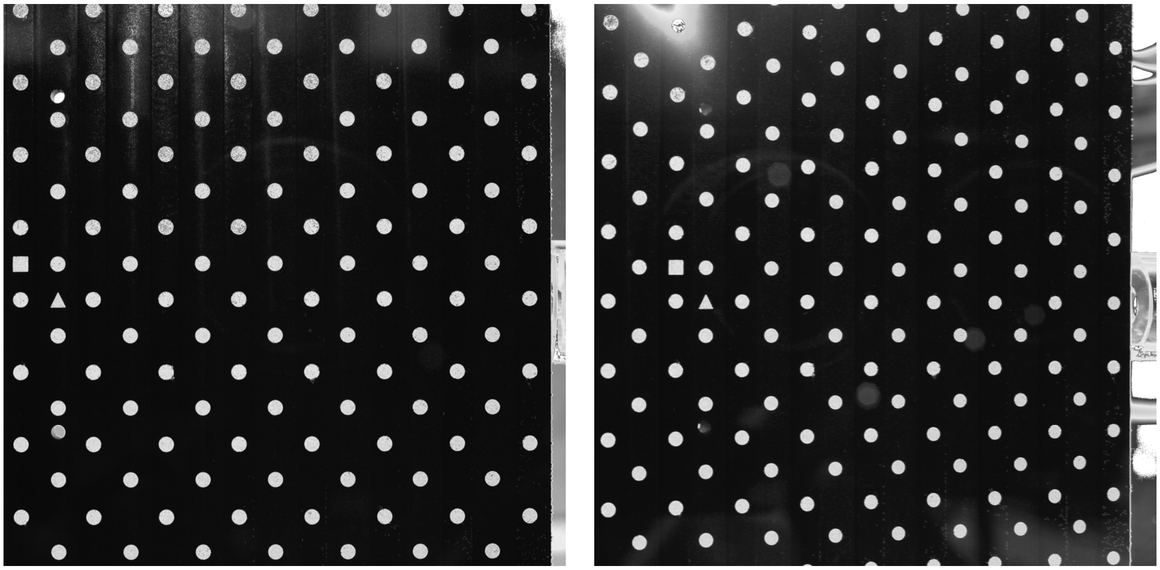

(a) (b)

Figure 2.6 Images of the calibration plate captured by two cameras viewing the same region. The nozzle is visible at the far right of the image.

Calibration is further refined by performing self-calibration (Wieneke, 2005), to ensure that the calibration and measurement planes are in the same position in space, thereby decreasing any errors introduced from the camera images not being properly overlapped. Images of particle distributions from the two cameras are cross-correlated with one another, resulting in a disparity vector map. This map shows the difference in position of the same particle in physical space when mapped from the image planes of two cameras using their respective calibration functions back onto the calibration plane. If the initial calibration is perfect, dewarped particle images from both cameras will overlap perfectly on the calibration plane. This is usually not the case, and the disparity vector map is used to adjust the initial calibration function so that the calibration plane corresponds to the position of the light sheet. An advantage of this calibration method is that the light sheet and calibration plane do not have to be coincident; instead, the self-calibration adjusts for any offset between them.

2.4.2 Image Preprocessing

Before the two frames of each camera image are cross-correlated to produce a vector field, it is necessary to preprocess the images to remove any background image and noise, as well as enhance the shape and intensity of the individual particles. The preprocessing steps used are outlined below. Not all preprocessing steps were used in each study within this thesis. The study-specific image preprocessing algorithms are defined in their appropriate sections. In any equations presented, $\mathbf{I_n}$ and $\mathbf{I'_n}$ are $\Xi \times \Psi$ arrays containing intensity distributions on the camera CCD plane before and after an image preprocessing step, respectively, where **n** denotes the n^{th} of N images. Ξ and Ψ are the width and height of the camera CCD array, in pixels. Subscripts ξ and ψ are the positional coordinates in these arrays, in pixels. The variable a is the parameter of the preprocessing step, and denotes the size of the window/filter used in each step.

2.4.2.1 Background Intensity Subtraction

This preprocessing step compares the intensity values of the same pixel in all N images recorded, and subtracts from each the lowest intensity value. This is useful, for example, when there is a constant intensity at a pixel in all images. When this preprocessing step is applied, the minimum value at a pixel with position (ξ,ψ) over all images, which happens to be the constant value, is subtracted from position (ξ,ψ) in all images. This is illustrated in equation (2.4).

$$\mathbf{I'_n}_{\xi,\psi} = \mathbf{I_n}_{\xi,\psi} - \min\left[\mathbf{I_1}_{\xi,\psi} \quad \mathbf{I_2}_{\xi,\psi} \quad \cdots \quad \mathbf{I_N}_{\xi,\psi}\right] \tag{2.4}$$

2.4.2.2. Subtraction of Sliding Minimum over Time

This preprocessing step helps to eliminate background noise occurring in a successive images. The intensity value of a pixel at position (ξ,ψ) is reduced by the minimum intensity value of that pixel over a images, as shown in equation (2.5). Unlike the Background Intensity Subtraction, which reduces a pixel's intensity value by the minimum over all images, such as a stationary, illumined particle within the flow field, this step eliminates any fluctuating noise or stationary intensity existing in only a few images.

$$\mathbf{I}'_{\mathbf{n}\,\xi,\psi} = \mathbf{I}_{\mathbf{n}\,\xi,\psi} \quad \min\begin{bmatrix} \mathbf{I}_{\mathbf{n}\,\xi,\psi} & \mathbf{I}_{\mathbf{n+1}\,\xi,\psi} & \cdots & \mathbf{I}_{\mathbf{n+a}\,\xi,\psi} \end{bmatrix} \tag{2.5}$$

2.4.2.3 Subtraction of Sliding Minimum

Subtraction of sliding minimum is used to minimize background noise and large, high-intensity areas in the image. The parameter a, in this case, defines the size of the window over which the preprocessing step takes place. At every position (ξ,ψ) in the image, the minimum intensity value within an $a \times a$ region centered about this point is subtracted from the intensity value at (ξ,ψ), as per equation (2.6). The parameter a is set so that it is larger than the size of an imaged particle, otherwise the inner-region of the particle would be removed.

$$\mathbf{I}'_{\xi,\psi} = \mathbf{I}_{\xi,\psi} - \min\begin{bmatrix} \mathbf{I}_{\xi-\frac{a-1}{2},\psi-\frac{a-1}{2}} & \mathbf{I}_{\xi-\left(\frac{a-1}{2}-1\right),\psi-\frac{a-1}{2}} & \cdots & \mathbf{I}_{\xi+\frac{a-1}{2},\psi-\frac{a-1}{2}} \\ \mathbf{I}_{\xi-\frac{a-1}{2},\psi-\left(\frac{a-1}{2}-1\right)} & \mathbf{I}_{\xi-\left(\frac{a-1}{2}-1\right),\psi-\left(\frac{a-1}{2}-1\right)} & \cdots & \mathbf{I}_{\xi+\frac{a-1}{2},\psi-\left(\frac{a-1}{2}-1\right)} \\ \vdots & \vdots & \ddots & \vdots \\ \mathbf{I}_{\xi-\frac{a-1}{2},\psi+\frac{a-1}{2}} & \mathbf{I}_{\xi-\left(\frac{a-1}{2}-1\right),\psi+\frac{a-1}{2}} & \cdots & \mathbf{I}_{\xi+\frac{a-1}{2},\psi+\frac{a-1}{2}} \end{bmatrix} \tag{2.6}$$

2.4.2.4 Min-Max Filter for Intensity Normalization

This is a non-linear filter used to normalize the intensities of particles. Due to shadows, reflections, variation in the light sheet power along its width and depth, and differences in particle sizes, particle intensity may vary throughout the image. This preprocessing step normalizes the intensities in region of size $a \times a$, reducing background intensity and equalizing the intensity peaks.

2.4.2.5 Linear Smoothing Filter

A linear smoothing filter is applied to smooth out the shapes of particles. This is of particular use for images with either non-circular particles, or for particles which are two pixels or smaller in diameter. Every pixel in the image is assigned the average intensity from an $a \times a$ region centered about that pixel, as illustrated in equation (2.7).

$$\mathbf{I}'_{\xi,\psi} = \frac{1}{a^2} \sum_{\tilde{\xi}=\xi-\frac{a-1}{2}}^{\xi+\frac{a-1}{2}} \sum_{\tilde{\psi}=\psi-\frac{a-1}{2}}^{\psi+\frac{a-1}{2}} \mathbf{I}_{\tilde{\xi},\tilde{\psi}} \tag{2.7}$$

The effectiveness of these preprocessing steps is shown in Figure 2.7. A region from an experimental image is magnified and shown as imaged by the camera before and after the five aforementioned preprocessing steps are sequentially applied to it. Note that in some instances, as in the figure, subtraction of sliding minimum of time series does not further improve the image after background count subtraction has already been applied.

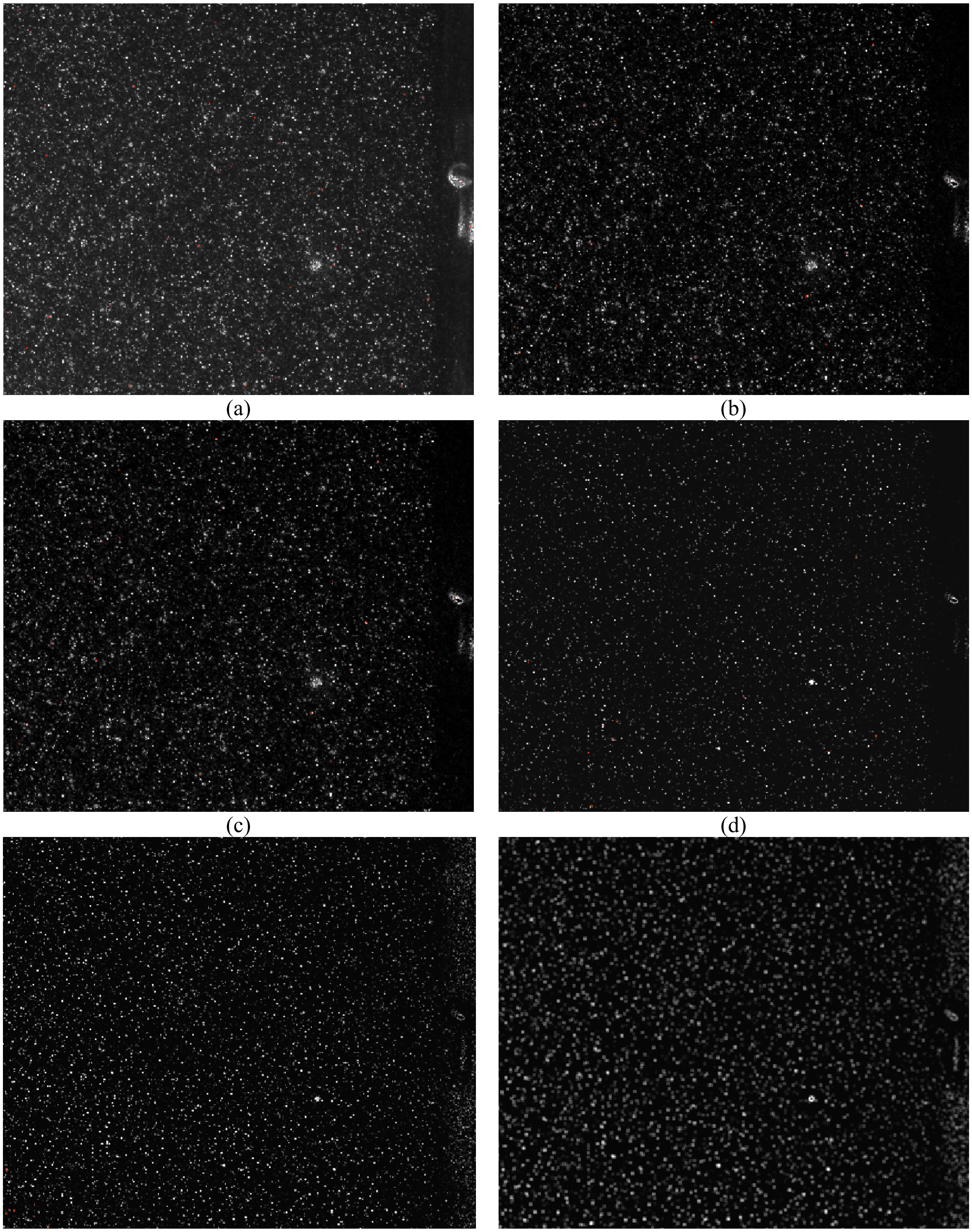

(a) (b) (c) (d) (e) (f)

Figure 2.7 Magnified region of camera image showing particles and edge of nozzle (at right) before and after each preprocessing step: (a) raw image from camera; (b) background count subtraction; (c) sliding minimum subtraction of time series, *a* = 3; (d) sliding minimum subtraction, *a* = 5; (e) min-max filter for intensity normalization, *a* = 10; (f) linear smoothing filter, *a* = 3.

2.4.3 Vector Field Correlation

The particle intensity distributions recorded in each frame by each camera are subdivided into interrogation windows. Corresponding interrogation windows from the two frames of one camera are cross-correlated with each other, resulting in a correlation peak which corresponds to a displacement vector, $\vec{s}$, for the group of particles within that interrogation window. As the particle positions in the first frame occurred at some time t_0, and their positions in the second frame at a later time, $t_0 + \Delta t$, where Δt is a preset and known quantity, the spatially-averaged particle velocity within an interrogation window can be approximated to first-order by equation (2.8) (Raffel et al., 1998).

$$\vec{u} = \frac{\vec{s}}{\Delta t} \tag{2.8}$$

Figure 2.8 outlines the correlation method used. Any out-of-plane velocity observed by a single camera is projected onto an equivalent in-plane velocity component. Using two cameras in a stereoscopic configuration, which form angle α with the normal to the light sheet plane, each camera sees a different projection of the same velocity, allowing for the resolution the out-of-plane component of velocity (Prasad, 2000).

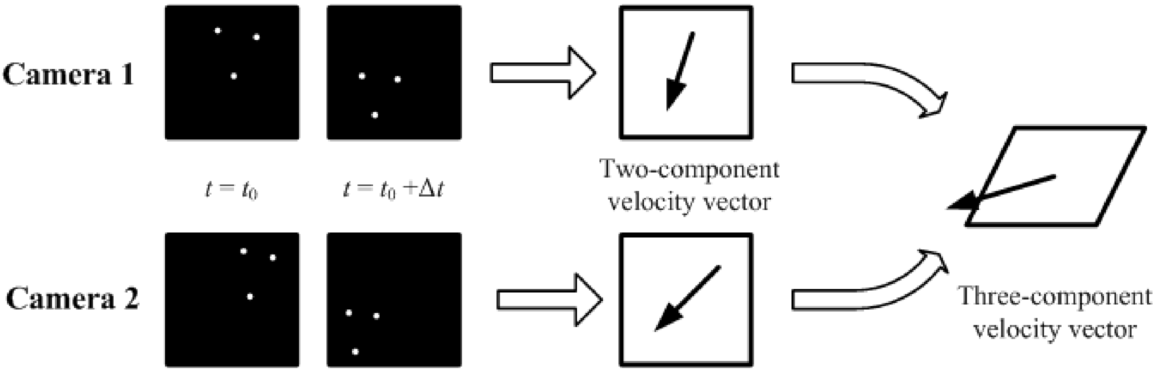

Figure 2.8 Correlation of particle displacements leading to a three-component velocity vector

2.4.4 Vector Field Post-Processing

After correlation, each vector field is treated with a non-linear median filter, which replaces the value of a vector with the median value from surrounding vectors. For every vector at position (i, j) within the array containing velocity data, the velocity values from a 3×3 area centered about (i, j) are sorted by magnitude, and the value at (i, j) is replaced with the median value of the sorted list. This is especially useful in removing spurious vectors. Three component vector fields are finally smoothed with a 3×3 linear filter.

Upon export from the PIV acquisition and processing software (where each vector field exists as a five column table with each row containing two entries representing position, and three entries representing the three velocity components), data is imported into commercial mathematics software (Matlab, Mathworks), where it is sorted into five arrays of dimensions I and J. $\mathbf{X}_{I\times J}$ and $\mathbf{Y}_{I\times J}$ contain spatial coordinates x and y, and $\mathbf{u}_{I\times J}$, $\mathbf{v}_{I\times J}$, and $\mathbf{w}_{I\times J}$ contain the three velocity components of $\vec{u}$ over the studied plane. So, a point in the dataset with array coordinates (i, j) has real world position and velocity vectors given by equations (2.9) and (2.10), respectively.

$$\vec{x}_{i,j} = \begin{bmatrix} \mathbf{X}_{i,j} \\ \mathbf{Y}_{i,j} \end{bmatrix} \tag{2.9}$$

$$\vec{u}_{i,j}\left(\vec{x}_{i,j}\right) = \begin{bmatrix} \mathbf{u}_{i,j} \\ \mathbf{v}_{i,j} \\ \mathbf{w}_{i,j} \end{bmatrix} \tag{2.10}$$

Average and RMS velocity data are stored in the same manner. The three arrays containing average velocity components are denoted **U**, **V**, and **W**, while RMS velocity components have array names **u′**, **v′**, and **w′**.

2.5 Summary

StereoPIV is employed in two configurations to measure the three-component velocity fields in a two-dimensional region of interest. A background to the experimental technique has been provided. The experimental methodology has been explained, and a description of the flow facility and all of its components was given.

CHAPTER 3: THE EFFECT OF INITIAL CONDITION ON THE ASYMPTOTIC BEHAVIOR OF AN AXISYMMETRIC JET

3.1 Introduction

The effect of initial conditions on far-field parameters was investigated by studying the flow field of a jet issuing from one of three inlets: a long pipe, a smooth contraction, and an orifice type nozzle. Each of these has the same exit diameter, *d*, and therefore produces the same mass flux and nearly the same momentum flux at a given Reynolds number. These three inlets differ only in the velocity profiles generated at their exits. Traditional scaling theory (Townsend, 1976) dictates that sufficiently far downstream from the nozzle in the self-preserving region of the jet, initial condition is 'forgotten', and characteristic parameters of the flow asymptote to universally constant values. This is investigated using three different nozzles, each generating a different initial flow condition, and studying the effects on asymptotic behavior far downstream over a range of Reynolds numbers. The flow fields resulting from these nozzles are studied at Reynolds numbers of 5,800, 10,000, 21,800, 32,400, 50,700, and 61,900. RMS axial velocity profiles, centerline velocity decay and jet half-spread coefficients, and virtual origin positions are compared for the three inlet conditions to determine whether there is universality between these jets, or whether the effect of initial conditions do indeed remain present.

3.2 Experimental Method

Three nozzles were used with identical outlet diameters, *d* = 5 mm, resulting in identical initial mass fluxes: Smooth contraction, orifice, and long pipe. Rendered cutaway drawings of these three inlets are shown in Figure 3.1, while their schematic drawings are shown in Appendix C. The smooth contraction has an area ratio of 1:14 and is formed with two circular arcs of equal radius, tangent at their meeting point. The orifice nozzle has a 45° reverse camber to the flow. The long pipe nozzle commences with a smooth contraction, formed in the same manner as the nozzle shown in Figure 3.1(a), and leads into a development length of $L_d = 10D_s$, where $D_s = 19.08$ mm (0.75”) and is the inner diameter of the supply pipe to which the three nozzles are attached.

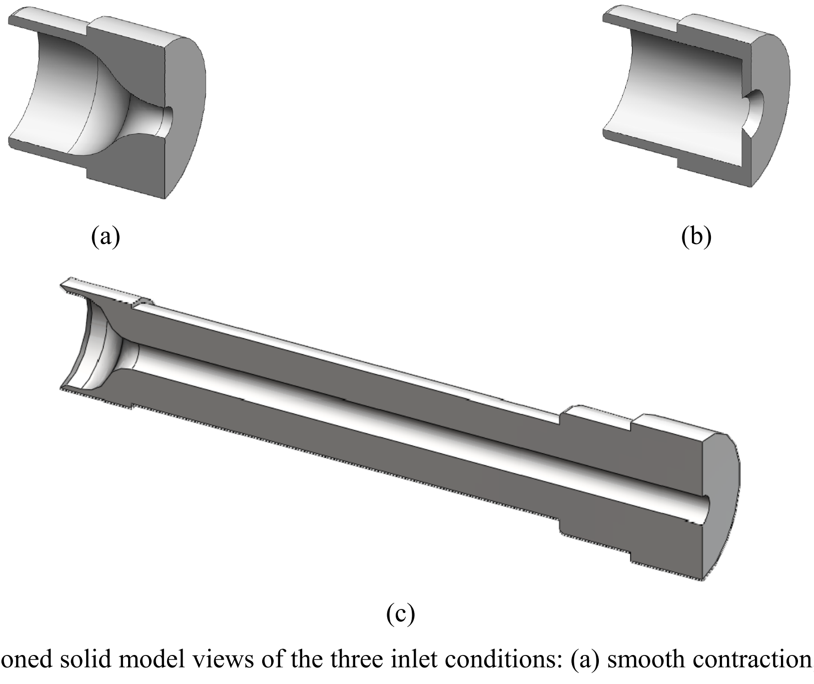

(a) (b)

(c)

Figure 3.1 Sectioned solid model views of the three inlet conditions: (a) smooth contraction, (b) orifice, (c) long pipe.

3.2.1 StereoPIV Setup

StereoPIV was employed to study the velocity field of the jet with the three inlet conditions. Two pairs of cameras were used, to allow for the observation of a region of interest reaching up to 40*d* downstream from the nozzle exit. The experimental configuration showing the relative positions of the cameras to the flow facility and light sheet is shown in. The four cameras were positioned at the height of the jet axis, suspended on a three-axis traverse (Isel). Each camera formed a ±20° angle with a vector normal to the light sheet, at an approximate distance of 500 mm. The light sheet was positioned so that it passed through the nozzle axis, with an approximate width and thickness of 250 mm and 0.5 mm, respectively. One side of the light sheet touched the nozzle exit plane.

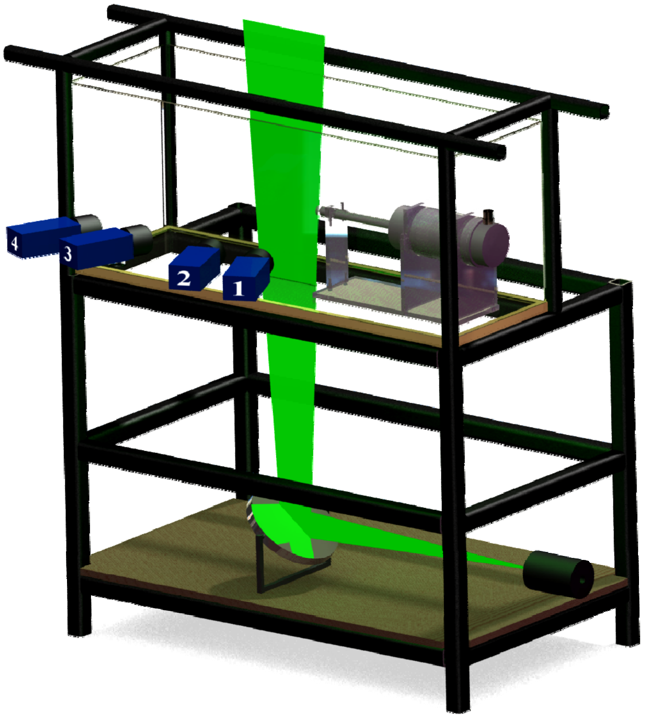

Figure 3.2 Solid model showing the relative positions of the four cameras, light sheet, plenum, and tank.

One thousand dual-frame images were collected per nozzle at Reynolds numbers of 5,800, 10,000, 21,800, 32,400, 50,700, and 61,900 with each camera. The Reynolds number was based on the nozzle exit diameter, *d*, and bulk inlet velocity, υ_e, i.e. $\mathrm{Re} = \nu \upsilon_e d$. Cameras '1' and '2' viewed the near field, while cameras '3' and '4' viewed the far-field. The numbering of cameras is shown in Figure 3.2. The fields of view from the two pairs of cameras were overlapped, as shown in Figure 3.3, to ensure that there is continuity between the vector fields obtained from both camera pairs.

Due to the deceleration of the jet with increased downstream distance from the nozzle, it would have been unreasonable to attempt to achieve the desired particle displacements required for robust processing in both near- and far-field regions simultaneously using a single value of Δt . Images for the near-field and far-field were collected separately using different time steps, and then merged after processing and averaging. Table 3-1 contains the time step values used for each Reynolds number studied for both camera pairs.

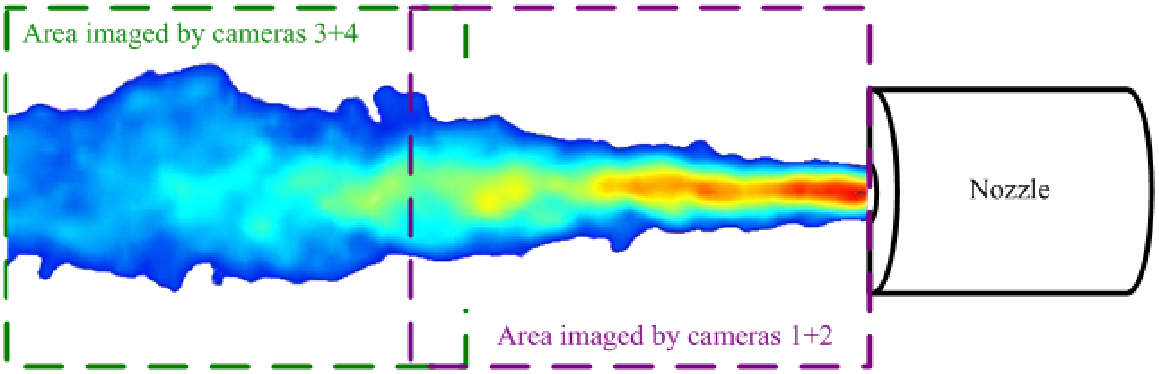

Figure 3.3 The overlapped fields of view from the two camera pairs.

Table 3-1 Time steps used with different flow rates for all axisymmetric nozzles.

Pump Speed, Ω [RPM]		120	210	480	750	1320	1800
Reynolds number, Re		5,800	10,000	21,800	32,400	50,700	61,900
Time step,	*Cameras 1+2*	120	80	35	28	25	20
Δt [µs]	*Cameras 3+4*	400	280	110	85	65	50

3.2.2 StereoPIV Processing

Image data from both pairs of cameras were processed using the algorithm shown in Figure 3.4. The images from the raw cameras were first treated with background count subtraction and sliding background subtraction of time series over three images, to minimize the appearance of the nozzle, as well as any regions with background intensity which remains constant. Sliding minimum subtraction with a 5 px window was then applied to eliminate any background intensity in the images. Finally, a min-max filter (10 px) and 3×3 linear smoothing were used to normalize particle intensities in the image and smooth out their shape. A more detailed description of the image preprocessing steps used is provided in Section 2.4.2.

Correlation was performed with a multi-pass approach with a decreasing interrogation window size. Initially, a 64×64 px interrogation window with 75% overlap was used, to determine an initial, coarse vector field. Correlation was then repeated twice using a 32×32 px interrogation window and 75% overlap, with the vector field from the previous step acting as an initial particle search field for the next. The final vector fields were treated with a median filter, to remove any spurious vectors, and smoothed with a 3×3 linear filter. Average and RMS vector fields for each Reynolds number and inlet condition were finally calculated.

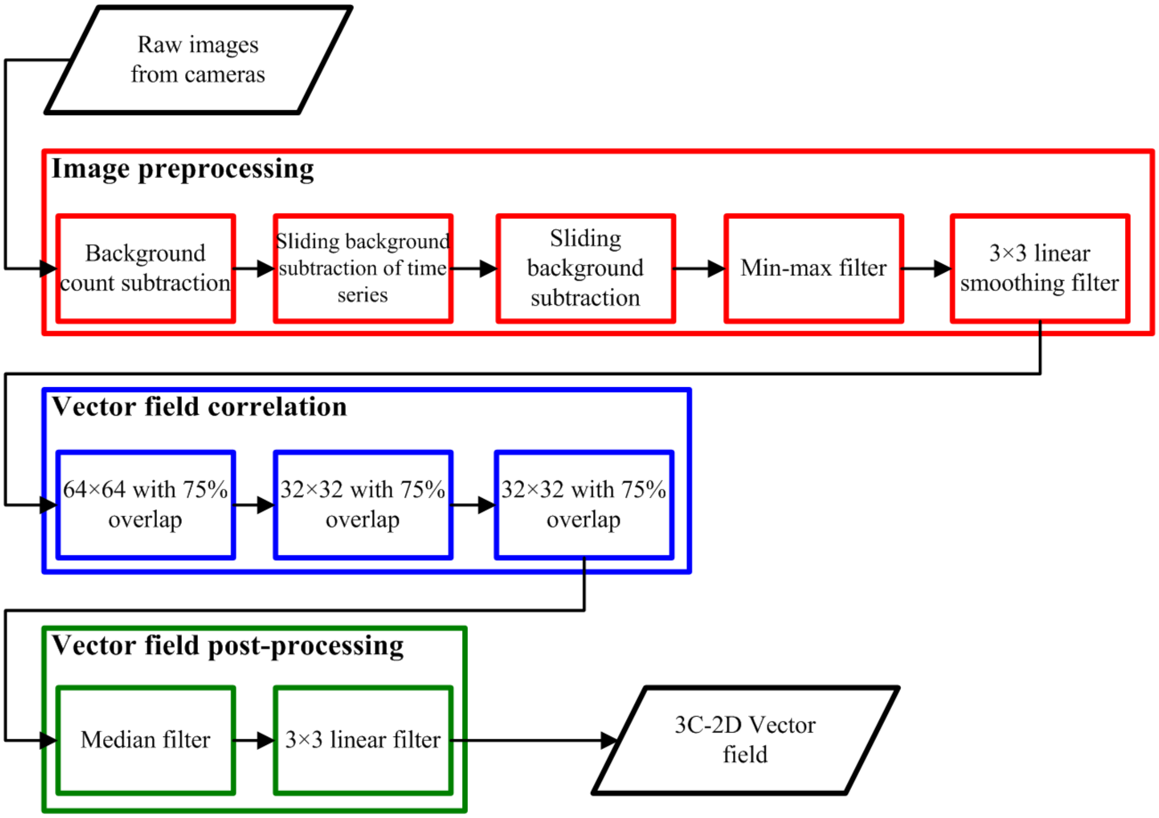

Figure 3.4 StereoPIV processing algorithm for axisymmetric jet data.

3.2.3 Merging of Vector Fields

Upon exporting from the PIV acquisition software, averaged and RMS vector fields for each inlet condition and Reynolds number existed in two parts, one in the near-field and the other in the far-field. In this section, subscripts ‘1’ and ‘2’ on variables will represent these two regions, respectively. It was therefore necessary to join these to obtain a vector field for the ROI. The vector fields were first manually cropped, to remove any spurious data which may exist on the boundary. All data from each inlet condition, including average and RMS vector fields, were cropped with the same range. The far-field data were interpolated so that their grid spacing matched that of the near-field data.

The centerline velocities of the near-field and far-field vector fields were first determined using the method outlined in Section 0, and shown in Figure 3.5. The *x*-axis shows the i-coordinate within the arrays, which corresponds to the axial distance from the nozzle, in grid points, and the centerline velocity, U_{cl}, is scaled against bulk inlet velocity. The necessary shift in this direction is the distance between two identical U_{cl} values. The furthest downstream data point of the near-field set was chosen as a reference value, and the closest in value centerline position in the far field was found, with streamwise grid coordinate i_0. These points in both arrays occupied the same point in physical space.

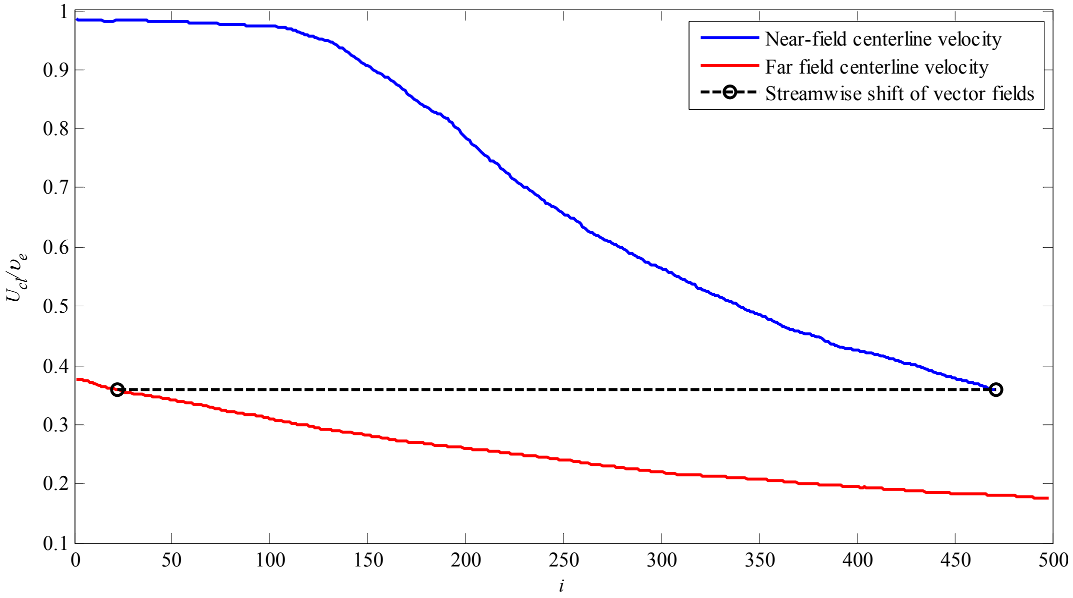

Figure 3.5 Centerline velocities obtained from both camera pairs, as well as the axial distance separating corresponding data points.

Once the offset in the axial direction was known, it was possible to determine the necessary shift in the spanwise direction. This was achieved by comparing two spanwise velocity profiles from the near-field and far-field average axial velocity arrays of size $I_1 \times J_1$ and $I_2 \times J_2$, respectively. The first velocity profile was created at the furthest downstream axial position $i_1 = I_1$ in the near-field array, and the second was created at grid position $i_2 = i_0$ in the far-field array. These two velocity profiles should be the same, as they are at the same axial distance in physical space, but offset in the spanwise direction. The necessary shift, j_0, was the difference in the *j*-indices between the positions of the velocity maxima of both profiles. This is illustrated in Figure 3.6. The blue and the red lines represent velocity profiles in the near field at $i_1 = I_1$ and in the far field at $i_2 = i_0$, respectively, while the length of broken line represents the value of j_0. The *x*-axis shows the *j*-coordinate in the arrays, while the *y*-axis shows the nondimensionalized centerline velocity scaled against bulk inlet velocity.

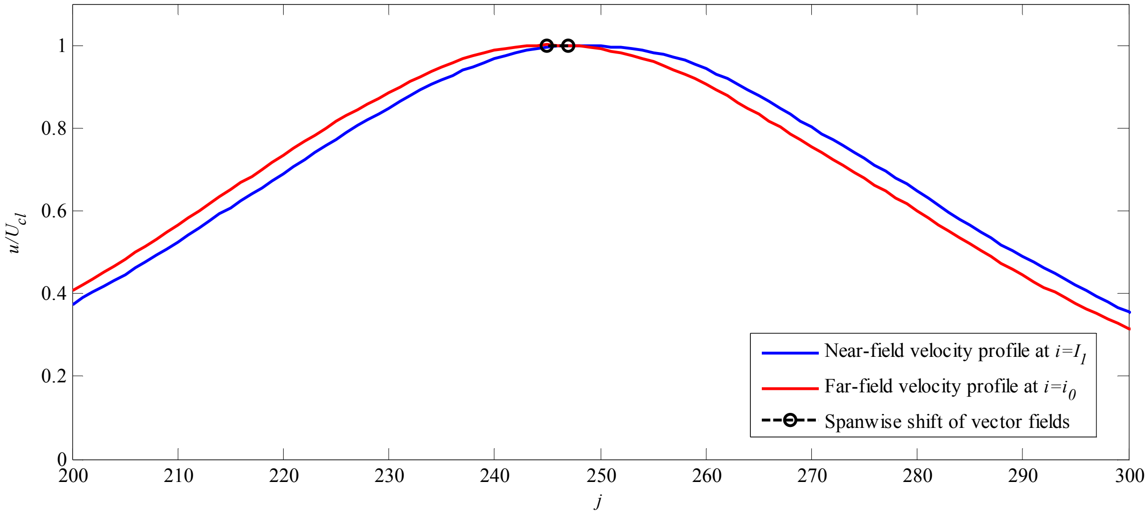

Figure 3.6 Spanwise velocity profiles of the same axial distance from the nozzle obtained with both sets of cameras.

New arrays were created of size $I \times J$, which are defined in equations (3.1) and (3.2). The length of the new arrays is that of the near-field array and the distance between the common centerline velocity value and the endpoint of the far-field array, while the width is equal to that of the near-field array.

$$I = I_1 + (I_2 - i_0) \tag{3.1}$$

$$J = J_1 \tag{3.2}$$

Positional coordinate arrays **X** and **Y** were constructed using equations (3.3) and (3.4). These were simply filled by incrementally increasing the position value by the known grid spacing as either axial or spanwise distance from the respective edge ($i = 1$ or $j = 1$) increased, beginning with the value at that edge.

$$\mathbf{X}_{i,j} = \mathbf{X}_{\mathbf{1}1,1} + (i-1)\delta x_1 \tag{3.3}$$

$$\mathbf{Y}_{i,j} = \mathbf{Y}_{\mathbf{1}1,1} + (j-1)\delta y_1 \tag{3.4}$$

The near- and far-field arrays were combined using equation (3.5) for all *i* and *j* values between one and *I* and *J*. Any points in the new arrays which were not defined in the existing ones were assigned a null value, and any points which were to be placed outside of the new array were ignored. **V** and **W** velocity component arrays, as well as RMS velocity component arrays, **u′**, **v′**, and **w′** were constructed in the same manner, using the shift values i_0 and j_0 determined from the axial velocity vector fields.

$$\mathbf{U}_{i,j} = \begin{cases} \mathbf{U}_{\mathbf{1}i,j}, & 1 \le i \le I_1, \quad 1 \le j \le J_1 \\ \mathbf{U}_{\mathbf{2}i+i_0,j+j_0}, & i_0 < i \le I_2, \quad j_0 \le j \le J_2 \ , \quad \forall i,j \\ 0, & \text{otherwise} \end{cases} \tag{3.5}$$

Figure 3.7 shows a sample axial velocity field before and after merging. The quality of the merging can be assessed by observing the jet boundary along its length. There is no apparent discontinuity.

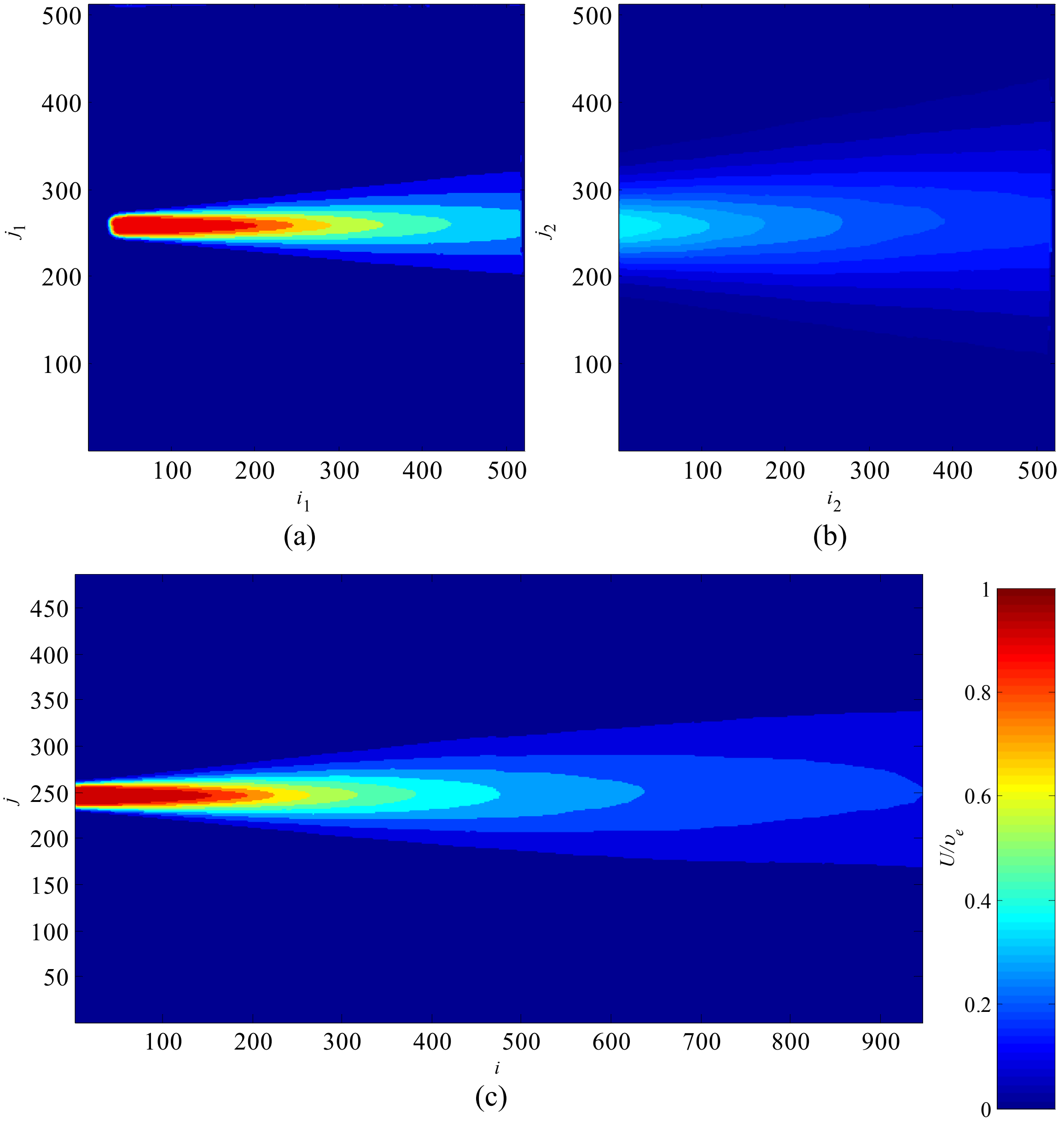

Figure 3.7 Contour plot of axial velocity of (a) near-field (b) and far-field before, and (c) after vector field merging.

3.3 Effect of Initial Conditions on Jet Parameters

3.3.1 Velocity Profiles at the Jet Exit Generated by Different Nozzles

The spanwise velocity profiles of the jet just beyond the nozzle exit at an approximate axial distance of $x/d \approx 2$ are shown in Figure 3.8 for the long pipe (a), orifice (b), and smooth contraction (c) inlet conditions. The average and RMS of axial velocity are shown for all studied Reynolds numbers, and are nondimensionalized against the initial centerline velocity at the nozzle exit, U_0 (see Section 0). No velocity profiles closer to the jet exit were possible, due to the reflections off of the nozzle from the light sheet, which resulted in erroneous vectors in that region.

The average and RMS axial velocity profiles obtained conform to the expected profiles for each of the inlets. In Figure 3.8, the broken lines represent the theoretical velocity profiles at the nozzle exit. The long pipe (a) follows a seventh-order relationship with spanwise distance from the jet centerline, *y*, shown in equation (3.6) (Ru and Antonia, 2002), while the smooth contraction (c) results in a top-hat velocity profile. The orifice nozzle results in a parabolic velocity profile in-between that of the smooth contraction and long pipe, approximated with equation (3.7).

$$\frac{U}{U_0} \cong \left(1 - 2\frac{y}{d}\right)^{\frac{1}{7}} \tag{3.6}$$

$$\frac{U}{U_0} \cong 4\left(\frac{y}{d}\right)^2 - 1 \tag{3.7}$$

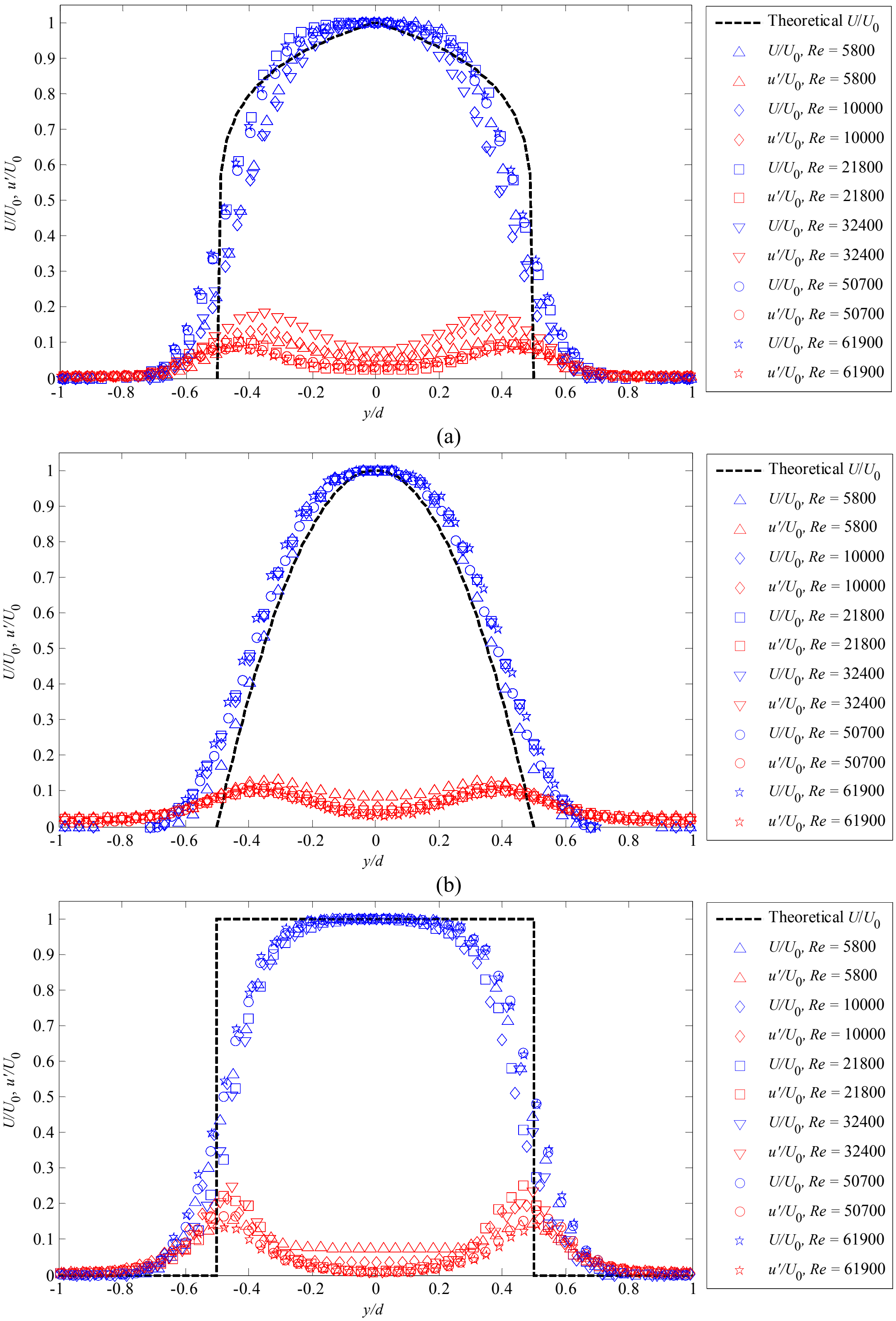

(a)

(b)

(c)

Figure 3.8 Average and RMS velocity profiles at the closest axial position to nozzle exit ($z/D \approx 1$) for (a) long pipe, (b) orifice, and (c) smooth contraction inlet conditions.

The RMS profiles for the three inlet conditions also agree with the expected results. The fluctuation in axial velocity peaks at the edges of the jet, and is a minimum at the centerline. The fluctuation is largest for the smooth contraction jet, due to the thin shear layer at the interface between the issuing jet and the surrounding fluid. The orifice and long pipe nozzles show similar RMS velocity distributions; however, the maxima of these are smaller than that of the smooth contraction. It is apparent from the figure that for the orifice and smooth contraction nozzles, the RMS profiles for all Reynolds numbers except 5,800 collapse onto one another.

3.3.2 Average and RMS Velocity along the Jet Centerline

The average and RMS axial velocities along the jets centerlines were compared for the three initial conditions. The centerline velocity at a downstream distance $x = \mathbf{X}_i$ (at a grid position *i*) is calculated as the maximum axial velocity component value in a spanwise profile. This results in the $1 \times I$ array $\mathbf{U_{cl}}$ containing all centerline velocity values in the ROI, defined in equation (3.8). Figure 3.9 shows average axial velocity profiles, and the location of the jet centerline velocity relative to them (shown as the red line). Spatial coordinates are scaled against the nozzle diameter, while the centerline velocity is scaled against the initial centerline velocity value, U_0, which is calculated as the mean of the first five measured centerline velocity values nearest to the nozzle, and is defined in equation (3.9).

$$U_{cl}(\mathbf{X}_i) = \mathbf{U_{cl}}_i = \max(\mathbf{U}_{i,j}), \quad 1 \le j \le J \tag{3.8}$$

$$U_0 \equiv \frac{1}{5} \sum_{i=1}^{5} \mathbf{U_{cl}}_i \tag{3.9}$$

The centerline RMS axial velocity profile, $\mathbf{u}'_{\mathbf{cl}}$, is constructed from the array $\mathbf{u}'$, which contains axial RMS velocity data from the entire region of interest. For every axial distance $x = \mathbf{X}_i$, corresponding to the i^{th} grid point in the data arrays, the RMS axial velocity component value is found which exists at the same spanwise grid position, *j*, as the centerline velocity value does in the average velocity array. This is illustrated in equation (3.10).

$$u'_{cl}(\mathbf{X}_i) = \mathbf{u}'_{\mathbf{cl}i} = \mathbf{u}'_{i,j} \ni \mathbf{U}_{\mathbf{cl}i} = \mathbf{U}_{i,j} \tag{3.10}$$

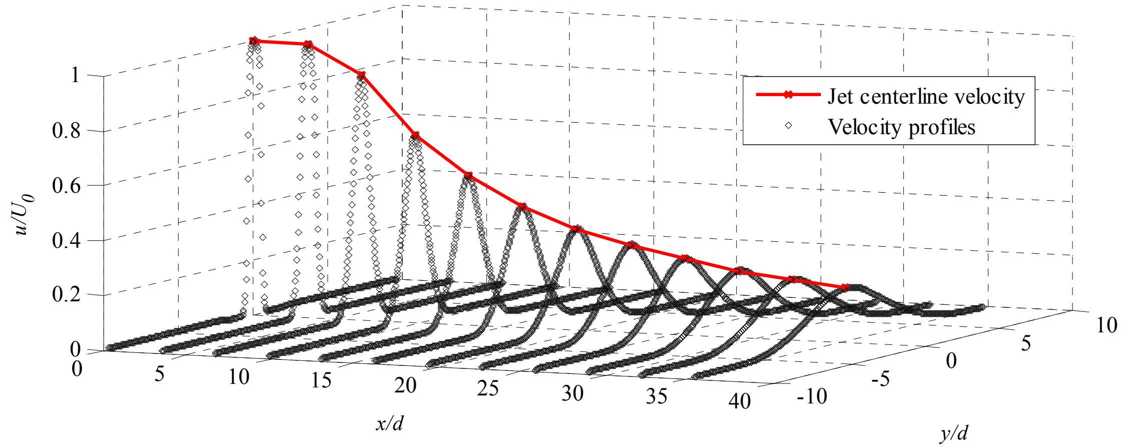

Figure 3.9 Axial velocity profiles in the spanwise direction and the location of the jet centerline.

3.3.3 The Effect of Initial Condition on Centerline Velocity Decay

Nondimensionalized centerline velocity profiles are presented in Figure 3.10 for the long pipe (a), orifice (b), and smooth contraction (c) nozzles, for all Reynolds numbers studied. Since the centerline velocity is inversely proportional to axial distance from the nozzle in the self-preserving region beyond the potential core and transition zone, i.e. $U_{cl} \sim 1/x$ (Rajaratnam, 1976), centerline velocity is nondimensionalized against initial centerline velocity, U_0.

Three characteristic regions of the jet are apparent in Figure 3.10. The development region occurs closest to the nozzle, and is characterized by a constant centerline velocity, i.e. $U_0/U_{cl} = 1$. Beyond this is the transition zone, where the slope of the dimensionless centerline velocity increases as the jet begins entraining fluid (Wygnanski & Fiedler, 1969). In the self-similar region, U_0/U_{cl} is linear, following the relationship in equation (3.11). Here, χ is the nondimensional axial distance from the virtual origin of the jet and is defined in equation (3.12), and K_1 describes the rate at which velocity along the centerline decreases.

$$\frac{U_0}{U_{cl}} = \frac{1}{K_1}\chi \tag{3.11}$$

$$\chi \equiv \frac{x - x_{o,1}}{d} \tag{3.12}$$

The self-similar behavior is apparent for all three inlet conditions, as the centerline velocity decay profiles collapse well onto one another when nondimensionalized. For the long pipe nozzle, dimensionless centerline velocity values at Reynolds numbers above 10,000 collapse onto a single curve, while for the smooth contraction, this is true above $\mathrm{Re} = 5{,}800$.

In the derivation of the self-similar equations, it is assumed that turbulent shear stresses dominate over viscous stresses (Rajaratnam, 1976), allowing for the neglect of all viscous terms. However, in a laminar or transitioning flow regime, this assumption does not hold the same validity. Dimensionless centerline velocity decay profiles for the long pipe at Reynolds number of 5,800 and 10,000, and for the smooth contraction at $\mathrm{Re} = 5{,}800$ do not collapse onto the same curves as do the higher Reynolds numbers. It can therefore be deduced that for these lower Reynolds numbers for these two inlet conditions, flow is not fully turbulent.

The nondimensional velocity profiles for all nozzles at all Reynolds numbers are shown in Figure 3.11, where Reynolds numbers are grouped by symbol and inlet condition is grouped by color (red - long pipe, green - orifice, blue - smooth contraction). Centerline velocity is scaled with U_0, and axial distance is shown as χ, so that the extrapolated best-fit lines in the self-similar region of all profiles pass through a common virtual origin. It is immediately apparent that the velocity profiles for all three inlet conditions do not collapse onto a single line as would be expected when considered from the point of view of traditional self-similarity theory. Excluding low Reynolds number cases where the flow may not be fully turbulent and therefore behave differently, the centerline velocity decay at a given Reynolds number should be the same, regardless of its initial condition. Instead, Figure 3.11 shows that the jet issuing from the orifice nozzle decays the fastest, and the smooth contraction the slowest.

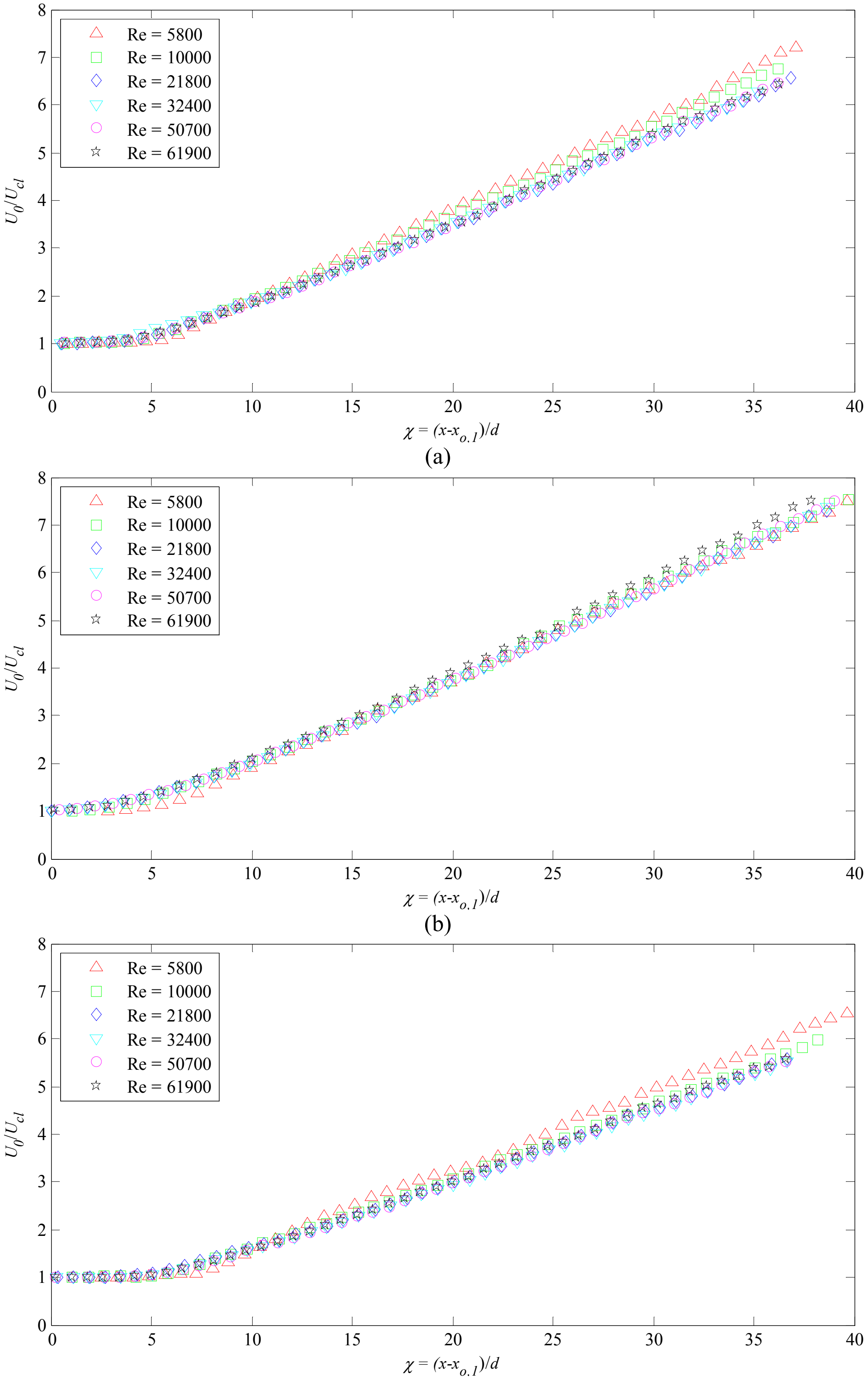

(a)

(b)

(c)

Figure 3.10 Nondimensionalized centerline velocity for long pipe (a), orifice (b), and smooth contraction (c) inlet conditions. Every 20th data point is plotted for clarity.

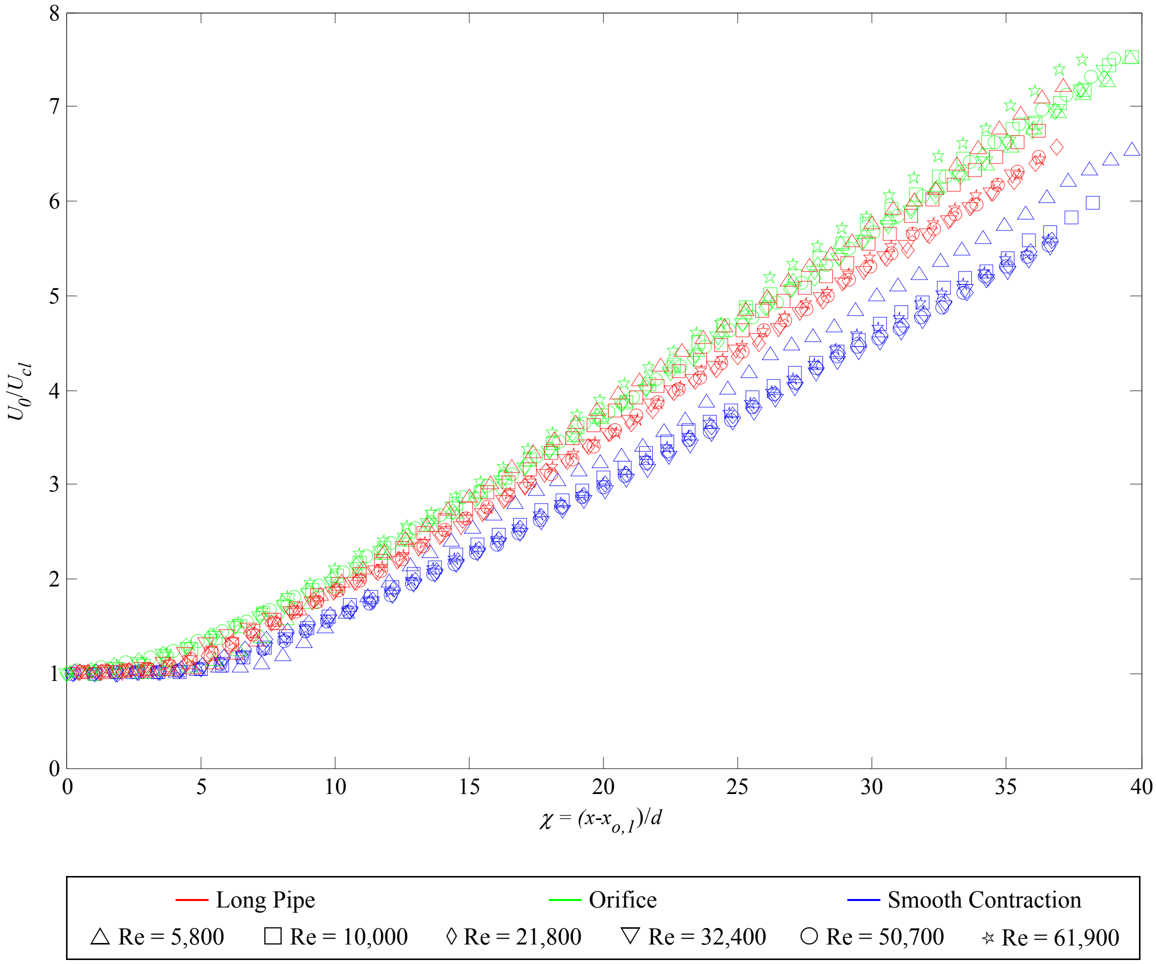

Figure 3.11 Collapsed nondimensionalized centerline velocity profiles for the three inlet conditions. Every 20th data point is plotted.

The centerline velocity decay rate and position of virtual origin were compared for all initial conditions and Reynolds numbers. In the self-similar region of the jet, the scaled velocity, U_0/U_{cl}, increases linearly with axial distance following equation (3.11), as apparent in Figure 3.12. Performing a linear least-squares fit of the data within this region ($x_1/d \le x/d \le x_2/d$) results in the centerline velocity decay coefficient, K_1, which characterizes the rate at which the axial velocity of the jet along its centerline. The lower bound of the regression range, x_1, was chosen as the first axial position downstream of the nozzle at which $U_0/U_{cl} \geq 1.25$. The higher bound, x_2, occurs at 90% of the length of the ROI in the axial direction, which can be expressed in terms of discretized grid location as $x_2 = \mathbf{X}_{i=\|0.9I\|}$, where i and I are the grid position and array size in the axial direction, respectively. The intercept of this best-fit line with the *x*-axis defines the virtual origin, $x_{o,1}$ of the jet (Pope, 2000), which represents the origin of momentum if the jet were modeled as a point source thereof. The individual centerline velocity decay profiles showing the lines of best fit used for determining K_1 and the positions of the virtual origin for all nozzles at all Reynolds numbers are shown in Appendix D.

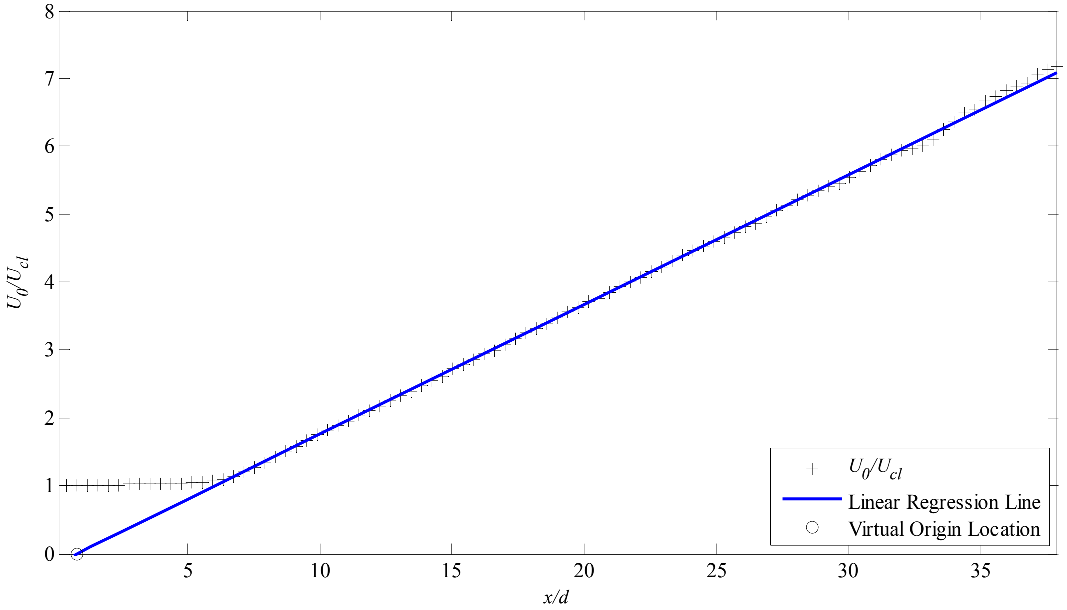

Figure 3.12 Nondimensionalized centerline velocity for smooth contraction at Re = 32,400, showing the best-fit line in the self-similar region and the location of the virtual origin.

The relationship between centerline velocity decay coefficient, K_1, and Reynolds number for the three nozzles studied is shown in Figure 3.13. There is an obvious relationship between nozzle configuration and decay coefficient, as the three K_1 vs. Re profiles differ in value. The smooth contraction nozzle shows the highest K_1, and the orifice the lowest. If the tradition self-similar solutions for the jet were indeed universal, these profiles should be identical.

The Reynolds number at which each jet reaches local self-similarity can also be deduced from Figure 3.13. When the jets reach a self-similar state, K_1 should reach an asymptotic value. It is apparent from the figure that above $\mathrm{Re} = 21{,}800$, the K_1-profiles appear to level off. There is some dependence of K_1 on Reynolds number. Below $\mathrm{Re} = 32{,}400$, K_1 increases for all nozzles. Mi et al. (2001b) have also observed K_1 dependence on Reynolds number for the smooth contraction nozzle, and almost no dependence for the long pipe. Above this Reynolds number, for the smooth contraction and long pipe nozzles, K_1 gradually decreases. For the orifice nozzle, K_1 remains almost constant, then finally decreases at $\mathrm{Re} = 61{,}900$.

The relationship between the virtual origin, determined from the nondimensionalized centerline velocity decay, $x_{o,1}$, and Reynolds number is shown in Figure 3.14 for the three nozzles. Apart from a suspicious value for the long pipe at $\mathrm{Re} = 21{,}800$, which is discussed in Section 0, the locations of the virtual origin show an increasing trend with Reynolds number, with values being largest for the long pipe and smallest for the orifice nozzle. The smooth contraction and orifice nozzles appear to reach their asymptotic values beyond $\mathrm{Re} = 21{,}800$, although $x_{o,1}$ continues to increase over the range of Reynolds numbers studied. The long pipe appears to reach its asymptotic value beyond $\mathrm{Re} = 32{,}400$.

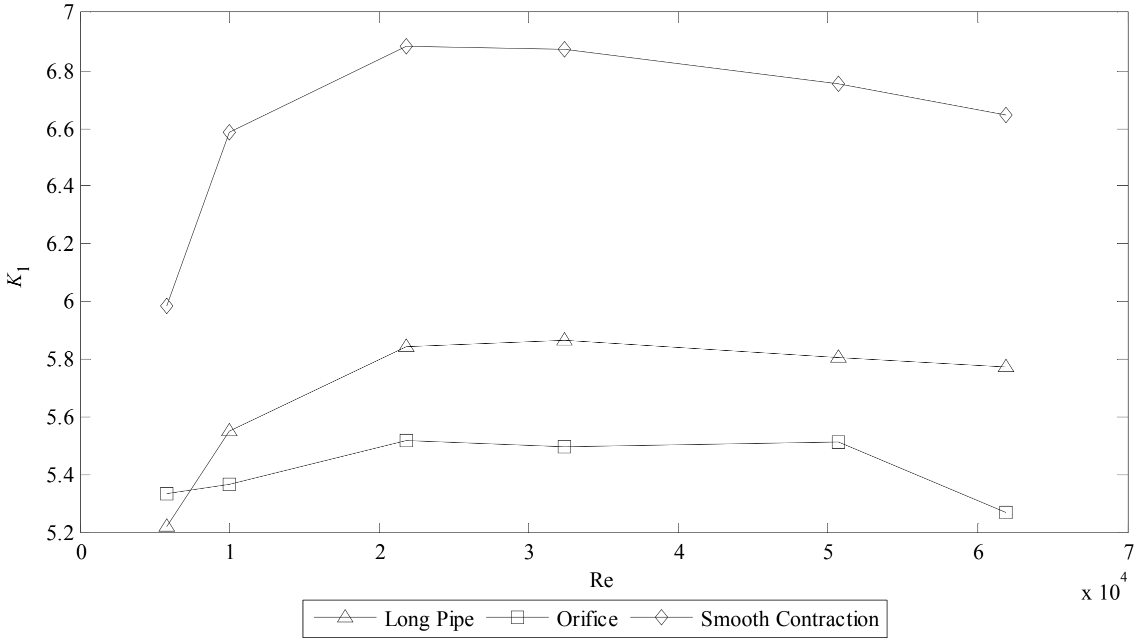

Figure 3.13 Reynolds number and initial condition effect on the centerline velocity decay coefficient, $K_{1.}$

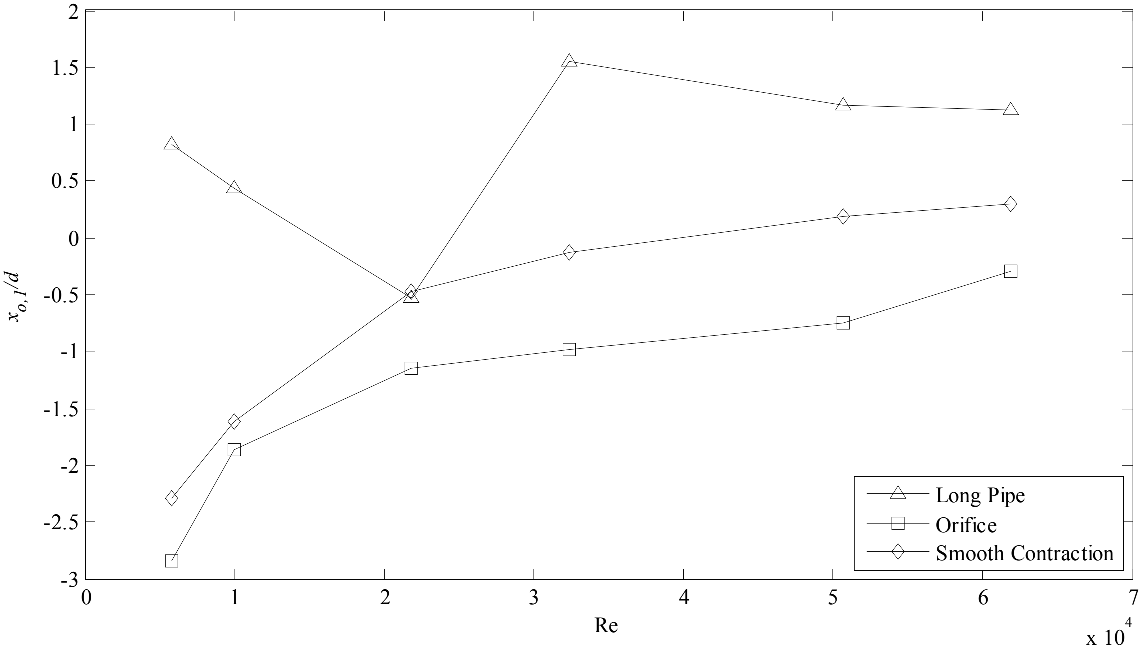

Figure 3.14 Reynolds number and initial condition effect on virtual origin, $x_{o,1}$, determined from centerline velocity decay for three inlet conditions.

3.3.4 The Effect of Initial Condition on Centerline RMS Velocity Profiles

The fluctuations of axial velocity along the jet centerline were compared for the three nozzles at all Reynolds numbers studied, and are shown in Figure 3.15. The axial RMS velocity component is scaled against centerline velocity at the same axial distance, while the nondimensionalized axial distance from is defined as $\chi = \left(x - x_{o,1}\right)/d$, where $x_{o,1}$ is the virtual origin position determined from the centerline velocity decay. The RMS velocity profiles collapse well above a Reynolds number of 5,800 for the smooth contraction and orifice nozzles, and above $\mathrm{Re} = 10{,}000$ for the long pipe. For these lower Reynolds numbers, centerline velocity fluctuations are higher in value up to a distance of $\chi \approx 25$ for the long pipe, $\chi \approx 23$ for the orifice, and $\chi \approx 30$ for the smooth contraction. Beyond these distances, u'_{cl}/U_{cl} values for all Reynolds numbers reach asymptotic values, approximately 0.23 ± 0.2 for all three inlets, which are reasonably close to 0.25 found by Xu and Antonia (2002) for the smooth contraction and long pipe nozzles, and 0.2 found by Mi et al. (2007) for the orifice.

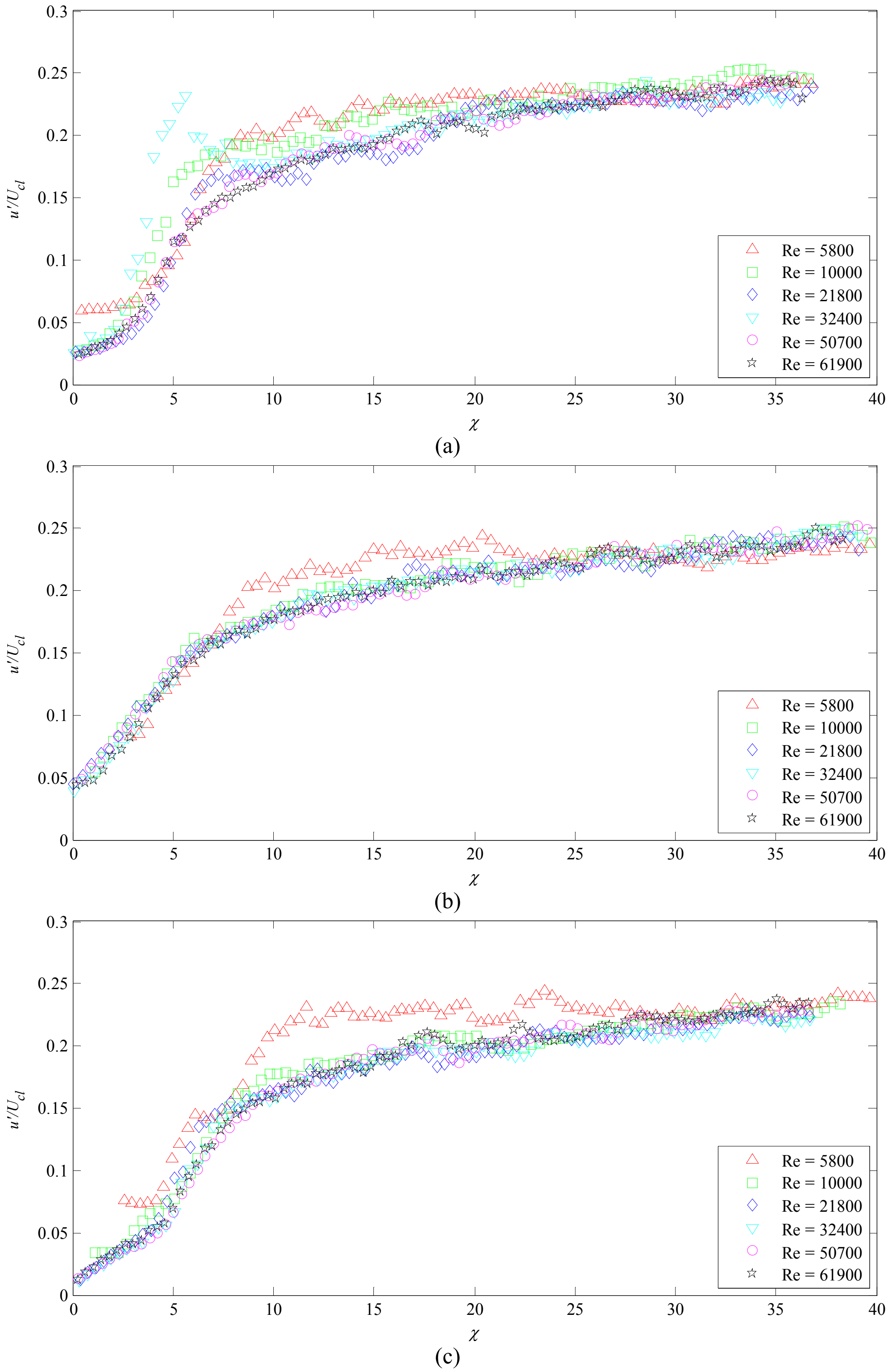

Figure 3.15 RMS velocity profiles along the jet's centerline for different Reynolds numbers for (a) long pipe, (b) orifice, and (c) smooth contraction nozzles.

3.3.5 The Effect of Initial Condition on the Length of the Potential Core

The relationship between the length of the potential core, x_p, and Reynolds number has also been examined for the three nozzles, and is shown in Figure 3.16. Here, potential core length is scaled with nozzle diameter. The potential core length is the furthest downstream axial location at which the centerline velocity is equal to the initial centerline velocity, or $U_0/U_{cl}=1$. This value is approximated as the axial position where the best-fit line for the nondimensionalized centerline velocity decay intersects the line $U_0/U_{cl}=1$. For the smooth contraction and orifice nozzles, potential core length increases with Reynolds number up to $\mathrm{Re}=21{,}800$, where it reaches two unique asymptotic values. The long pipe appears to have an outlying data point at either $\mathrm{Re}=21{,}800$ or $\mathrm{Re}=32{,}800$, which is discussed in Section 0.

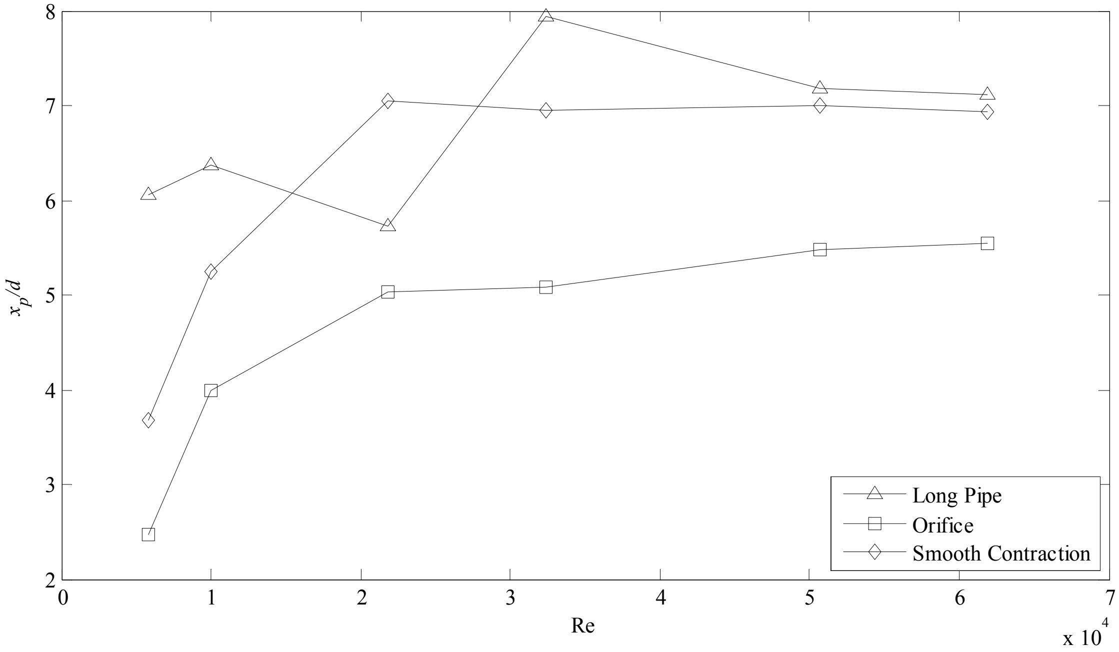

Figure 3.16 Reynolds number and initial condition effect on potential core length

3.3.6 The Effect of Initial Condition on Jet Half-Width

The jet half-width, $y_{1/2}(x)$ is a length scale which characterizes the spreading rate of the jet (Pope, 2000), satisfying equation (3.13). The half-width of the jet is the spanwise distance from the centerline at which the local axial velocity is equal to one-half of the centerline velocity at the same axial distance. The location of the half-width in a sample spanwise velocity profile is shown in Figure 3.17.

$$U(x, y_{1/2}) = \frac{1}{2} U_{cl}(x) \qquad (3.13)$$

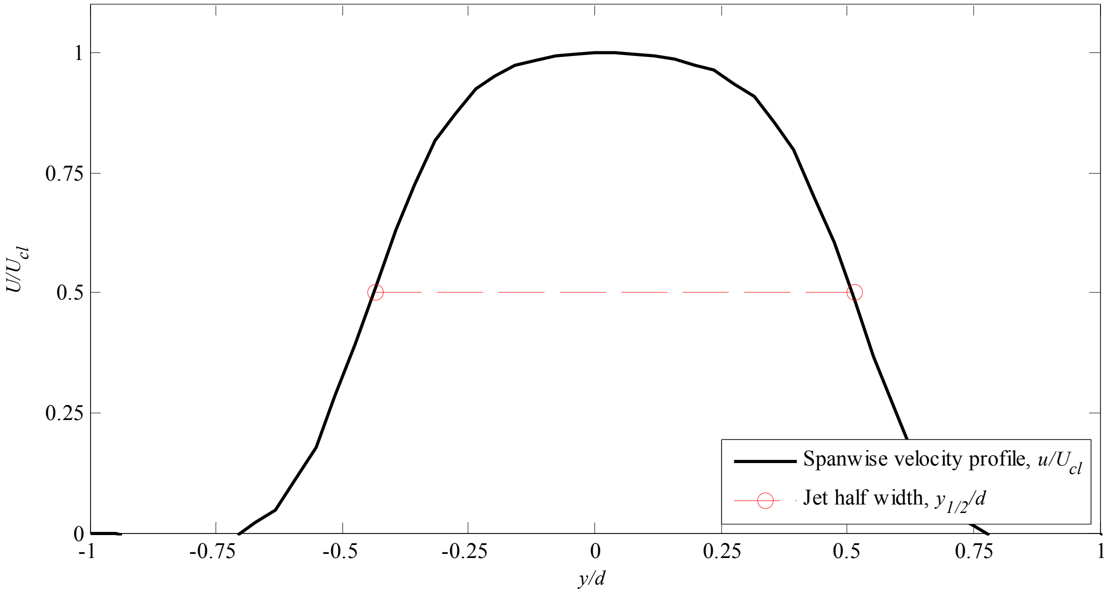

Figure 3.17 Figure showing the location of the jet half width in a sample spanwise velocity profile

The self-similar solution to the axisymmetric jet (see Section 1.3.2) relates the dimensionless axial distance from the idealized point-source of momentum, χ, to the half-width, as per equation (3.14). χ is defined in equation (3.15), and is the distance axial distance adjusted for the location of the virtual origin, $x_{o,2}$, scaled against the nozzle diameter. Owing to the assumed universality between turbulent axisymmetric jets as stated by the traditional approach to self-similarity, the values of K_2 should be the same, regardless of initial condition, provided that the flow is fully turbulent.

$$\frac{y_{1/2}}{d} = K_2 \chi \tag{3.14}$$

$$\chi = \frac{x - x_{o,2}}{d} \tag{3.15}$$

The half-width relationship to axial distance of a sample averaged vector field (in this case long pipe at $\mathrm{Re} = 5{,}800$) is presented in Figure 3.18. Positional coordinates are scaled against nozzle diameter, *d*. Three regions of the jet are apparent in the figure. The development region is characterized by a constant half-width. Beyond this is the transition zone, where the jet begins entraining fluid and the slope of $y_{1/2}$ begins to increase. Downstream of the transition zone, the jet achieves a self-similar state, where half-width increases linearly with axial distance, thereby satisfying equation (3.15).

It is possible to determine the half-spread coefficient, K_2, and the virtual origin position, $x_{o,2}$ by performing linear regression in the self-similar region, $x_1/d \le x/d \le x_2/d$. Here, x_1 is chosen as the first axial position at which $y_{1/2}$ exceeds the initial value of the half-width by a factor of 2, i.e. $y_{1/2}(x_1) > 2y_{1/2}(x=0)$, as to ensure that regression is performed sufficiently far beyond the transition zone, and x_2 is chosen as 90% of axial size of the ROI. The slope of the best-fit line is the spread coefficient, K_2, while its intercept with the line formed by $y/d = 0$ is the virtual origin position, $x_{o,2}$. Figure 3.18 shows the best-fit lines obtained from regression, as well as location of the virtual origin from a sample dataset. The best-fit lines and virtual origin locations for all nozzles at all Reynolds number are presented in Appendix D.

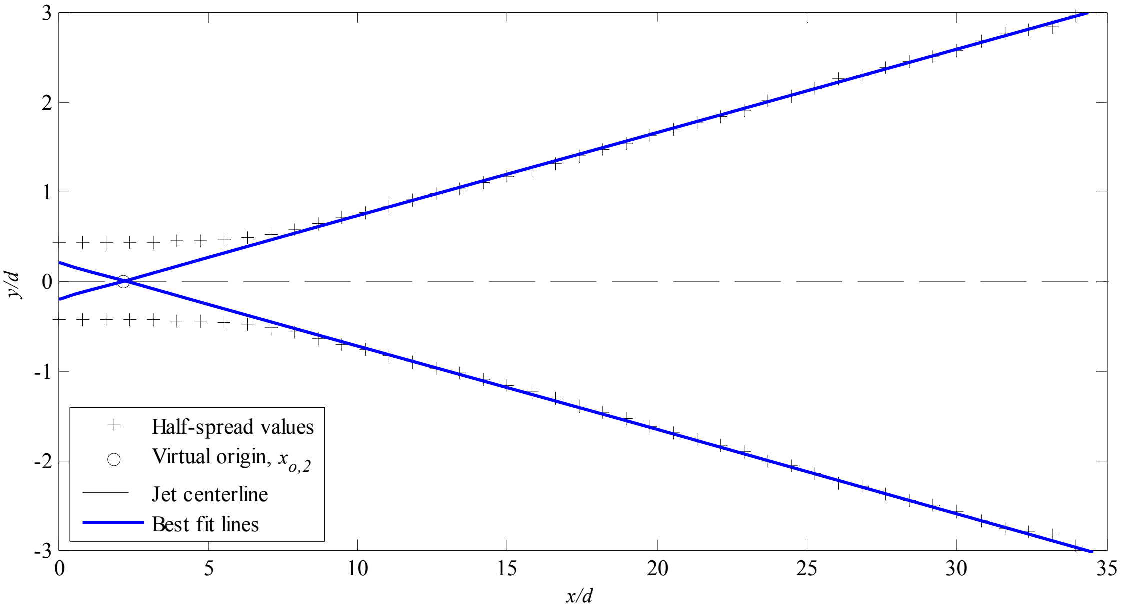

Figure 3.18 Half-width profile for a sample dataset, showing the lines of best fit and the location of the virtual origin, $x_{o,2}$.

The half-widths for the jets issuing from the three studied nozzles at various Reynolds numbers are shown in Figure 3.19. The half-width is scaled against the nozzle diameter, and axial position is shown as χ, defined in equation (3.15). This ensures that all half-width profiles all originate from the same conceptualized point source of momentum. For all three nozzles, half-width profiles collapse well for all Reynolds numbers studied, except for $\text{Re} = 5{,}800$ for the orifice nozzle.

The effect of Reynolds number and initial condition on K_2 is shown in Figure 3.20. The three curves for the three nozzles do show similar trends: The values of the spread coefficient asymptote in value at a Reynolds number beyond 10,000 for the orifice

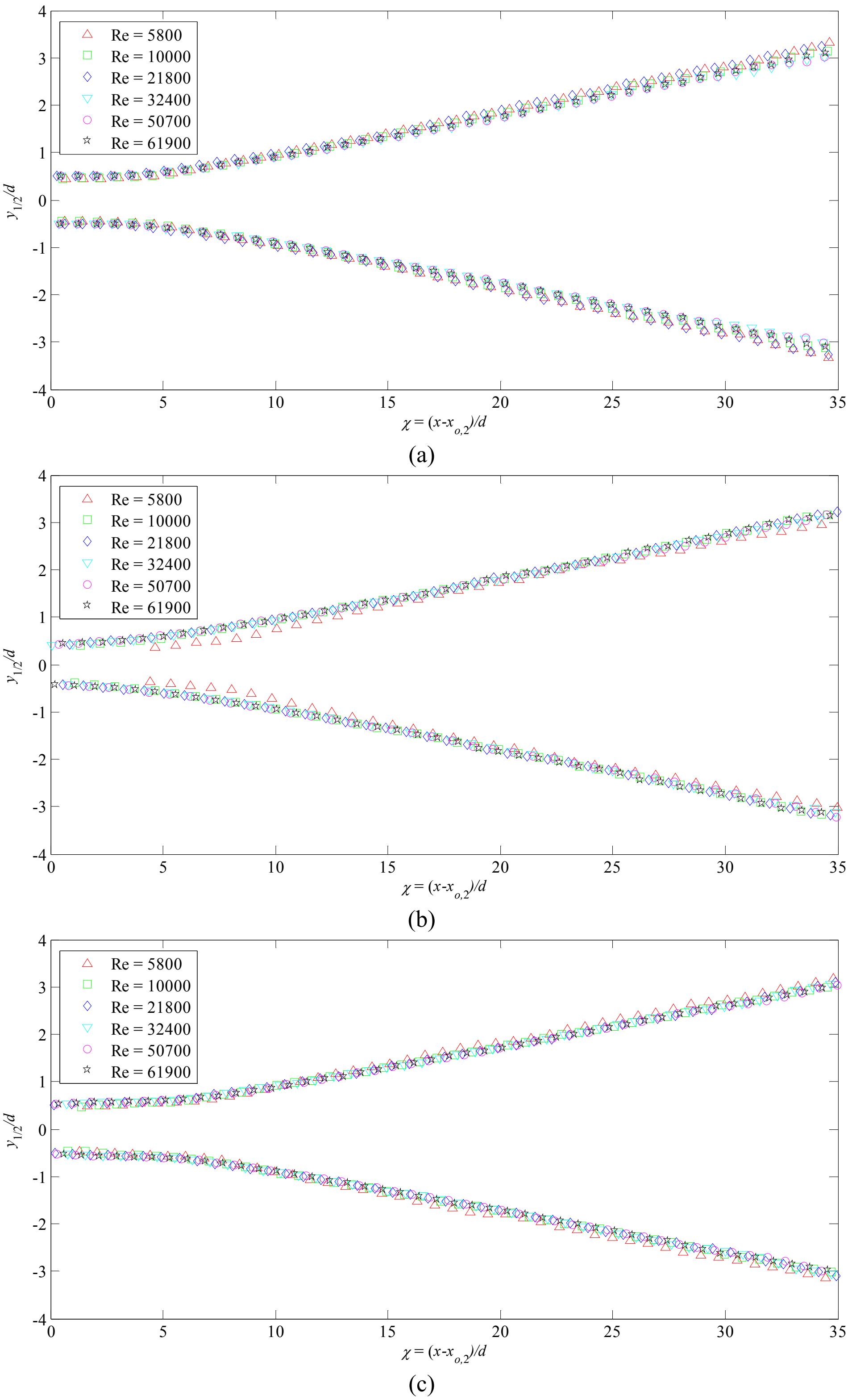

(a)

(b)

(c)

Figure 3.19 Nondimensionalized jet half-widths for long pipe (a), orifice (b), and smooth contraction (c) inlet conditions. Every 20th data point is plotted for clarity.

and smooth contraction, at which it can be argued that the jet is in a fully turbulent flow regime. It should be noted that the value of K_2 for the long pipe at $\mathrm{Re} = 21{,}800$ appears to be an outlier. If this point was neglected, the spread coefficient for the long pipe would begin to asymptote at $\mathrm{Re} = 32{,}400$. K_2 does not appear to have a significant Reynolds number dependence beyond above $\mathrm{Re} = 10{,}000$, although there does appear to be dependence on the nozzle used: The smooth contraction has the smallest spread over the range of Reynolds number studied, while the orifice has the highest value of this coefficient. The variation in spread coefficient between these three nozzles is likely not due to experimental error, since the data was collected in an identical manner for all initial conditions. If the variation in K_2 was of the same magnitude as experimental error, all spread coefficient values for the orifice would surely not be higher than those for the smooth contraction.

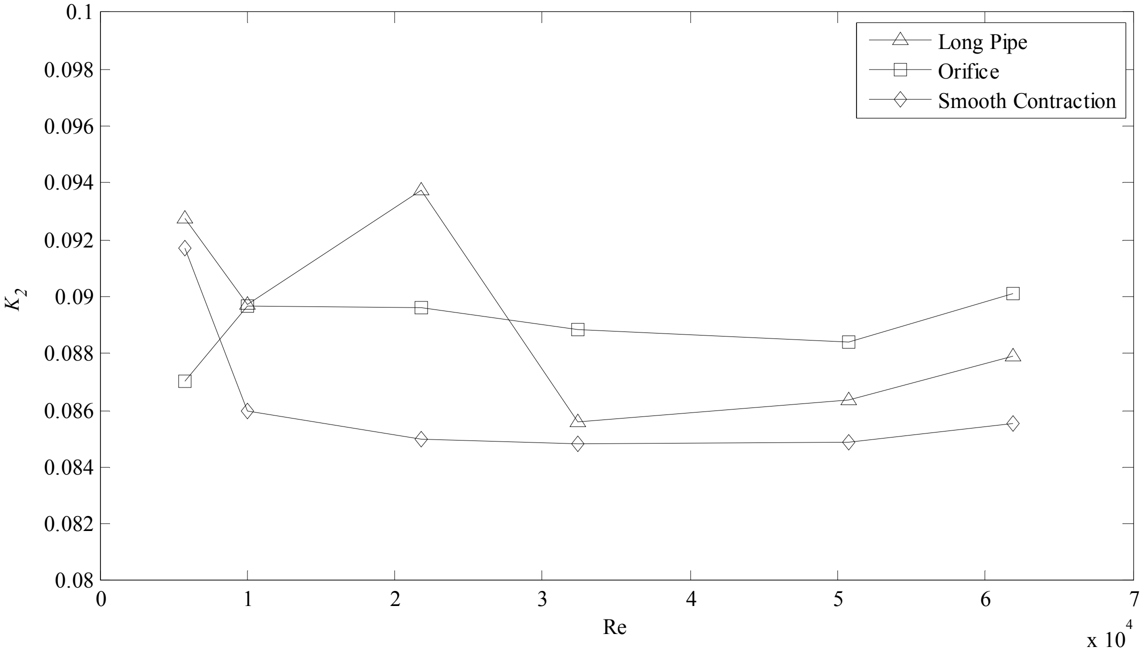

Figure 3.20 Reynolds number and initial condition effect on spread rate, K_2

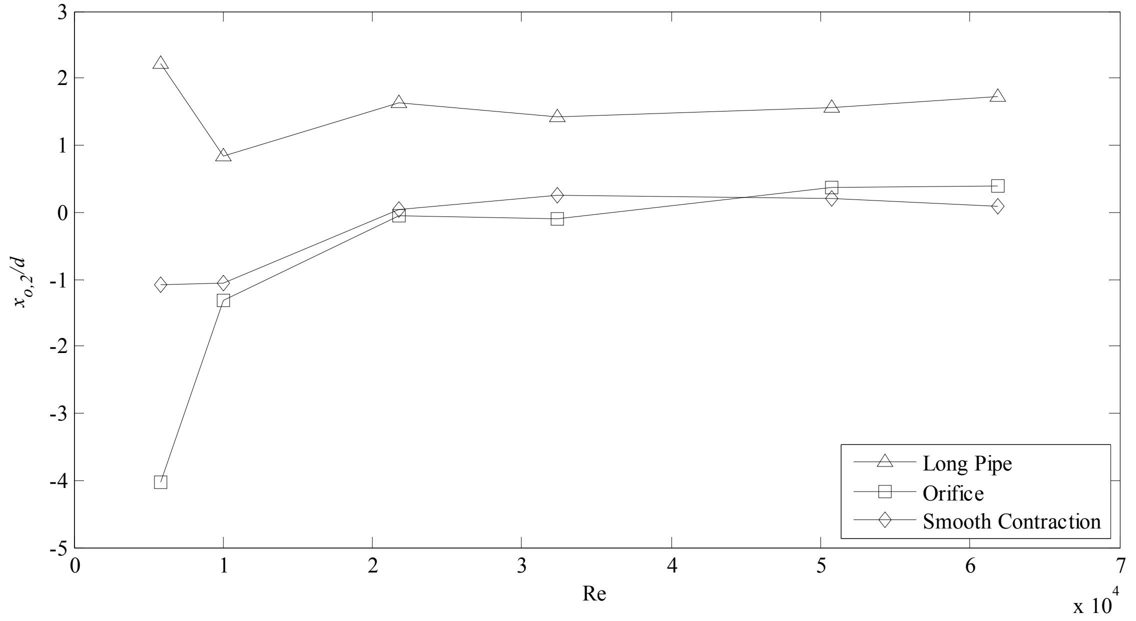

Figure 3.21 Effect of Reynolds number on virtual origin, $x_{o,2}$, determined from jet half-width for three inlet conditions

3.3.7 Discussion of the Suspicious Data Points Occurring for the Long Pipe Nozzle at Reynolds Numbers of 21,800 and 32,400

It is apparent from the profiles of the virtual origin position determined from the centerline velocity decay (Figure 3.14), potential core lengths (Figure 3.15), and spread coefficient (Figure 3.20) that the data points in all of these figures corresponding to the long pipe at Reynolds numbers of 21,800 and 32,400 do not seem to match the trend of the other data. In the case of the location of the virtual origin $x_{o,1}$ and the length of the potential core, x_p, their respective values are lower than the surrounding points for the long pipe, while for the spread rate, K_2, the value at this Reynolds number is higher than would be expected.

The centerline velocity decay profiles and half-width profiles for the long pipe nozzle are shown Figure D.1 and Figure D.4, respectively, in Appendix D. These show the best fit lines used to calculate the centerline velocity decay and half-width coefficients as well as the determined virtual origin positions for individual Reynolds numbers. The centerline decay profiles for all Reynolds numbers greater than 10,000 reveal that the transition from the development to the self-similar regions does not occur over a short axial distance. Instead, it appears that there is an extended transition region with length of approximately $x/d \approx 5$, where U_0/U_{cl} values are slightly higher than expected. Beyond this at $x/d \approx 10$ there is a readjustment, and the centerline velocity decay profile becomes linear and matches well with the line of best fit. It is most pronounced for Reynolds number of 21,800 and 34,200. This extended region is also evident for smooth contraction nozzle at higher Reynolds numbers, but not as significantly for the orifice, as shown in Figure D.3 and Figure D.2, respectively. Since the virtual origin and potential core length are determined from the intersections of the line of best fit with $U_0/U_{cl} = 0$ and $U_0/U_{cl} = 1$, respectively, the existence of this region surely affects where these intersection points lie. This especially true for the length of the potential core, since the intersection point used to determine it does not actually coincide with the true centerline velocity decay profile. Instead, it is offset by a small amount.

Similarly, observation of the half-width profiles for the long pipe, shown in Figure D.4, reveals the occurrence of a similar extended transition zone for certain Reynolds numbers. Ideally, the lines of best fit should match the half-width values immediately beyond the transition zone. Instead there is some difference between them in a short region beyond the transition zone, after which $y_{1/2}$ is linear and coincides with its line of best fit. Since the half-spread coefficient, K_2, is slope of the best-fit line, the presence of such a region would affect it. The deviation of the half-width from the line of best fit for $\mathrm{Re} = 21{,}800$ in this region appears to be the most pronounced, which coincides with the spurious data point. The transition regions are much smaller in the half-width profiles of the orifice and smooth contraction nozzles, shown in Figure D.5 and Figure D.6, respectively, and therefore no such outlying point is evident in the data obtained for those nozzles.

The profiles of RMS axial velocity along the jet centerline, shown in Figure 3.15(a), reveal a hump and a plateau occurring at Reynolds numbers of 10,000, 21,800 and 32,400 in the region $4 \le \chi \le 10$. All other profiles show a steady increase to their asymptotic value of $u'/U_{cl} \approx 0.23$. A similar hump was observed by Mi et al. (2001b) in the scalar RMS field for the smooth contraction nozzle, but not the long pipe. The existence of this hump and plateau could be the result of some fluctuating phenomenon occurring in the near field existing at only at those two Reynolds numbers, affecting the spread and decay observed downstream.

3.4 Conclusions

The effect of initial condition of the self-similar behavior of an axisymmetric jet was studied by comparing the flow fields generated by a long pipe, orifice, and smooth contraction nozzle over a range of Reynolds numbers. The jets issuing from these nozzles had the same initial mass and momentum fluxes, and differed only in the velocity profiles and turbulence structure at their outlets. The velocity profiles conform to their theoretical distributions, with the long pipe producing a seventh-order polynomial profile, the smooth contraction a ‘top-hat’ profile, and the orifice a parabolic profile in-between that of the other two nozzles.

Self-similar behavior was examined by comparing the centerline velocity decay and spread rates of the jets generated by the three nozzles, as well as the location of their virtual origins and the lengths of the potential cores. The jet issuing from the orifice was found to decay the fastest and the slowest from the smooth contraction. The centerline velocity decay coefficient, K_1, reached an asymptotic value for the three jets at high Reynolds numbers ($\mathrm{Re} > 21{,}800$); however, the jet from each nozzle reached a different value. A similar conclusion was made for the spread rates of from the three nozzles: The orifice jet spread the fastest, while the smooth contraction spread the slowest. Values of the spread coefficient, K_2, varied between the three jets, reaching different asymptotic values. The positions of the virtual origins also differed between the three jets, with those of the long pipe being consistently higher than those of the smooth contraction, which were in turn higher than those of the orifice. These values asymptote to unique values for each of the initial conditions at high Reynolds numbers. A similar conclusion was made for the potential core lengths of the three jets, which asymptote to unique values for each of the initial conditions at Reynolds numbers greater than 25,000.

It is concluded that initial conditions do indeed have an effect on the downstream behavior of axisymmetric jets, and therefore the self-similar solutions used to model these flows are not universal for jets issuing from different source conditions. As dictated by the self-similarity theory, jets should decay and spread at the same rates. Jets with different initial conditions have been shown to reach different asymptotic states, which supports local-self similarity, but not universality

CHAPTER 4: THE EFFECT OF CHAMBER LENGTH AND REYNOLDS NUMBER ON A FLUIDIC PRECESSING JET

4.1 Introduction

The flow field occurring just beyond the exit plane of a precessing jet is studied to determine the effect of chamber length and Reynolds number on the probability of precession, as this relationship is still poorly understood. The effect of these two parameters on the entrainment back into the chamber and the size of the issuing jet is also examined. In order to determine the probability of precession at a given Reynolds number and chamber length, a processing algorithm was devised capable of discerning the two flow modes (precessing mode and axial mode) based on the distribution of axial velocity in the region of interest. This allows for the entrainment ratio to be compared for the two flow modes and provides conditionally averaged mean and RMS velocity distributions of precessing mode at different combinations of chamber length and Reynolds number.

4.2 The Fluidic Precessing Nozzle

The nozzle and chamber assembly used to generate the precessing flow is shown in Figure 4.1. It is comprised of an axisymmetric jet exiting from a smooth contraction nozzle of exit diameter d = 5.08 mm (1/5”), which issues through a sudden expansion into a chamber with diameter $D/d = 5$. This expansion ratio has been shown by Nathan et al. (1998) to be the most favorable to generate precession. Seven chamber lengths are studied, with lengths L/D = 1, 2, 2.5, 2.75, 3, 3.5, and 4.5. Newbold (1997) has shown the optimum chamber length for precession to be L/D = 2.75, with precession occurring over the range $2 \le L/D \le 3.5$. The chamber lengths studied encompass this range, as well as chamber lengths below and above it.

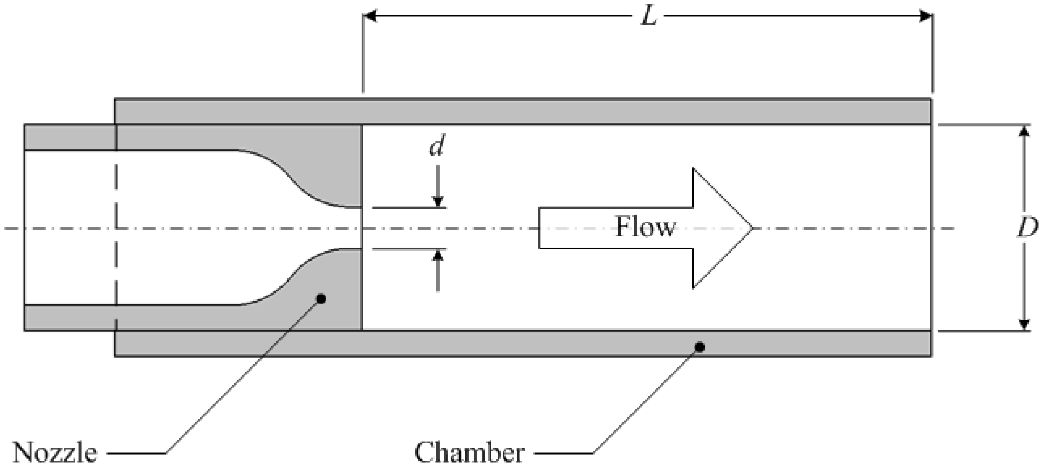

Figure 4.1 Sectioned view of the fluidic precessing jet assembly, showing the nozzle and chamber.

Similar sorts of jet flows into abrupt expansions have been studied by Mi & Nathan (2004), Nathan et al. (1998), Wong et al. (2003), Wong et al. (2004), and Wong et al. (2006). The precessing nozzle and chamber configurations used for these, however, have involved a lip and centerbody, which have been shown to stabilize the flow and increase its probability of precession (Wong et al., 2008). The configuration used lacks a centerbody and lip, resulting in a more chaotic and unstable flow, which is appropriate for fundamental study of the effect of chamber geometry on the probability of occurrence of this flow phenomenon.

Flow into the nozzle first passes through the plenum, described in Section 2.3, which minimizes any swirl or disturbance in the flow. The seven chambers are interchangeable and are held onto the nozzle section with a pressure fit. Schematic drawings of the smooth contraction nozzle and chambers can be found in Appendix C.

4.3 Experimental Method

4.3.1 StereoPIV Setup

Typical StereoPIV configurations orient the light sheet so that the largest component of velocity is in-plane, which is typically the axial velocity component of the jet (Prasad, 2001). Due to the rotational and chaotic nature of the precessing jet flow, neither the position of the jet within the chamber exit plane nor the angle formed between the jet and chamber axes can be anticipated. Therefore, it is impossible to orient the light sheet so that the axial component of velocity is parallel to the light sheet while ensuring that it remains in the region of interest.

For this work the light sheet is instead oriented just beyond the chamber so that the chamber axis is normal to it, and flow is normal to the light sheet. In this configuration, the entire exit plane of the chamber is visible in the field of view, and the projection of axial velocity onto the chamber axis corresponds to the out-of-plane velocity component, *w*. Since the highest velocity component is no longer an in-plane velocity component, a thicker light sheet is required (van Doorne et al., 2003).

Two cameras are used with 105 mm lenses (Sigma) and Scheimpflug adapters, and are positioned at a downstream distance from the nozzle of approximately 30 cm. They are at the same height as the nozzle, and both form an angle of 16° to the chamber axis. The relative positions of the precession chamber assembly, light sheet, and cameras are shown in Figure 4.2. One thousand dual-frame images were collected for each chamber length and Reynolds number.

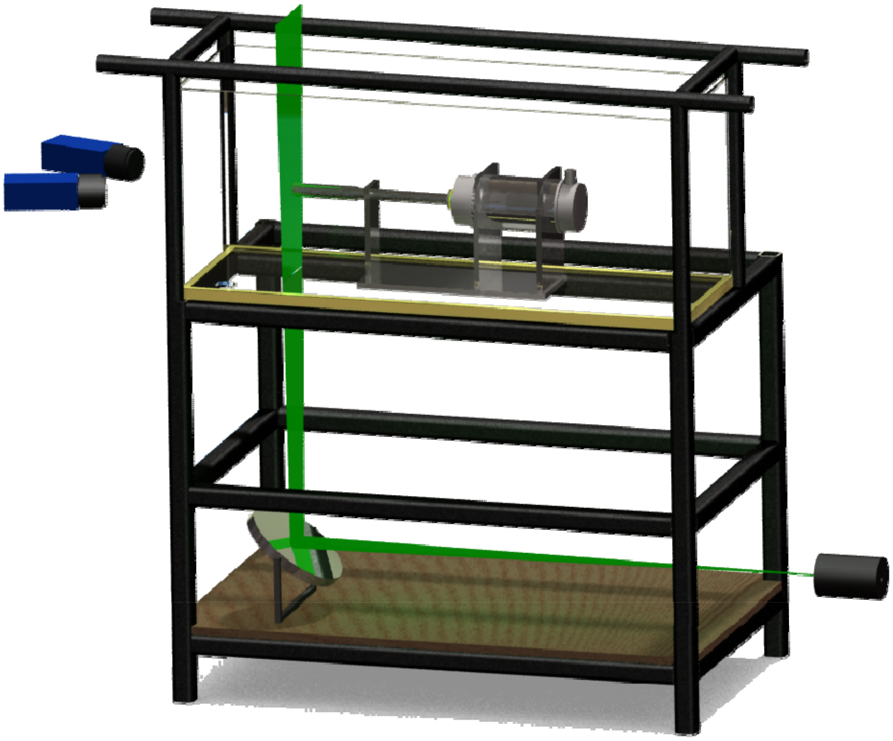

Figure 4.2 Solid model showing StereoPIV setup with the light sheet normal to the flow direction.

4.3.2 Light Sheet Thickness and Time Step

It has been shown that in StereoPIV configurations, it is desirable for robust processing that the following two criteria are met (Raffel et al., 1998):

1. Particles travel approximately one-quarter of the size of an interrogation window between frames in order to capture in-plane velocity components *u* and *v* (in the *x*- and *y*-directions, receptively).

2. Particles travel approximately one-quarter of the light sheet thickness between frames in order to capture out-of-plane velocity component w (in the z-direction).

These two criteria are aimed to ensure that the same group of particles remains within an interrogation window between laser flashes. If different groups of particles are imaged in the two frames and then cross-correlated, an erroneous velocity vector results. The out-of-plane velocity component is of most interest in this study, and therefore the light-sheet thickness and time step are optimized for capturing this component.

Any displacement in the z-direction in the real-world coordinate system is mapped into an in-plane displacement on the camera CCD plane. Due to the much stronger out-of-plane than in-plane velocity, any in-plane displacement resulting from particle motion in the x-direction, Δx, is assumed to be much smaller than in the z-direction. Since the cameras are at the same height as the chamber axis and form an angle α with the z-axis, any out-of-plane displacement, Δz, is mapped only into a horizontal displacement, $\Delta x'$, on a plane parallel to the CCD plane, given in equation (4.1). The magnification factor, M, between this plane and the CCD plane is defined in equation (4.2). Combining equations (4.1) and (4.2) yields equation (4.3), which relates the mapped pixelwise displacement of a particle onto the camera CCD plane to its real-world axial displacement. The difference between the highest and lowest x-values, $x_{\max} - x_{\min}$, is the width of the field of view.

$$\Delta x' = \Delta z \sin\alpha + \Delta x \cos\alpha \approx \Delta z \sin\alpha \tag{4.1}$$

$$M = \frac{x_{\max} - x_{\min}}{\Xi} = \frac{\Delta x'}{\Delta \xi} \tag{4.2}$$

$$\Delta\xi = \frac{\Delta z \sin\alpha}{M} \tag{4.3}$$

The out-of-plane velocity component, *w*, is determined from the correlated displacement of a group of particles in the two frames of an interrogation window, and the known time step between them. This follows the simple velocity equation (4.4), which relates the change of position to the change in time required for the motion.

$$w = \frac{\Delta z}{\Delta t} \tag{4.4}$$

Equation (4.4) can be rearranged to give equation (4.5). Here, the second criterion can also be imposed, which requires that the displacement in the *z*-direction be exactly one-quarter the thickness of the light sheet, i.e. $\Delta z = mT$, where $m = 1/4$ and T is the thickness of the light sheet. In this equation, both light sheet thickness and time step are coupled to the axial displacement of the particles.

$$\Delta z = w\Delta t = mT \tag{4.5}$$

Equation (4.3) is rearranged and the in-plane displacement on the CCD is set to the desired quarter-width of the interrogation window, $\Delta\xi = \Delta\xi_0$ (in this study the interrogation window is 32×32 px, so the desired particle displacement is $\Delta\xi_0 = 8$ px). This satisfies the first criterion mentioned earlier. In addition, the maximum out-of-plane velocity is assumed to be the bulk exit velocity out of the nozzle, $w = \upsilon_e$. Combining equation (4.3) with (4.5) gives equation (4.6), which now relates both time step and light sheet thickness to the desired pixelwise particle displacement within an interrogation window and the angle between cameras.

$$\Delta\xi_0 = \frac{\upsilon_e \Delta t \sin\alpha}{M} = \frac{mT\sin\alpha}{M} \tag{4.6}$$

Uncoupling equation (4.6) gives equations (4.7) and (4.8), which now define the required time step and light sheet thickness for a maximum out-of-plane velocity $w = \upsilon_e$.

$$\Delta t = \frac{M\Delta\xi_0}{\upsilon_e \sin\alpha} \tag{4.7}$$

$$T = \frac{M\Delta\xi_0}{m\sin\alpha} \tag{4.8}$$

The calculated value of Δt is merely an estimate, since the axial velocity will nowhere in the ROI exceed the bulk inlet velocity. The actual time step values used for this experiment were based on the result of equation (4.7), and adjusted using a trial-and-error approach. Too large of a time-step allows for too large of a particle displacement within an interrogation window and through the light sheet, which in turn results in an invalid vector in an interrogation window. The Δt at each Reynolds number and chamber length was chosen so that less than 1% of the interrogation windows in an instantaneous vector field contained a null vector[2]. Table 4-1 shows the time steps used for each of the chamber lengths, as well as the calculated values based on υ_e.

It is apparent from equation (4.8) that the light sheet thickness is not dependent upon the out-of-plane velocity, provided that the Δt is chosen so that the in-plane particle displacement, $\Delta\xi$, is 8 px. A light sheet thickness of approximately 2.75 mm was used. Too thin of a light sheet could cause particles to move through the entire light sheet thickness between laser pulses, resulting in spurious vectors. Too thick of a light sheet

---

[2] In the StereoPIV processing software used (DaVis 7.4, LaVision), any interrogation window in which velocity cannot be determined results in a null vector.

may result in different particle velocities at its near and far sides, which would result in erroneous correlated vectors.

Table 4-1 Comparison of time step values calculated based on the bulk inlet velocity to those used for each chamber length.

Pump Speed, *Ω*	210	480	750	990	1320	1800	
Re	10,000	21,800	32,400	40,800	50,700	61,900	
Calculated Δ*t* [µs]	343	158	106	85	68	55	**Chamber Length, *L*/*D***
Actual Δ*t* used [µs]	65	40	30	25	20	15	1.0
	275	170	120	75	60	45	2.0
	275	170	120	80	60	45	2.5
	275	165	115	70	65	45	2.75
	275	155	100	65	55	45	3.0
	275	165	105	75	60	45	3.5
	300	175	140	125	105	80	4.5

4.3.3 StereoPIV Processing

StereoPIV processing was achieved using the algorithm illustrated in Figure 4.3. Raw images from the cameras were first preprocessed using background count subtraction and sliding background subtraction of time series (over 3 images), in order to remove any background intensities which may exist in sequential images, as well as remove any intensity which remained constant, such as the image of the chamber. Background noise was reduced using sliding background subtraction with a 5 px filter size. The intensity of particles is normalized using a min-max filter with a 10 px window, and the particle images were finally smoothed using a 3×3 linear filter. See Section 2.4.2 for a more detailed description of the preprocessing steps used.

Vector fields were generated using a multi-pass correlation scheme with a decreasing window size. Five passes were used to improve the quality of calculation of out-of-plane vectors, which were of the most interest in this study. Correlation was performed twice with a 64×64 px interrogation window, and then further processed with three passes of a 32×32 px interrogation window. The resulting vector field from each correlation step was used as an initial particle search field for the next. This resulted in 67,804 vectors in each instantaneous vector field. Vector fields were finally treated with a median filter, to remove any spurious vectors, as well as a 3×3 smoothing filter.

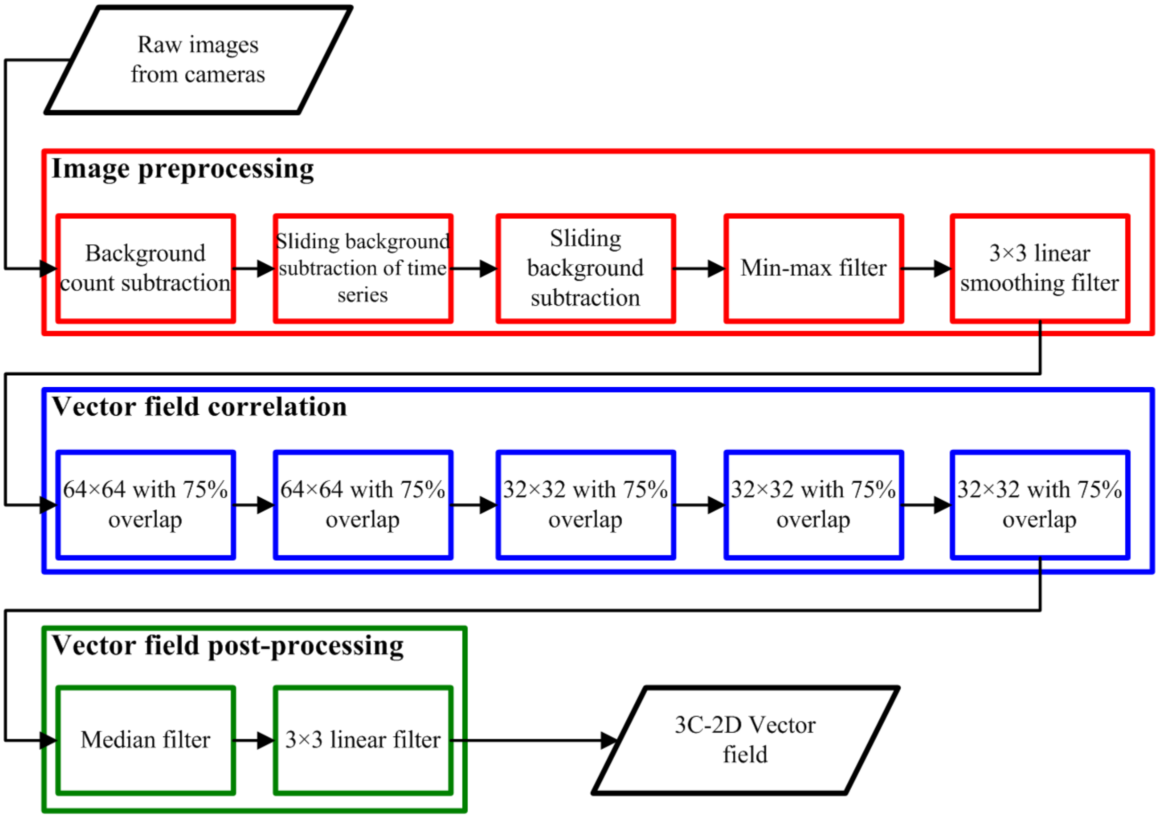

Figure 4.3 StereoPIV processing algorithm for precessing jet data.

4.3.4 Location of Chamber Center

It was necessary to determine the chamber center and radius in terms of the coordinate system of the calculated vector field. It was not feasible to attempt to calibrate the StereoPIV system with the origin corresponding to the chamber axis, since, during the calibration process, the view of the chamber is obscured by the calibration target. Instead, calibration was performed with the chamber center being reasonably close to the calibration target's origin. From images of the chamber (with room illumination and low seeding density), its origin coordinates were determined, using a circle-fitting method, and in turn used to offset all data so that the chamber axis corresponded to $(x,y)=(0,0)$ mm. This procedure was carried out for each chamber length, since changing the chamber between experimental runs resulted in a small positional variation.

Circle fitting was accomplished by mapping images from both cameras onto one another to ensure proper calibration. The inner and outer diameters of the chambers from both images should overlap perfectly. One image was chosen, and an arbitrary number of points were marked on the chamber inner diameter. Using the method proposed by Pratt (1987), the pixelwise coordinates of the chamber center, ξ_0 and ψ_0, were determined from these selected points, as well as the chamber radius, λ_0, also in pixels. Conversion from camera CCD plane coordinates to real world coordinates was achieved using equations (4.9) and (4.10), and the chamber radius was determined from equation (4.11). Ξ and Ψ are the image size in the horizontal and vertical directions in pixels, respectively.

$$x_c = \left(\frac{\xi_0}{\Xi}\right) I\delta x + \min(\mathbf{X}) \tag{4.9}$$

$$y_c = \left(\frac{\psi_0}{\Psi}\right) J\delta y + \min(\mathbf{Y}) \tag{4.10}$$

$$R = \left(\frac{\lambda_0}{\Xi}\right) I\delta x \tag{4.11}$$

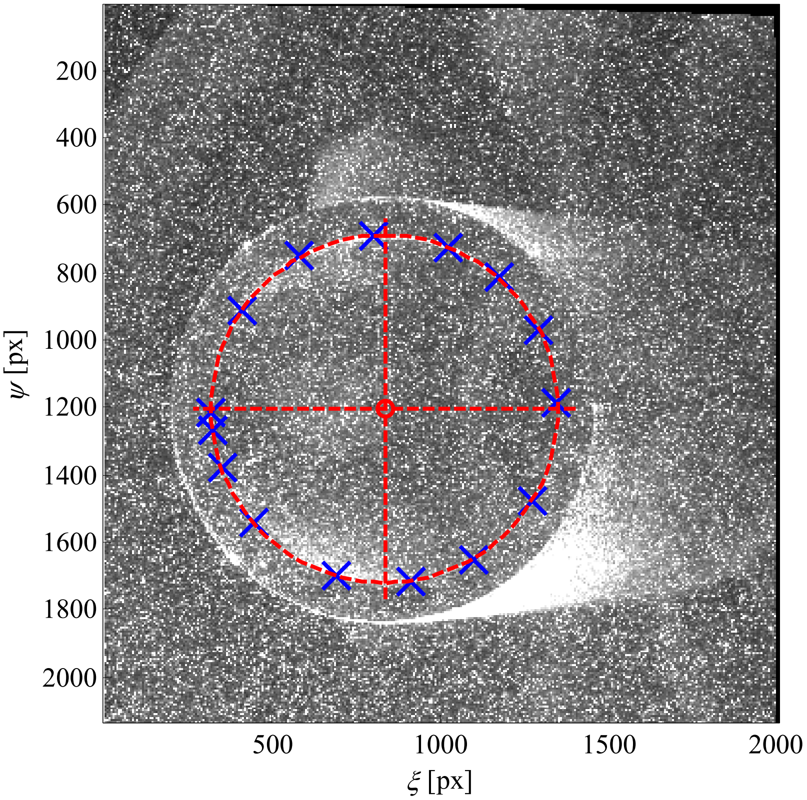

Figure 4.4 Location of chamber center (marked with '○') determined from points selected on chamber edge (marked with 'x').

Figure 4.4 shows the image of the *L*/*D* = 2.75 chamber as seen by one of the cameras. The inner edge of the chamber was marked with points (shown in the figure as X). Using the method explained in the paragraph above, the chamber center (shown as ○) and radius were calculated. The chamber perimeter and the *x*- and *y*-axes are shown overlaid as broken lines. It is apparent from the figure that the calculated values of radius and center are reasonable.

4.3.5 Data Masking

It was necessary to mask all instantaneous vector fields to remove any data beyond the chamber radius. This was accomplished by creating a new axial velocity array, $\breve{\mathbf{w}}$, to contain all data within just beyond the radius (a factor of 1.1 was chosen, since the region of interest is just beyond the chamber exit plane, and the issuing jet undergoes some expansion in this distance). This new array has the same size as **w**, which contains all axial velocity data over the entire field of view. The masked array is filled with corresponding axial velocity values from **w** which are within a distance of 1.1*R* from the chamber center at position (x_c, y_c). Any velocity values beyond this are set to null. The creation of $\breve{\mathbf{w}}$ is defined in equation (4.12), where *i* and *j* are array indices, and $\mathbf{X}_{i,j}$ and $\mathbf{Y}_{i,j}$ contain *x* and *y* positional coordinates at grid point (i, j).

$$\breve{\mathbf{w}}_{i,j} = \begin{cases} \mathbf{w}_{i,j}, & \sqrt{\left(\mathbf{X}_{i,j} - x_c\right)^2 + \left(\mathbf{Y}_{i,j} - y_c\right)^2} \leq 1.1R \\ 0, & \text{otherwise} \end{cases}, \quad \forall i, j \tag{4.12}$$

4.4 Two Modes of Flow

Instantaneous velocity profiles of the issuing jet reveal two dominant modes of flow: Precessing (PJ) mode and axial (AJ) mode. There is a third mode, which will be referred to as transitioning mode, in which the jet is neither obviously in precessing mode nor axial mode. Sample axial velocity contours and in-plane velocity vectors for the jet in precessing mode, axial mode, and transition mode are shown in Figure 4.5, Figure 4.6, and Figure 4.7, respectively. In these figures, all velocity components have been smoothed with a 10×10 linear filter to highlight the dominant shape and structure of the flow and minimize the presence of any turbulence or small scale structures. In addition, to highlight the shape of the issuing jet, only positive axial velocity is shown; any negative axial velocity has been set to zero.

Precessing mode is illustrated in Figure 4.5, and is characterized by a high positive axial velocity region near to the chamber wall (see subfigures a-c), which resembles a kidney-bean in shape, resembling a jet in cross-flow (Rajaratnam, 1976). This region occupies approximately half of the perimeter of the chamber. There is no outflow in the region around the chamber axis; instead, fluid is being entrained back into the chamber. In-plane velocity vectors (see subfigures d-f) show a pair of dominant counter-rotating vortices which exist in the region between the crescent-shaped outflowing jet and the chamber center. The shape and vortical structure of this flow mode agree with the observations of Mi et al. (2008).

Axial mode, as shown in Figure 4.6, resembles an axisymmetric jet flow, where the jet axis is near to the chamber axis, and its shape is reasonably round. From the in-plane velocity vectors (subfigures d-f), it is apparent that there are no dominant vortical structures. Instead, smaller vortices are apparent which correspond to the edges of the outflowing region, the size of which increases with chamber length. The maximum axial velocity in this mode can reach $w/\upsilon_e \cong 0.9$ for a chamber length of $L/D = 1$ (see Figure 4.6 (a)), which is essentially an axisymmetric jet.

A third mode of flow is also possible, which is presumed to occur as the jet transitions between axial and precessing modes. Figure 4.7 shows examples of this mode. The outflowing jet is not necessarily crescent-shaped, as would be expected in precessing mode, having instead a round shape as would be expected in axial mode. The region of highest outflow, however, is not sufficiently close to the chamber axis (marked with '+' in the figure), as would be characteristic of axial mode. The in-plane velocity vectors show no dominant counter-rotating vortex pair which is characteristic of precessing mode.

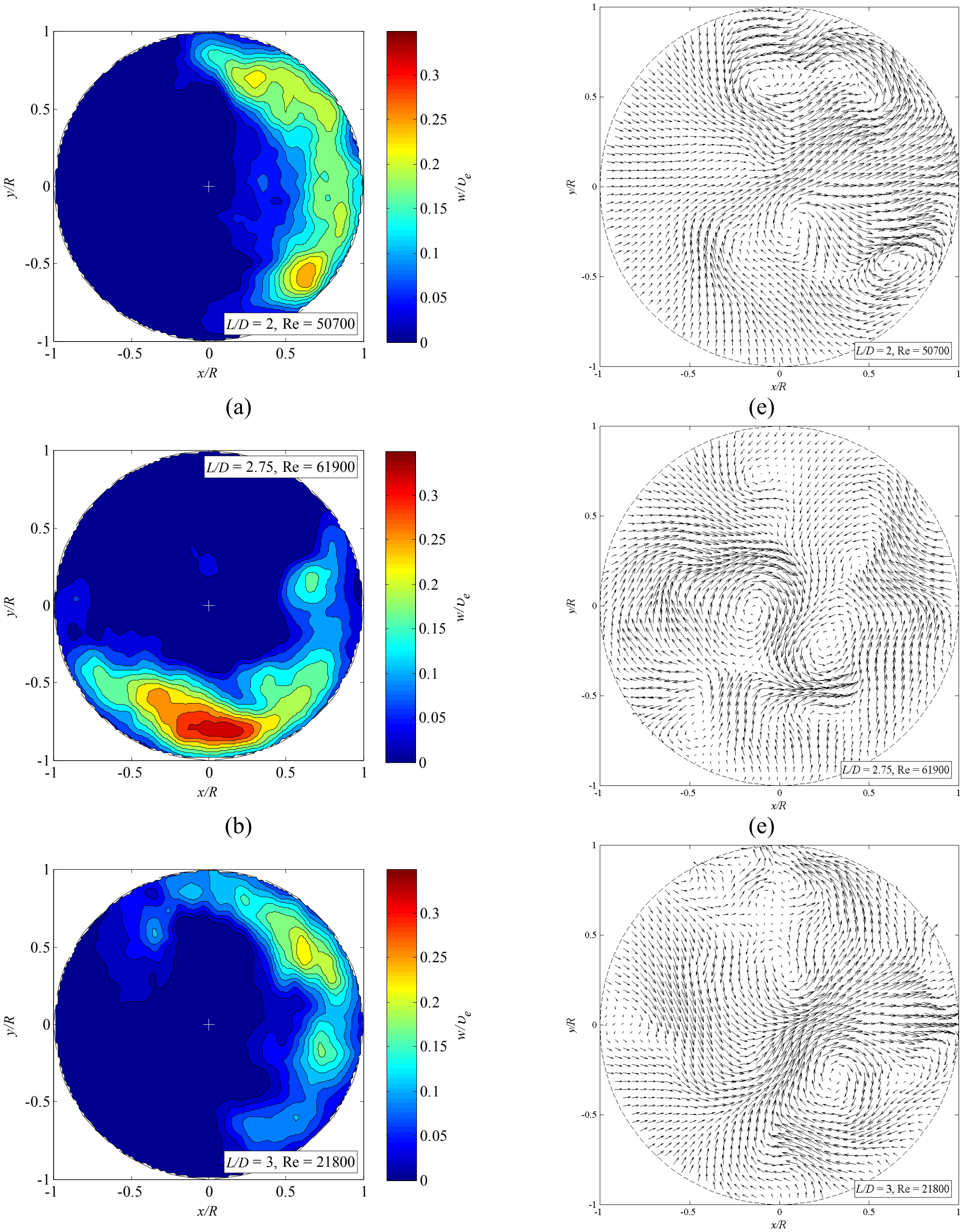

(a) (e)

(b) (e)

(c) (f)

Figure 4.5 Contour plots of axial velocity distribution (a-c) and vector plots of in-plane velocity (d-f) illustrating the outflowing region of the jet in precessing mode.

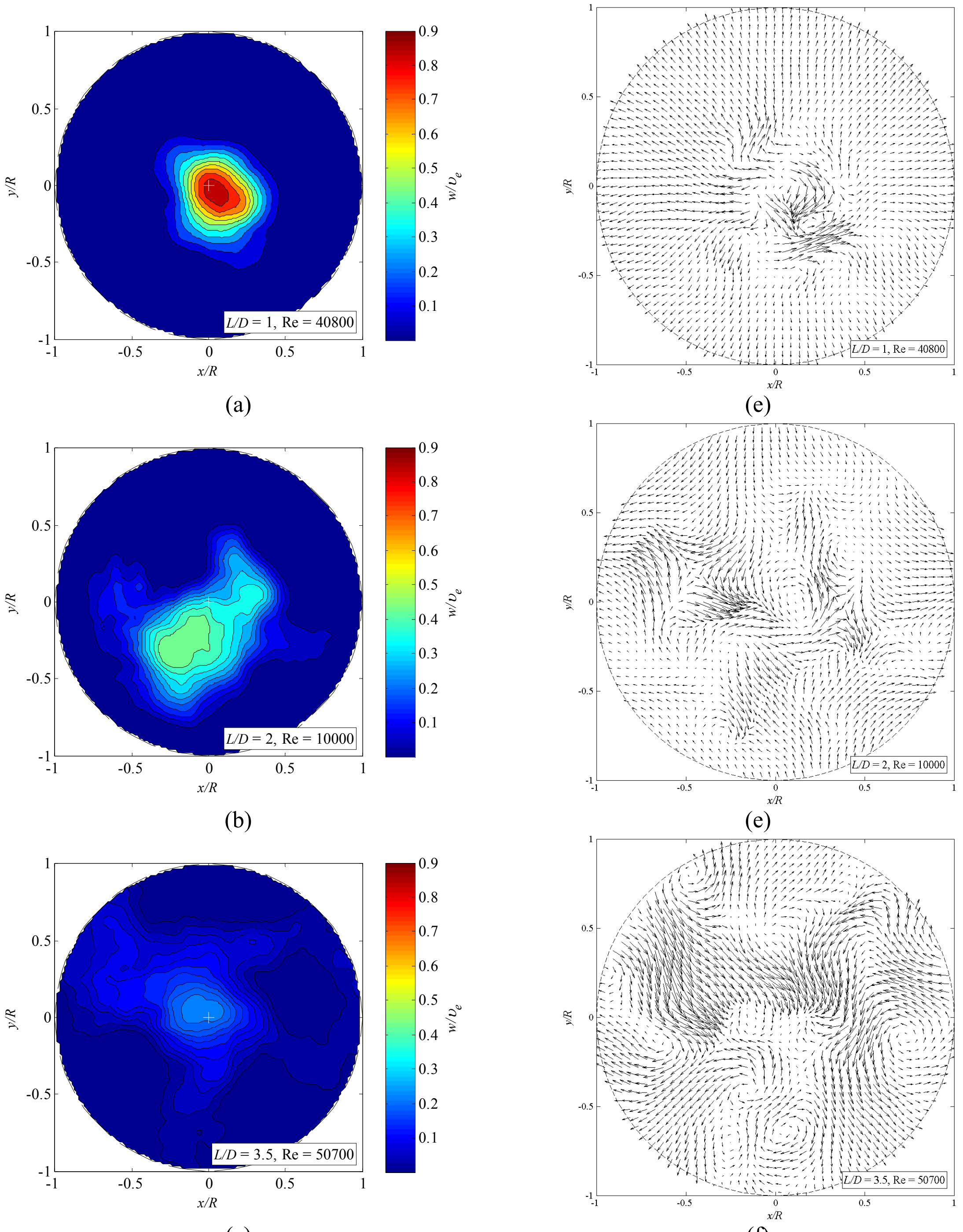

(a) (e)

(b) (e)

(c) (f)

Figure 4.6 Contour plots of axial velocity distribution (a-c) and vector plots of in-plane velocity (d-f) illustrating the outflowing region of the jet in axial mode.

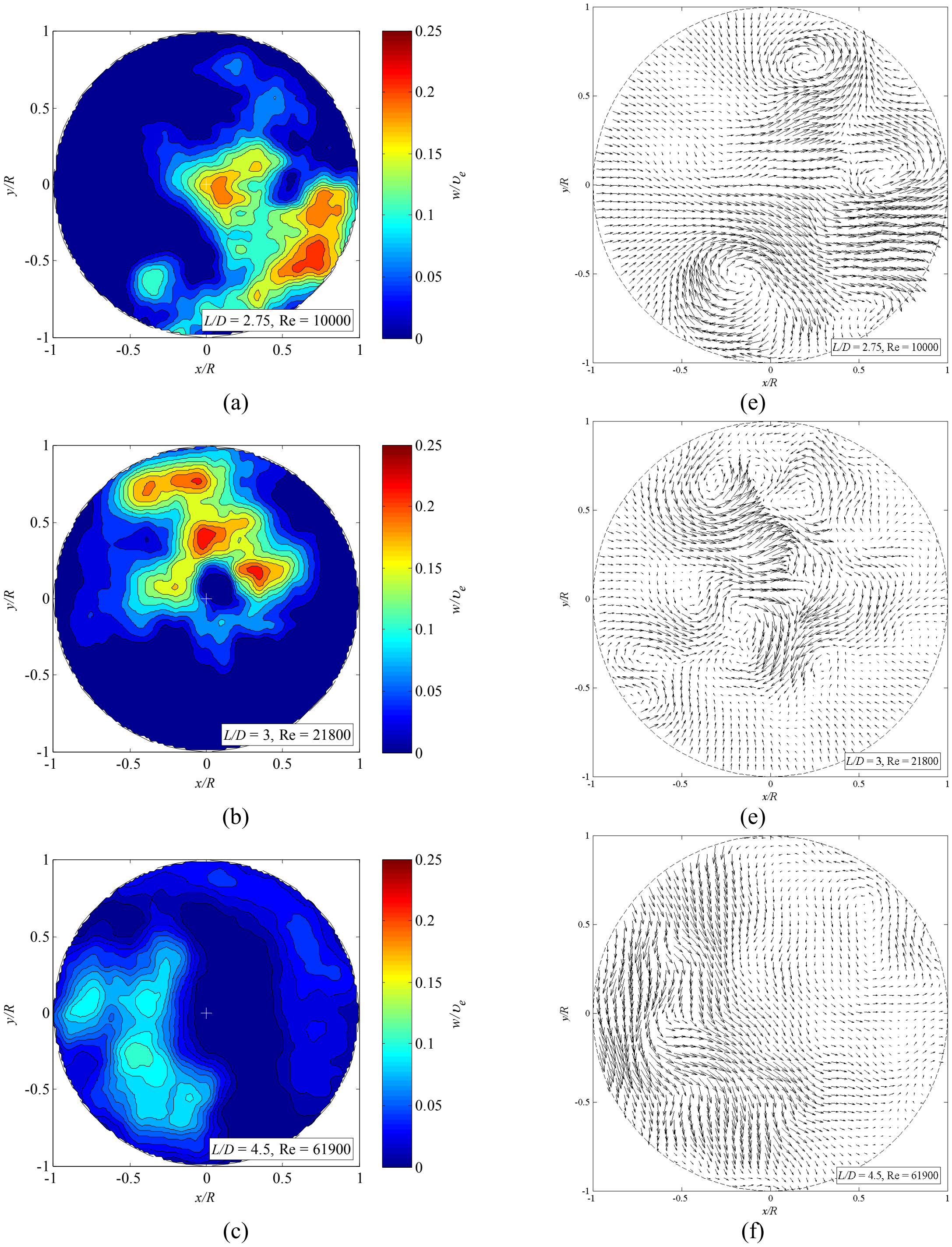

Figure 4.7 Contour plots of axial velocity distribution (a-c) and vector plots of in-plane velocity (d-f) illustrating the outflowing region of the jet in transitioning mode.

4.5 Mode-Finding Method

In order to determine precession probability, as well as conditionally average only those instantaneous vector fields which were in precessing mode, a technique was developed to determine the flow mode based on instantaneous axial velocity distribution. It is relatively easy to visually distinguish the two modes based on the axial velocity distribution, since the outflowing region is either kidney-bean shaped and along the chamber wall, or reasonably axisymmetric and in-line with the chamber axis. However, due to the large volume of data collected in this study (42,000 instantaneous vector fields for all chamber lengths and Reynolds numbers), a manual mode determination method relying on visual inspection of instantaneous velocity fields is not feasible.

The mode determination method characterizes the flow based on the instantaneous, positive axial velocity field. Due to the chaotic nature of the flow, and the possibility of the jet existing in a mode which is neither obviously axial nor precessing, as evident in Figure 4.7, three quantitative criteria are examined in the flow field, each deeming the flow as either precessing or axial. A best-two-of-three approach is used with these results. In this manner, if two mode-finding methods find the jet to be in precessing mode while the third disagrees, it is considered to be in precessing mode.

The probability of precession is defined as the ratio of the number of vector fields found to be in precessing mode (using the mode-finding method described in this section) to the total number of vector fields in a dataset at a given Reynolds number and chamber length. This is defined in equation (4.13).

$$P_{PJ} \equiv \frac{N_{PJ}}{N} \tag{4.13}$$

4.5.1 Peak Outflow Position Method

The first mode-finding method considers the position of the peak axial velocity of the issuing jet. The position of these velocity peaks differ between modes, as the issuing jet in axial mode resembles an axisymmetric jet, with its highest velocity region being near to the chamber center, while precessing mode has its velocity peak nearer to the chamber wall. Since the flow is highly turbulent, the axial velocity field is first heavily smoothed (25×25 linear filter) to highlight the dominant velocity distribution within it. Figure 4.8 shows a sample instantaneous positive axial velocity field before and after smoothing, as well as the position of the maximum velocity, (x_p, y_p). If this point is beyond a characteristic radius R_c, the jet is assumed to be in precessing mode. If (x_p, y_p) is within the circle of radius R_c, it is assumed to be in axial mode.

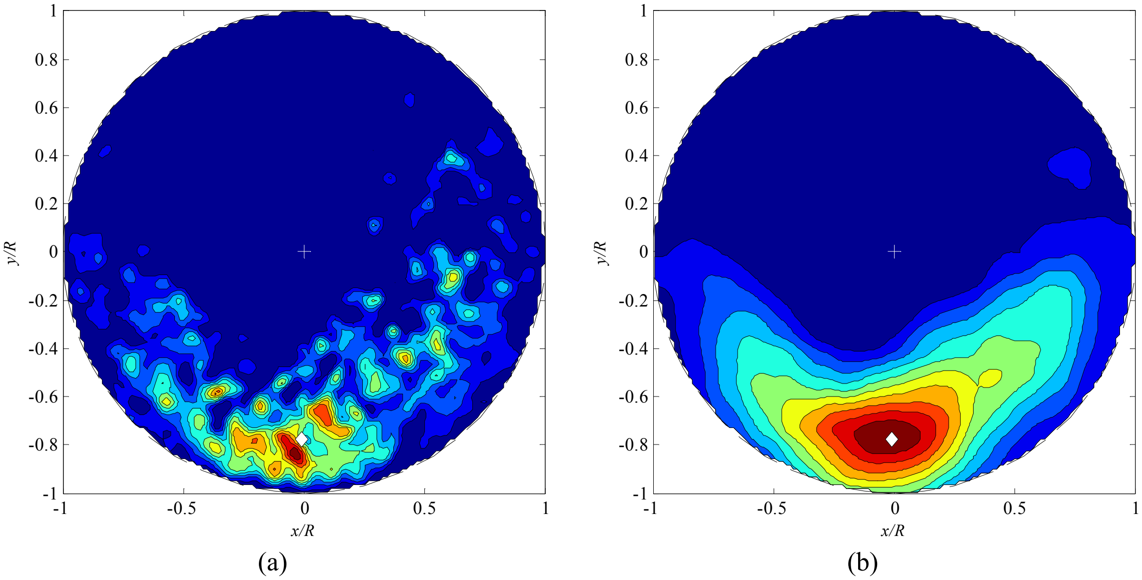

(a) (b)

Figure 4.8 Location of maximum outflow velocity shown in (a) unsmoothed and (b) smoothed axial vector field.

4.5.2 Areas Method

In its two characteristic modes, the shape of the issuing jet (the region of positive axial velocity) can be relatively circular (in axial mode) and coaxial with the chamber axis, or kidney-bean shaped (precessing mode), where the majority of outflow is nearer to the chamber wall than its center. With this in mind, it is assumed that in axial mode, there is a higher volume flow rate out of the chamber in a circular region within a radius R_c than beyond it. Conversely, for precessing mode, the opposite should hold true: There should be more volume flux in the annulus bounded by R_c and the chamber radius.

For each masked instantaneous axial-component flow field, the volume flow rates q_1 and q_2 are approximated using equations (4.14) and (4.15). These are the sums of volume flux through finite rectangular areas of dimensions δx and δy at all data points either within R_c or in the annulus beyond it, respectively. Positional coordinate arrays $\mathbf{X}$ and $\mathbf{Y}$ are adjusted for the position of chamber center, (x_c, y_c). If $q_1 > q_2$, the jet is considered to be in axial mode, and if $q_1 < q_2$, it is considered to be in precessing mode.

$$q_1 \approx \sum_{i,j} \breve{\mathbf{w}}_{i,j} \delta x \delta y, \quad 0 < \sqrt{\left(\mathbf{X}_{i,j} - x_c\right)^2 + \left(\mathbf{Y}_{i,j} - y_c\right)^2} \le R_c \tag{4.14}$$

$$q_2 \approx \sum_{i,j} \breve{\mathbf{w}}_{i,j} \delta x \delta y, \quad R_c < \sqrt{\left(\mathbf{X}_{i,j} - x_c\right)^2 + \left(\mathbf{Y}_{i,j} - y_c\right)^2} \le R \tag{4.15}$$

4.5.3 Centroid Method

The second method characterizes the flow mode based on the position of the fluidic centroid of the issuing jet relative to a third cutoff radius. This centroid is similar to a mass or area centroid; however, it is weighted with the value of axial velocity instead of mass or area. Its two components (in cylindrical coordinates) are given in equations

(4.16) and (4.17). If the position of this centroid is beyond R_c, the jet is considered to be in precessing mode, and if it is within R_c, it is considered to be in axial mode.

$$\tilde{r} = \frac{\sum rw(r,\theta)}{\sum w(r,\theta)} \tag{4.16}$$

$$\tilde{\theta} = \frac{1}{\tilde{r}} \frac{\sum r\theta w(r,\theta)}{\sum w(r,\theta)} \tag{4.17}$$

It is unreasonable to calculate the centroid using a Cartesian coordinate system, due to the crescent shape of the jet (along the *x-y* plane) when in PJ mode. Instead, the vector field is mapped into a cylindrical coordinate system, and the radial distance of the centroid defines the mode. The mapping of coordinate systems resembles a radar, sweeping out a circular area starting at an initial angle of θ_0 with the *y*-axis, and completing a 2π-revolution about the center of the chamber. Figure 4.9 and Figure 4.10 illustrate this method for the jet in axial mode and precessing mode, respectively.

The location of the highest outflow velocity, (x_p, y_p), is first found in a heavily smoothed (25×25) axial velocity field. The angle ϕ is formed between vector $\vec{s}$, defined in equation (4.18), which joins the origin and (x_p, y_p), and the y^+-axis. Angle θ_0 is defined as the angle opposite to ϕ, formed between the y^+-axis and $(-x_p, -y_p)$. This serves as the angle at which the sweep begins and ends. By mapping the coordinate system with this initial offset, it is guarantees that, if in precessing mode, the entire outflowing region occurs within the range $\theta_0 \le \theta < \theta_0 + 2\pi$.

$$\vec{s} \equiv \begin{bmatrix} x_p - x_c \\ y_p - y_c \end{bmatrix} \tag{4.18}$$

Since the vector fields exist in arrays as discrete data points, it is necessary to create new positional coordinate grids, **R** and **Θ**, containing all $0 < r \leq R$ and $\theta_0 \leq \theta < 2\pi + \theta_0$ positional coordinates. The size of these arrays has been chosen to be the same as **X** and **Y**, which results in a grid spacing of $\delta r = R/I$ and $\delta\theta = 2\pi/J$. **R** and **Θ** are filled according to equations (4.19) and (4.20), respectively, where *s* and *t* are their array indices in two dimensions.

$$\mathbf{R}_{s,t} = s\delta r; \quad 1 \leq s \leq I, \quad 1 \leq t \leq J \tag{4.19}$$

$$\mathbf{\Theta}_{s,t} = \theta_0 + (t-1)\delta\theta; \quad 1 \leq s \leq I, \quad 1 \leq t \leq J \tag{4.20}$$

Mapping from the masked axial velocity array in the Cartesian coordinate system, $\breve{\mathbf{w}}$, to the new array in cylindrical coordinates, $\mathbf{w_{cyl}}$, is achieved using equation (4.21). For every grid point in array $\mathbf{w_{cyl}}$ with position $(r,\theta) = (\mathbf{R}_{s,t}, \mathbf{\Theta}_{s,t})$, the corresponding point in Cartesian coordinates $(x,y) = (\mathbf{X}_{i,j}, \mathbf{Y}_{i,j})$ is found using equations (4.22) and (4.23). Since the data are not continuous, any point (x,y) which does not fall on a grid point has its axial velocity value cubically interpolated from the surrounding grid points.

$$\mathbf{w_{cyl}}_{s,t} = \breve{\mathbf{w}}_{i,j} \ni \begin{bmatrix} \mathbf{X}_{i,j} \\ \mathbf{Y}_{i,j} \end{bmatrix} = \begin{bmatrix} x_c \\ y_c \end{bmatrix} + \mathbf{R}_{s,t} \begin{bmatrix} \sin(\mathbf{\Theta}_{s,t}) \\ \cos(\mathbf{\Theta}_{s,t}) \end{bmatrix}, \quad \forall s,t \tag{4.21}$$

$$x = x_c + r\sin\theta \tag{4.22}$$

$$y = y_c + r\cos\theta \tag{4.23}$$

The radial component of the centroid is then calculated using equation (4.24). If $\tilde{r} > R_c$, the jet is considered to be in precessing mode. Otherwise, the jet is considered to be in axial mode. Note that all values of $\mathbf{w_{cyl}}$ beyond the chamber radius have a null value.

$$\widetilde{r} = \frac{\sum_{s=1}^{I}\sum_{t=1}^{J} \mathbf{R}_{s,t}\,\mathbf{w}_{\mathbf{cyl}_{s,t}}}{\sum_{s=1}^{I}\sum_{t=1}^{J} \mathbf{w}_{\mathbf{cyl}_{s,t}}} \tag{4.24}$$

Figure 4.9 and Figure 4.10 on the following pages illustrate this mode finding process for a sample vector field in both axial and precessing modes, respectively. Subfigure (a) shows the axial velocity contours after heavy smoothing. The position of the highest outflow velocity is marked with '★' while '✫' shows the point opposite to it. The white broken line forms angle θ_0 with the y^+-axis, and is the angular position from which the data is "swept-out". Subfigure (b) shows the position of the determined centroid, marked with '◊', while subfigure (c) shows the vector field in cylindrical coordinates. When calculating the centroid from (c), r and θ coordinates are treated as though they were Cartesian.

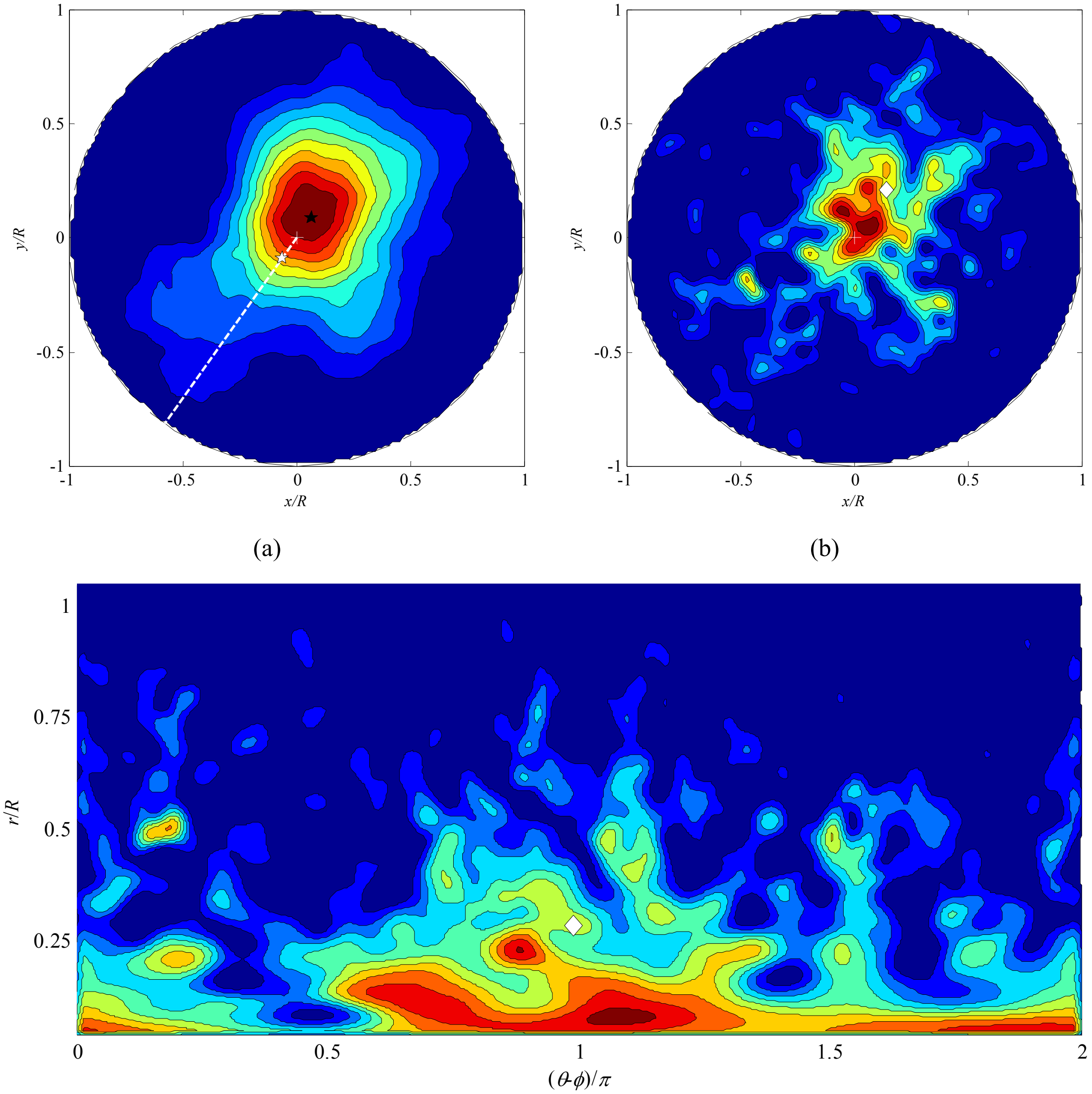

(a) (b)

(c)

Figure 4.9 Application of the centroid method to a instantaneous vector field in axial mode: (a) heavily smoothed axial velocity field showing the position of maximum outflow and the location opposite to it from which the sweep begins, marked with '★' and '✩', respectively; (b) unsmoothed axial velocity field showing the location of the centroid, marked with '◊'; (c) unsmoothed axial velocity field mapped into cylindrical coordinates showing the position of the centroid.

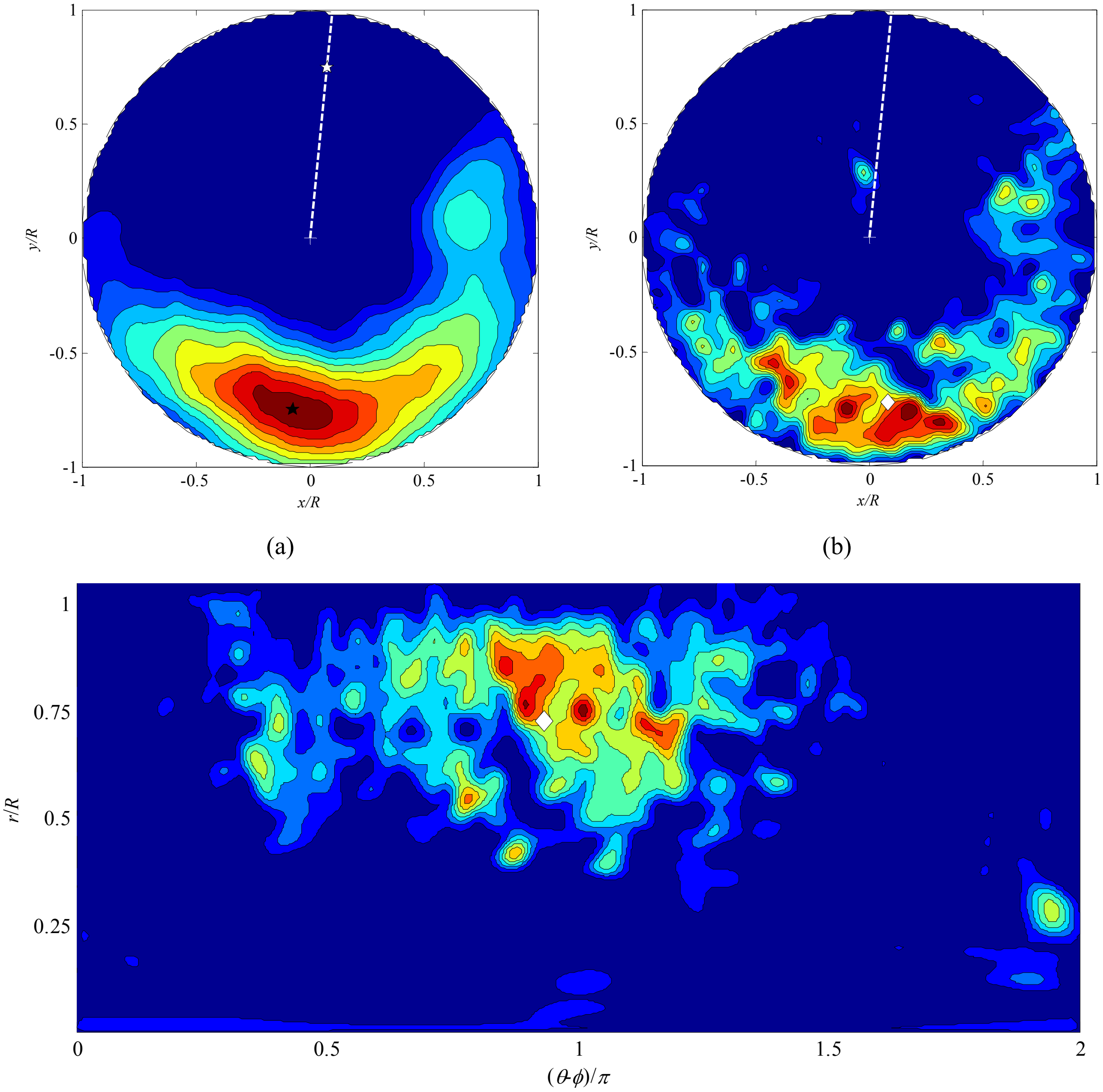

(a) (b)

(c)

Figure 4.10 Application of the centroid method to a instantaneous vector field in precessing mode: (a) heavily smoothed axial velocity field showing the position of maximum outflow and the location opposite to it from which the sweep begins, marked with '★' and '✫', respectively; (b) unsmoothed axial velocity field showing the location of the centroid, marked with '◊'; (c) unsmoothed axial velocity field mapped into cylindrical coordinates showing the position of the centroid.

4.5.4 Calculation of Cutoff Radius

It was necessary to determine the cutoff radii for the three methods outlined in the previous sections in order to accurately determine the mode for each vector field. Of the 18 chamber length and Reynolds number combinations studied, six were arbitrarily chosen. For each of these, the mode probability of the first one-hundred vector fields was determined by visual inspection, based on the mode characterization outlined in section (4.4). The precession probability values found are reported in Table 4-2. The same one hundred images from each set were analyzed using the three mode-finding methods at different cutoff radii over the range $0 \leq R_c \leq R$, which resulted in a different precession probability for each method at each cutoff radius. The relationship between R_c and the mode probability determined by the three methods is shown in Figure 4.11.

For each of the six chamber length-Reynolds number combinations and for each of the mode-finding methods, the cutoff-radius value was found which resulted in the same precession probability as manually determined for that set. For example, for a chamber length of *L/D* = 2.75 at a Reynolds number of 61,900, the precession mode probability determined from visual inspection of the axial velocity fields was found to be 84%. In Figure 4.11(d), it can be observed that the centroid method (section 4.5.3) requires a cutoff radius of 0.60*R* in order to produce a precession probability of 84%, while the area method (section 4.5.2) requires a cutoff radius of 0.71*R*. All cutoff radii for the three methods are in Table 4-2.

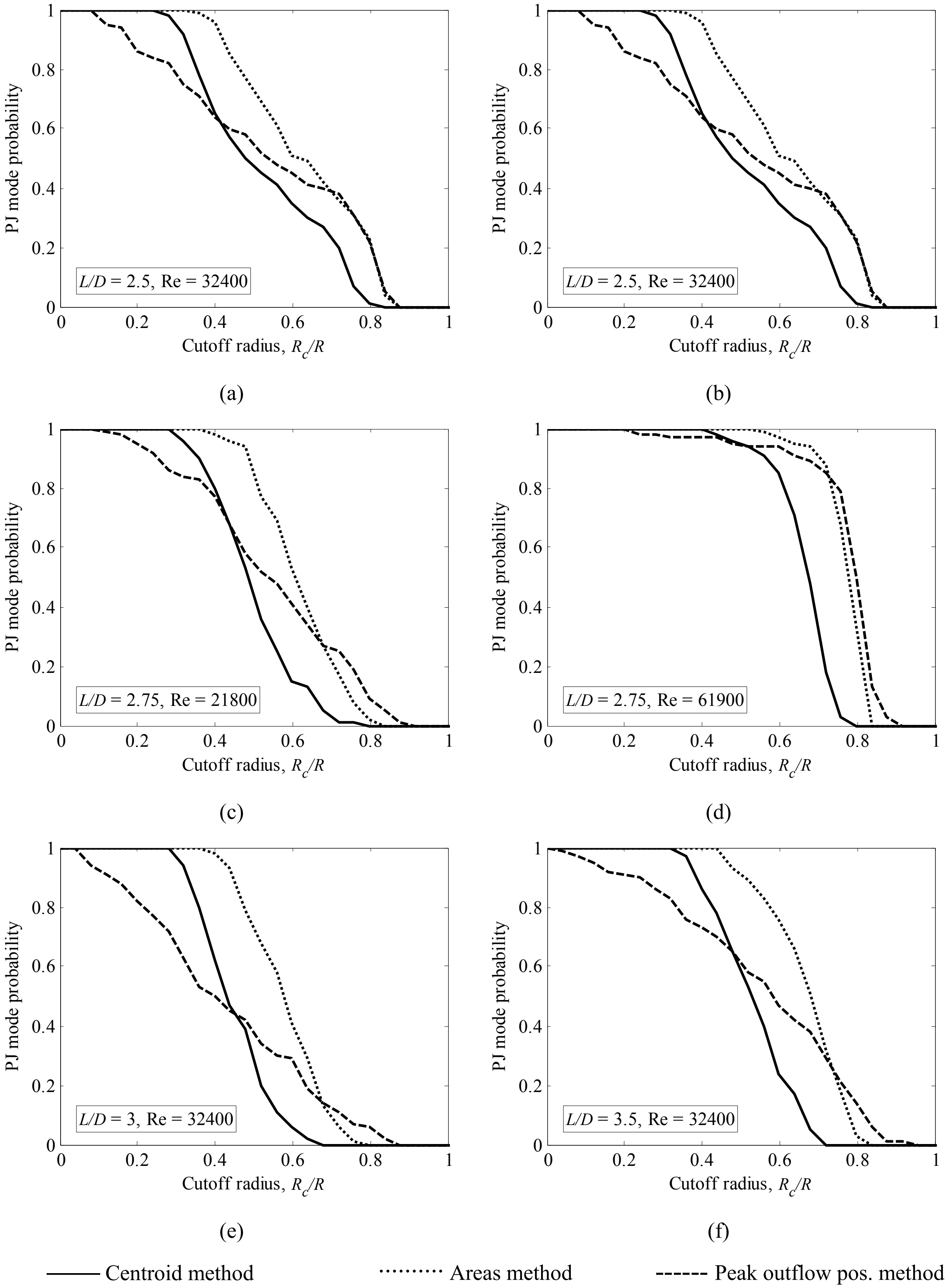

(a) (b) (c) (d) (e) (f)

Figure 4.11 Cutoff radius finding results for the following chamber length and Reynolds number combinations: (a) *L/D* = 2.0, Re = 32,400; (b) *L/D* = 2.5, Re = 32,400; (c) *L/D* = 2.75, Re = 61,900; (d) *L/D* = 2.75, Re = 21,800; (e) *L/D* = 3.0, Re = 32,400; (f) *L/D* = 3.5, Re = 21,800.

Table 4-2 Cutoff radii determined using the three mode finding methods

Reynolds number, Re		10,000	66,100	32,400	32,400	32,400	32,400	$\overline{R}_c$	$\sigma_{\overline{R}_c}$
Chamber length, *L/D*		2.75	2.75	2	2.5	3	3.5		
PJ mode probability, P_{PJ}		17%	84%	61%	37%	4%	24%		
Cutoff Radius, R_c/R	*Centroid Method*	0.59	0.60	0.61	0.59	0.61	0.60	0.60	0.01
	Areas Method	0.72	0.73	0.72	0.71	0.73	0.73	0.72	0.01
	Peak Outflow Position Method	0.77	0.77	0.67	0.73	0.82	0.73	0.74	0.04

For a given mode-finding method, the proper cutoff radius is assumed to be the average of the cutoff radii found for the different chamber length and Reynolds number combinations for that method. It is apparent from Table 4-2 that the cutoff radius for a given mode is not greatly dependant on neither Reynolds number nor chamber length. This is especially true for the areas and centroid methods, which have a standard deviation of only $0.01R$ between the six Reynolds number and chamber length combinations. Of the three methods, the peak outflow position method (Section 4.5.1) is the most volatile, with a standard deviation of $0.04R$. Since a best-two-of-three approach is used in the mode-finding algorithm, however, the larger spread of cutoff radii with the outflow position method should not greatly affect the determined mode of an instantaneous vector field.

4.6 Entrainment and Conditional Averaging of Axial Velocity

4.6.1 Entrainment Ratio

The amount of fluid being drawn back into the precession chamber through the exit plane of the chamber (at an axial distance $z = 0$) is compared between the two flow modes for each chamber length and Reynolds number. The amount of fluid being entrained back into the chamber is characterized with the entrainment ratio, *E*, which is defined in equation (4.25) as the ratio of mass flux into the chamber to the mass flux out of the chamber at the chamber exit plane.

$$E \equiv \left. \frac{\dot{m}_{in}}{\dot{m}_{out}} \right|_{z=0} \tag{4.25}$$

The mass fluxes in and out of the chamber are approximated as the sum of mass flux through finite rectangular regions centered at each grid point within array $\breve{\mathbf{w}}$ of size δx and δy. Mass flux into the chamber, $\dot{m}_{in}$, sums all the mass flux through all of these regions where the local axial component is negative (into the chamber), while the mass flux out of the chamber, $\dot{m}_{out}$, includes all data points where axial velocity is positive (out of the chamber). The approximations for these two values are given in equations (4.26) and (4.27), respectively, where ρ is the fluid density.

$$\dot{m}_{in} \approx \rho \sum_{i=1}^{I} \sum_{j=1}^{J} \left| \breve{\mathbf{w}}_{i,j} \right| \delta x \delta y, \quad \breve{\mathbf{w}}_{i,j} < 0 \tag{4.26}$$

$$\dot{m}_{out} \approx \rho \sum_{i=1}^{I} \sum_{j=1}^{J} \breve{\mathbf{w}}_{i,j} \delta x \delta y, \quad \breve{\mathbf{w}}_{i,j} > 0 \tag{4.27}$$

At each chamber length and Reynolds number there are $N = 1{,}000$ vector fields. Starting from the first, each has its entrainment ratio, *E*, calculated from equation (4.25). Based on its mode (determined using the method outlined in Section 4.5), the value of *E* is appended to one of two arrays, $\mathbf{E_{PJ}}$ or $\mathbf{E_{AJ}}$, defined in equations (4.28) and (4.29), which contain all entrainment ratio values for the jet in precessing mode and axial mode, respectively. N_{PJ} and N_{AJ} are the number of vector fields in precessing and axial modes, respectively.

$$\mathbf{E_{PJ}} = \left[\left(\frac{\dot{m}_{in}}{\dot{m}_{out}} \right)_1 \quad \left(\frac{\dot{m}_{in}}{\dot{m}_{out}} \right)_2 \quad \cdots \quad \left(\frac{\dot{m}_{in}}{\dot{m}_{out}} \right)_{N_{PJ}} \right] \tag{4.28}$$

$$\mathbf{E_{AJ}} = \left[\left(\frac{\dot{m}_{in}}{\dot{m}_{out}} \right)_1 \quad \left(\frac{\dot{m}_{in}}{\dot{m}_{out}} \right)_2 \quad \cdots \quad \left(\frac{\dot{m}_{in}}{\dot{m}_{out}} \right)_{N_{AJ}} \right] \tag{4.29}$$

The entrainment ratio for each chamber length and Reynolds number for both modes is finally determined by averaging all mass flux fractions, as per equations (4.30) and (4.31).

$$E_{PJ} = \frac{1}{N_{PJ}} \sum_{n=1}^{N_{PJ}} \mathbf{E_{PJ}}_n \tag{4.30}$$

$$E_{AJ} = \frac{1}{N_{AJ}} \sum_{n=1}^{N_{AJ}} \mathbf{E_{AJ}}_n \tag{4.31}$$

4.6.2 Axial Velocity Field Rotation and Averaging

Due to the rotational nature of the issuing jet, its position varies throughout the chamber exit plane with time and in successive images. In order to attempt to perform any averaging or statistical work on the velocity fields of the jet in precessing mode, it is necessary to include only those vector fields which are in precessing mode and transform them in such a way that the same regions of the jet are averaged together, regardless of the orientation of the jet in the ROI. The fluidic centroid of the jet (described in Section 4.5.3) is chosen as the common point, and instantaneous vector fields which are in precessing mode are rotated so that the centroid always lies on the y^+-axis. Average and RMS axial velocity distributions are then calculated. The procedure is explained in the following paragraphs.

The mode of each vector field is first determined using the method in Section 4.5. If in precessing mode, the axial velocity field is mapped to cylindrical coordinates using the method outlined in Section 4.5.3 and the position of the centroid is found. The azimuthal component of the position of the centroid is found with equation (4.32).

$$\tilde{\theta} = \frac{1}{\tilde{r}} \frac{\sum_{s=1}^{I}\sum_{t=1}^{J} \mathbf{R}_{s,t} \mathbf{\Theta}_{s,t} \mathbf{w_{cyl}}_{s,t}}{\sum_{s=1}^{I}\sum_{t=1}^{J} \mathbf{w_{cyl}}_{s,t}} \tag{4.32}$$

The method for rotation is based on the change of basis from an old basis $B = (\hat{x}, \hat{y})$ to a new basis $B' = (\hat{x}', \hat{y}')$. Here, the new basis is rotated an angle θ from the old one (Anton & Rorres, 2000), and $\hat{x}$ and $\hat{y}$ are unit vectors in the x and y directions, respectively. This yields the transformation matrix **P** between the rotated and original coordinate system, $B' \mapsto B$, which is defined in equation (4.33).

$$\mathbf{P} \equiv \begin{bmatrix} \cos\theta & -\sin\theta \\ \sin\theta & \cos\theta \end{bmatrix} \tag{4.33}$$

The transformation matrix P maps rotated positional coordinates (x', y') to their corresponding position in the original coordinate system (x, y), as illustrated in equation (4.34). This yields equations (4.35) and (4.36), which relate x and y positional coordinates, respectively, to positional coordinates x' and y'.

$$\begin{bmatrix} x \\ y \end{bmatrix} = \mathbf{P}^{-1} \begin{bmatrix} x' \\ y' \end{bmatrix} = \begin{bmatrix} \cos\theta & \sin\theta \\ -\sin\theta & \cos\theta \end{bmatrix} \begin{bmatrix} x' \\ y' \end{bmatrix} \tag{4.34}$$

$$x = x' \cos\theta + y' \sin\theta \tag{4.35}$$

$$y = -x' \sin\theta + y' \cos\theta \tag{4.36}$$

Rotation is achieved by mapping each vector field so that the position of the centroid in the rotated axial velocity array, $\mathbf{w_{rot}}$, lies on the y^+-axis. This array has the same size as its original counterpart, $\breve{\mathbf{w}}$. The necessary angle for rotation is $\theta = \tilde{\theta}$, which is the azimuthal location of the fluidic centroid of the jet. If the data were continuous, the relationship between original and rotated vector fields, $\breve{w}$ and w_{rot}, would hold the form of equation (4.37).

$$w_{rot}(x, y) = \breve{w}\left(x'\cos\tilde{\theta} + y'\sin\tilde{\theta}, -x'\sin\tilde{\theta} + y'\cos\tilde{\theta}\right) \tag{4.37}$$

Since, however, the data exist in discretized arrays, it is necessary to map the value of each data point in $\mathbf{w_{rot}}$ from its corresponding position in $\breve{\mathbf{w}}$. This is achieved with equation (4.38), which assigns every position $(x', y') = \left(\mathbf{X}_{i',j'}, \mathbf{Y}_{i',j'}\right)$ in the rotated velocity array the corresponding value of velocity from the original array at position $(x, y) = \left(\mathbf{X}_{i,j}, \mathbf{Y}_{i,j}\right)$. Any velocity value in $\breve{\mathbf{w}}$ which does not lie on a grid point is cubically interpolated from the velocity values at the surrounding grid points. Figure 4.12 shows a sample axial velocity field before and after rotation. The axial velocity distribution in this plot is heavily smoothed (10×10 linear filter) and shows only regions of positive axial velocity in order to more clearly illustrate the rotation. Vector fields undergoing this process were unsmoothed and included both positive and negative axial velocity data.

$$\mathbf{w}_{\mathbf{rot}\,i',j'} = \breve{\mathbf{w}}_{i,j} \ni \begin{bmatrix} \mathbf{X}_{i,j} \\ \mathbf{Y}_{i,j} \end{bmatrix} = \begin{bmatrix} \cos\tilde{\theta} & \sin\tilde{\theta} \\ -\sin\tilde{\theta} & \cos\tilde{\theta} \end{bmatrix} \begin{bmatrix} \mathbf{X}_{i',j'} \\ \mathbf{Y}_{i',j'} \end{bmatrix}, \quad \forall i', j' \tag{4.38}$$

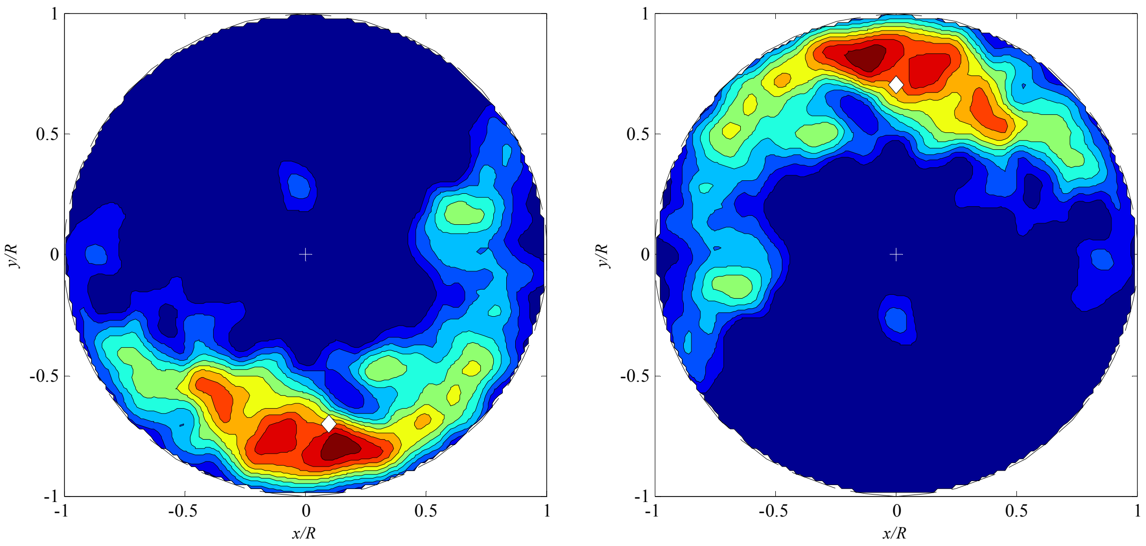

(a) (b)

Figure 4.12 Figure showing the contour plot of positive axial velocity (a) before and (b) after rotation. The data have been smoothed (10×10 linear filter) to highlight the large-scale velocity distribution of the issuing jet. The ◊ shows the position of the fluidic centroid.

Mapping from $(x',y') \mapsto (x,y)$ was chosen instead of the reverse, due to the discretized nature of the data. If discrete points from the original array were mapped to the rotated array, most of the points in the new array would not fall on discrete grid points. If this was the case, assigning values to grid points in the rotated array would require solving sets of equations for each point, since axial velocity values at grid points would have to be determined by reverse-interpolation from velocity values existing between them. By mapping from the rotated array to the original array, values at discrete grid points in the rotated array correspond to points which may or may not exactly lie on grid points in the original array. If they do not, their value is simply interpolated from surrounding points.

The phase-averaged axial velocity field, $\mathbf{W}$, is then calculated using equation (4.39), where $(\mathbf{w}_{\mathbf{rot}})_{\mathbf{n}}$ is the n^{th} of N_{PJ} rotated instantaneous vector fields in precessing mode. The RMS axial velocity field is determined with equation (4.40).

$$\mathbf{W} = \frac{1}{N_{PJ}} \sum_{n=1}^{N_{PJ}} (\mathbf{w}_{\mathbf{rot}})_{\mathbf{n}} \tag{4.39}$$

$$\mathbf{w}' = \frac{1}{N_{PJ}} \left\{ \sum_{n=1}^{N_{PJ}} \left[\mathbf{W} - (\mathbf{w}_{\mathbf{rot}})_{\mathbf{n}} \right]^2 \right\}^{\frac{1}{2}} \tag{4.40}$$

4.6.3 Jet Area Ratio

The effect of Reynolds number and chamber length on the expansion of the jet while in precessing mode can be determined from the conditionally averaged axial velocity fields. The dimensionless area ratio, γ_c, is defined in equation (4.41) as the ratio between the cross-sectional area of the jet, A_j, and the area of the chamber exit, $A_c = \pi R^2$, and characterizes the fraction of chamber area which is occupied by the jet.

$$\gamma_c \equiv \frac{A_j}{A_c} = \frac{A_j}{\pi R^2} \tag{4.41}$$

The jet is defined in any position in the light sheet plane where the axial velocity is positive. The jet's cross-sectional area may then be approximated using equation (4.42), which sums the areas of all finite rectangular regions of size $\delta x \times \delta y$ centered about grid points within the averaged axial velocity array $\mathbf{W}$ whose axial velocity is positive. In equation (4.42), $\mathbf{f}$ is a Boolean array identical in size to $\mathbf{W}$, where every grid point within it is valued at unity if the corresponding grid point in $\mathbf{W}$ has a positive axial velocity, and zero otherwise.

$$A_j \approx \sum_{i=1}^{I}\sum_{j=1}^{J}\mathbf{f}_{i,j}\delta x\delta y, \quad \begin{cases} \mathbf{f}_{i,j}=1, & \mathbf{W}_{i,j}>0 \\ \mathbf{f}_{i,j}=0, & \mathbf{W}_{i,j}\le 0 \end{cases} \tag{4.42}$$

4.7 Results

4.7.1 Chamber Length and Reynolds Number Effects on Precession Probability

The relationship between precession probability, P_{PJ}, and the chamber length at various Reynolds numbers is shown in Figure 4.13. The highest precession probability appears to occur at $L/D = 2$, and the range of high probability is larger at higher Reynolds numbers. There is a sharp decrease in probability at a chamber length of 3*D*. It is apparent in this figure that the probability trend is similar for all Reynolds numbers except for Re = 10,000, where the flow is considered to be laminar. There is no precession at a chamber length of $L/D = 1$.

The probability of precession appears to increase beyond $L/D = 3$ up to $L/D = 4.5$. At the latter chamber length, the jet is beyond the chamber length range given by Newbold (1997), and may not be ‘precessing’ in the sense desirable to industry, where there is significant backward entrainment, thereby improving mixing. However, the axial velocity field of the jet at this chamber length does exhibit characteristics of the precessing jet, such as the crescent shaped jet with high velocity near to the chamber wall. For this reason, the mode determination method outlined in Section 4.5 characterizes the jet as PJ.

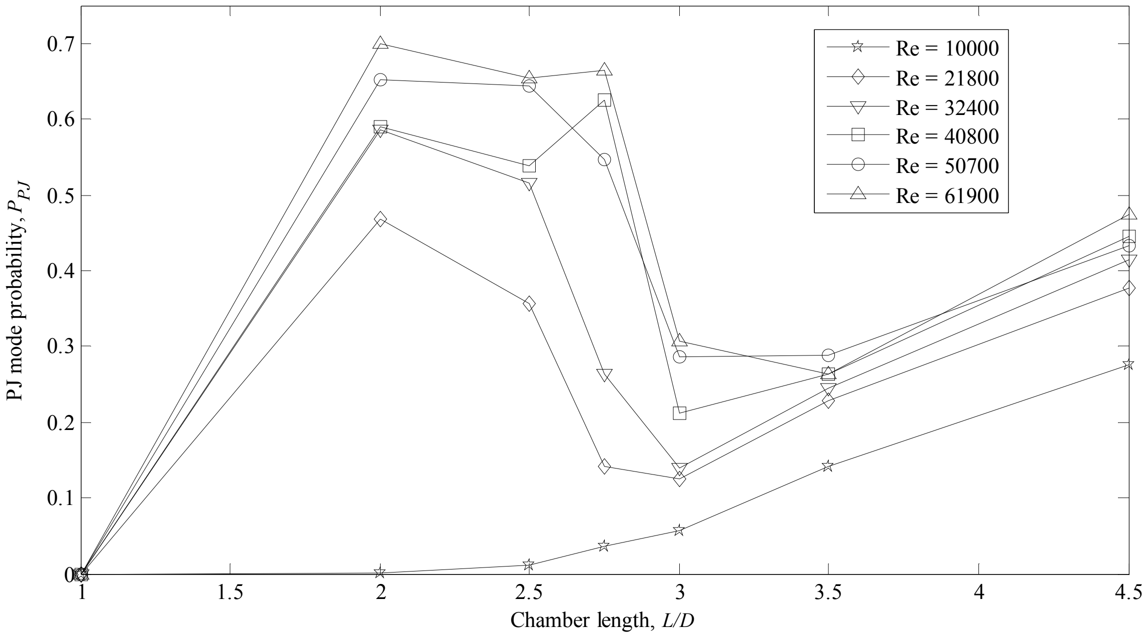

Figure 4.13 Effect of chamber length on the probability of precession at varying Reynolds numbers.

Figure 4.14 shows the relationship between precession probability and Reynolds number at different chamber lengths. There appear to be three distinct trends here: The first occurs for chamber lengths $L/D \geq 3$, at which precession probability almost linearly increases with Reynolds number, beginning with a non-zero P_{PJ} at $\mathrm{Re} = 10{,}000$. At a chamber length of $L/D = 2.75$, precession probability is near-zero at the lowest Reynolds number, and increases almost linearly with Reynolds number, excluding the precession probability value at Re = 40,800, which is assumed to be an outlier. In the range $2 \leq L/D \leq 2.5$, precession probability is zero at the lowest Reynolds number, and appears to increase following a second-order relationship with Reynolds number. There is no precession at a chamber length of $L/D = 1$.

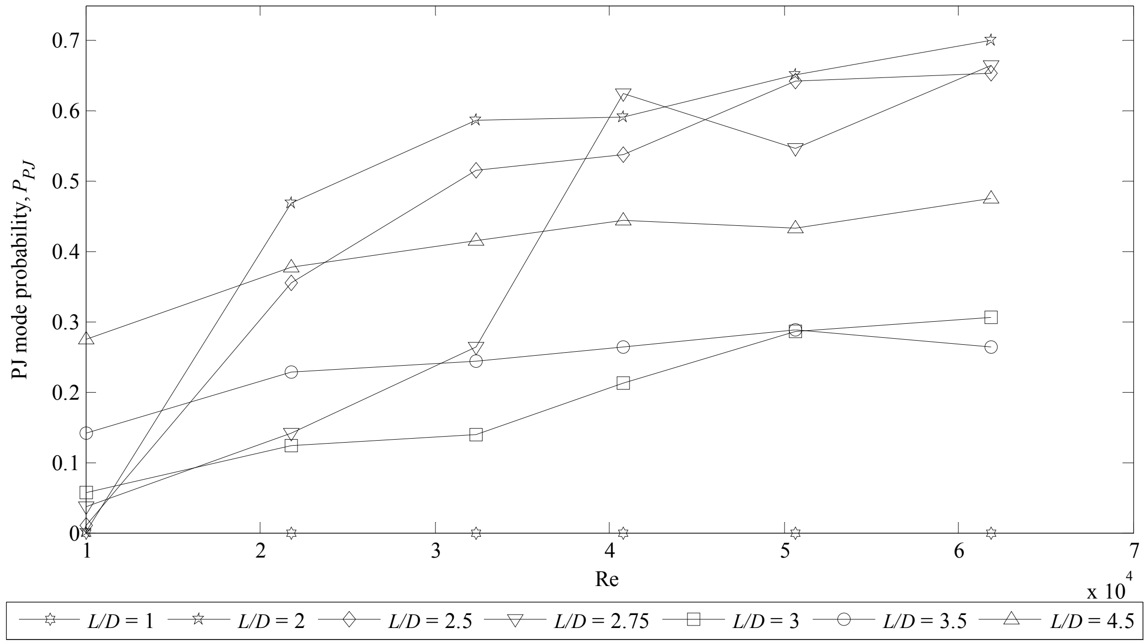

Figure 4.14 Effect of Reynolds number on the probability of precession at varying chamber lengths.

4.7.2 Chamber Length and Reynolds Number Effects on Entrainment Ratio

The relationship between entrainment ratio, *E*, defined in Section 4.6.1, and chamber length is shown in Figure 4.15 for both precessing an axial modes. Figure 4.16 shows the relationship between *E* and Reynolds number for these two modes. It is apparent from Figure 4.15 that there is a strong relationship between chamber length and the entrainment ratio. Entrainment ratio is highest at $L/D = 2$, and decreases with increasing chamber length for both modes. Figure 4.16 shows a weak relationship between Reynolds number and entrainment ratio, except at Re = 10,000, where the flow is considered to be laminar. There is also negligible difference in entrainment back into the chamber between the two modes.

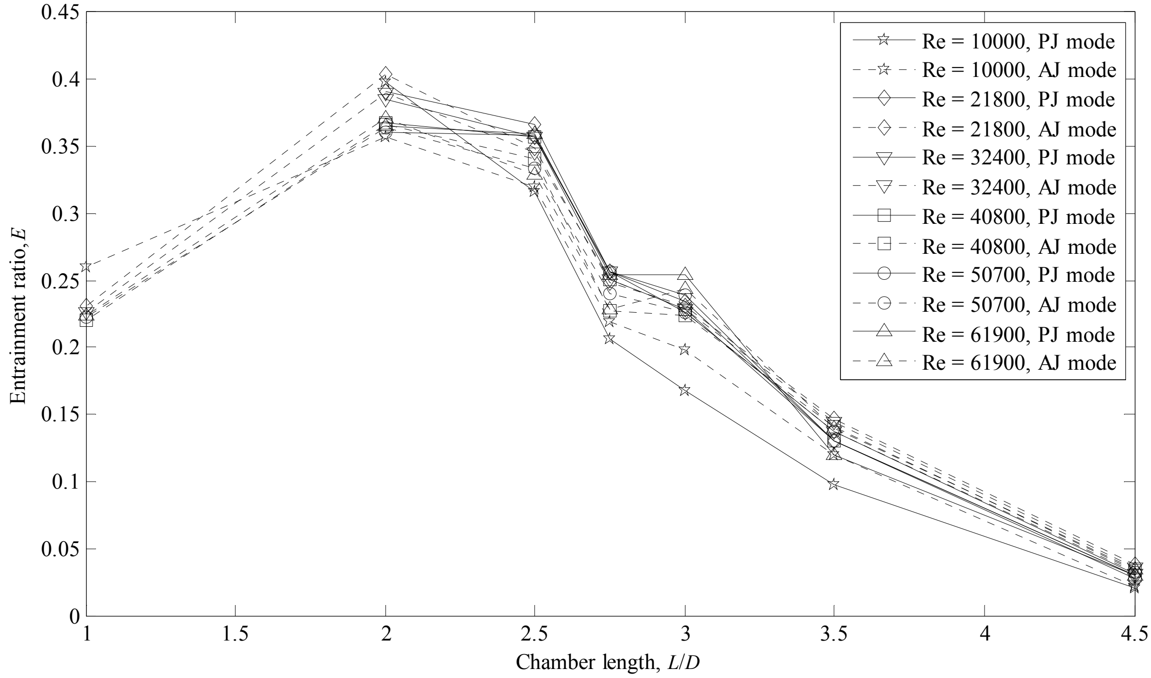

Figure 4.15 Effect of chamber length on the entrainment ratio at varying Reynolds numbers.

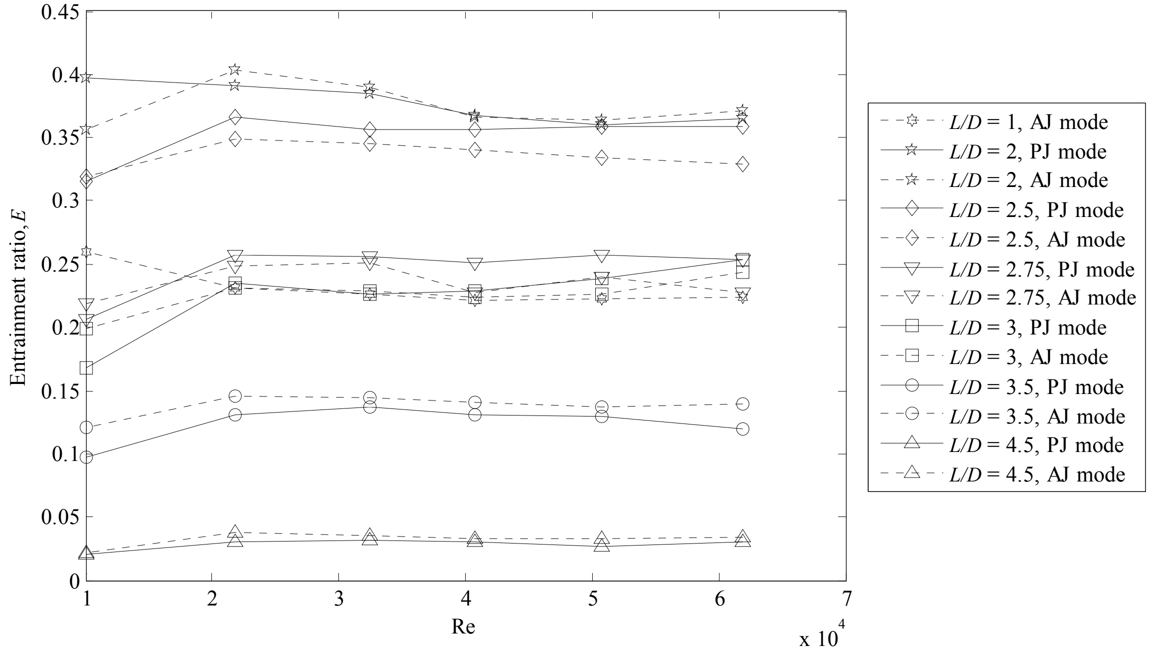

Figure 4.16 Effect of Reynolds number on the entrainment ratio at varying chamber lengths..

4.7.3 Conditionally Averaged Axial Velocity Profiles

Averaged and RMS velocity profiles for all chamber length and Reynolds number combinations (except for $L/D = 1$, since there was no precession at this chamber length) are shown in Figure 4.17 through Figure 4.22. These figures are the result of the conditional averaging technique described in Section 4.6.2. Note that for certain Reynolds number and chamber length combinations at which there was low precession probability, average and RMS axial velocity flow fields appear blotchy and not as smooth as the others. This is due to the low data density for calculating the average and RMS. For example at $L/D = 2.0$ and $\mathrm{Re} = 10{,}000$, only 1% of the observed instantaneous axial velocity fields were in precessing mode, resulting in an average and RMS field for this chamber length and Reynolds number combination being calculated from ten images. Those combinations with higher precession probability show much better average and RMS axial velocity fields.

All chamber lengths show a crescent-shaped region of positive axial velocity which hugs the chamber wall. The highest region of axial velocity is at a radial distance of approximately $r/R = 0.8$. The largest fluctuations in velocity occur in the high-velocity region of positive axial velocity, and decrease with increasing radial and azimuthal distance from this area. The smallest velocity fluctuations occur near to the chamber wall opposite to the outflow region, i.e. $(x, y) \approx (0, -R)$. The shape and size of the RMS velocity distribution does not appear to significantly change at different chamber lengths and Reynolds numbers, except at those at which there was a low precession probability, resulting in a low data density. Only the magnitude of w'/υ_e is affected by chamber length. At all chamber lengths except for $L/D = 4.5$, there is entrainment back into the cavity in the round region opposite (on the other side of the *x*-axis) to the region of outflow. This area decreases in size as Reynolds number increases, disappearing completely at chamber lengths above $3.5D$.

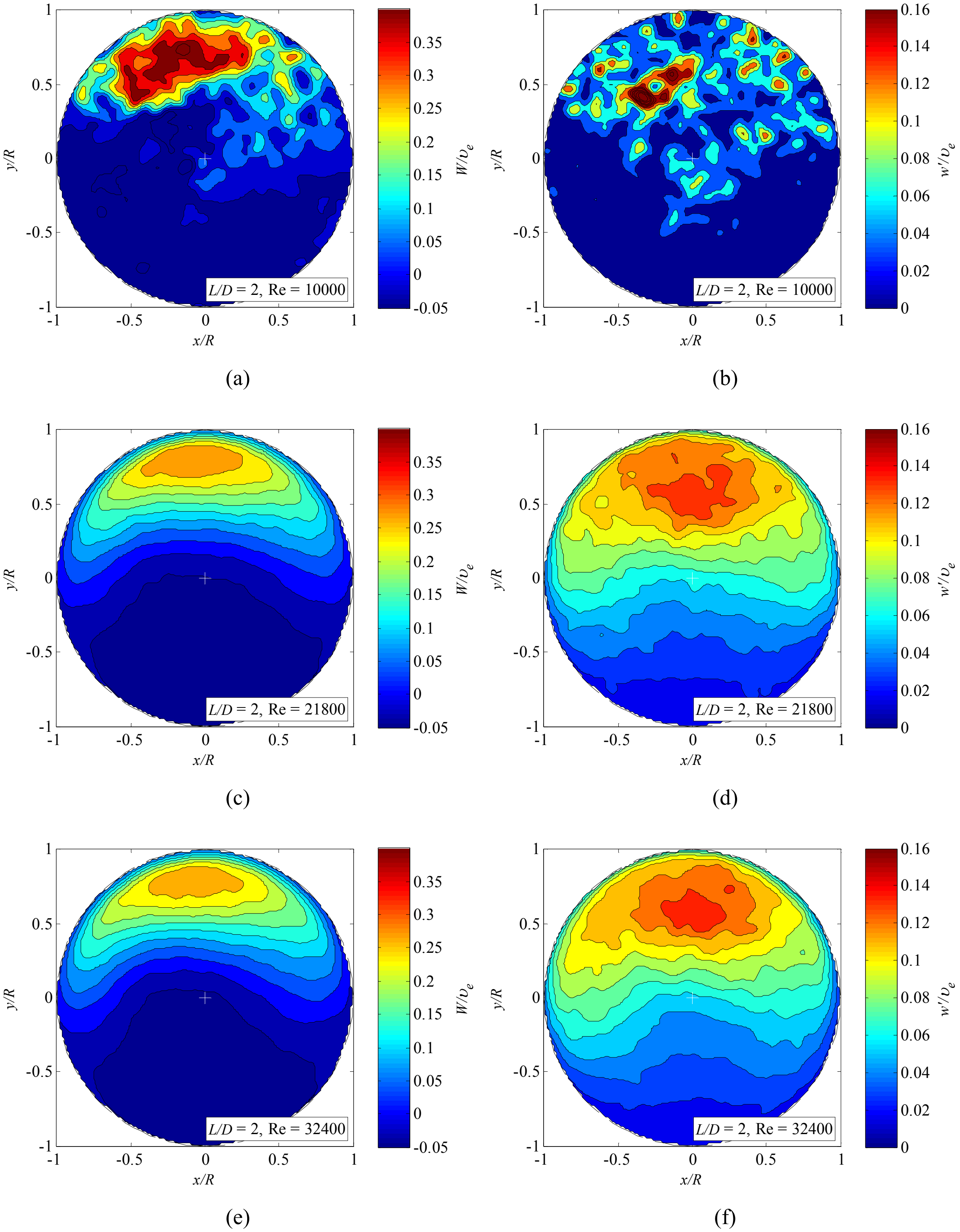

Figure 4.17 Average and RMS axial velocity contours for chamber length *L/D* = 2.

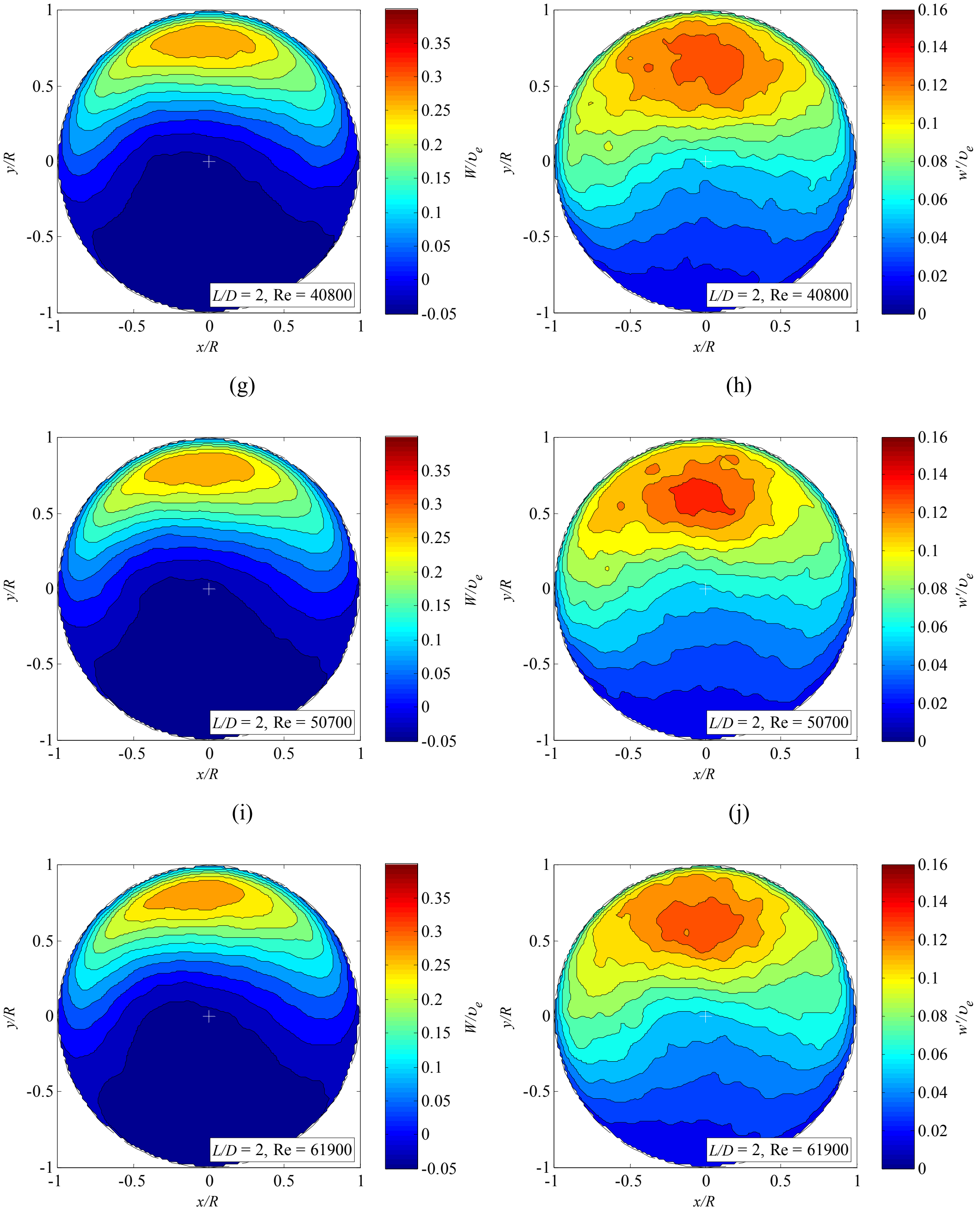

(g) (h)

(i) (j)

(k) (l)

Figure 4.17 Average and RMS axial velocity contours for chamber length *L/D* = 2.

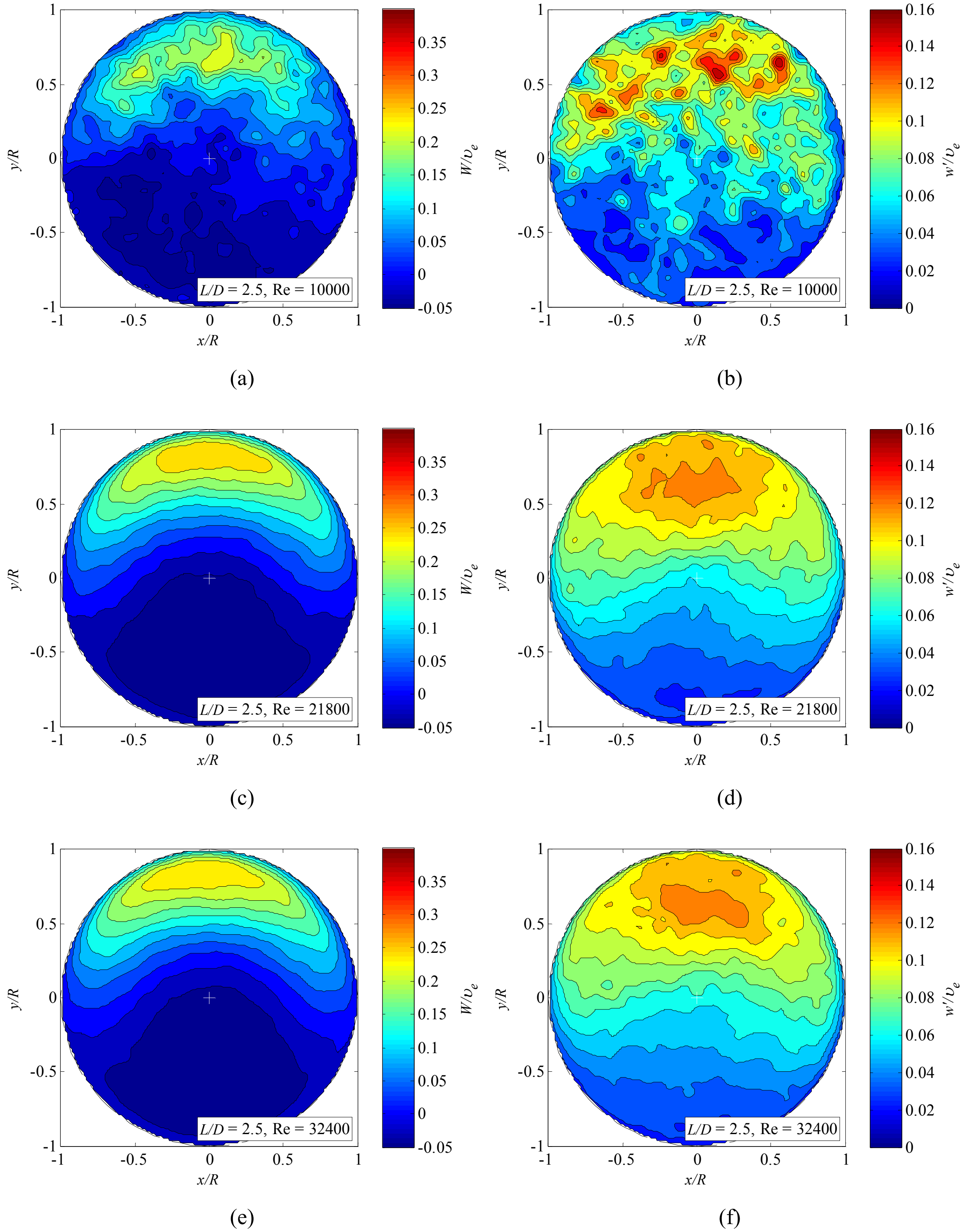

Figure 4.18 Average and RMS axial velocity contours for chamber length *L/D* = 2.5.

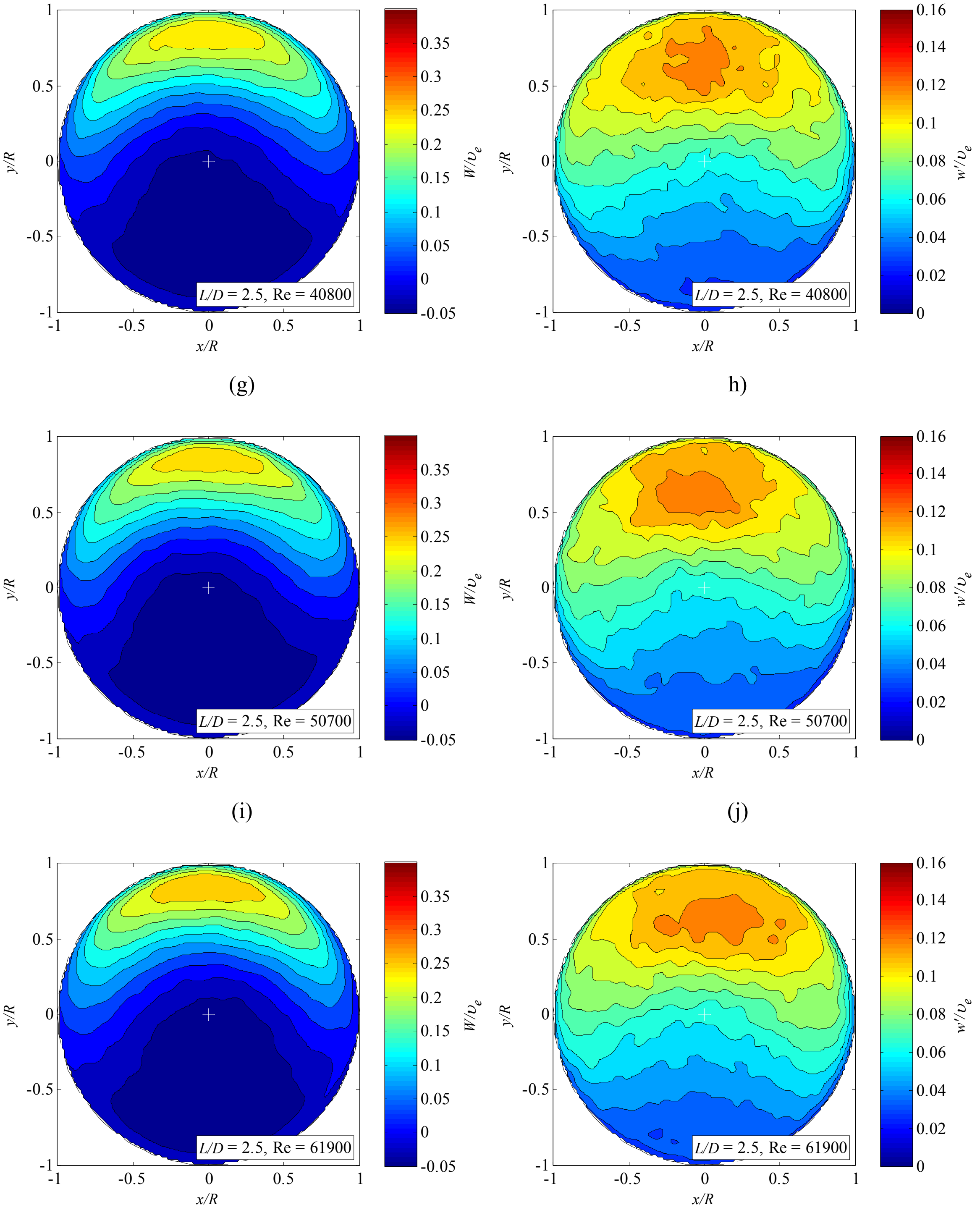

(g) h)

(i) (j)

(k) (l)

Figure 4.18 Average and RMS axial velocity contours for chamber length *L/D* = 2.5.

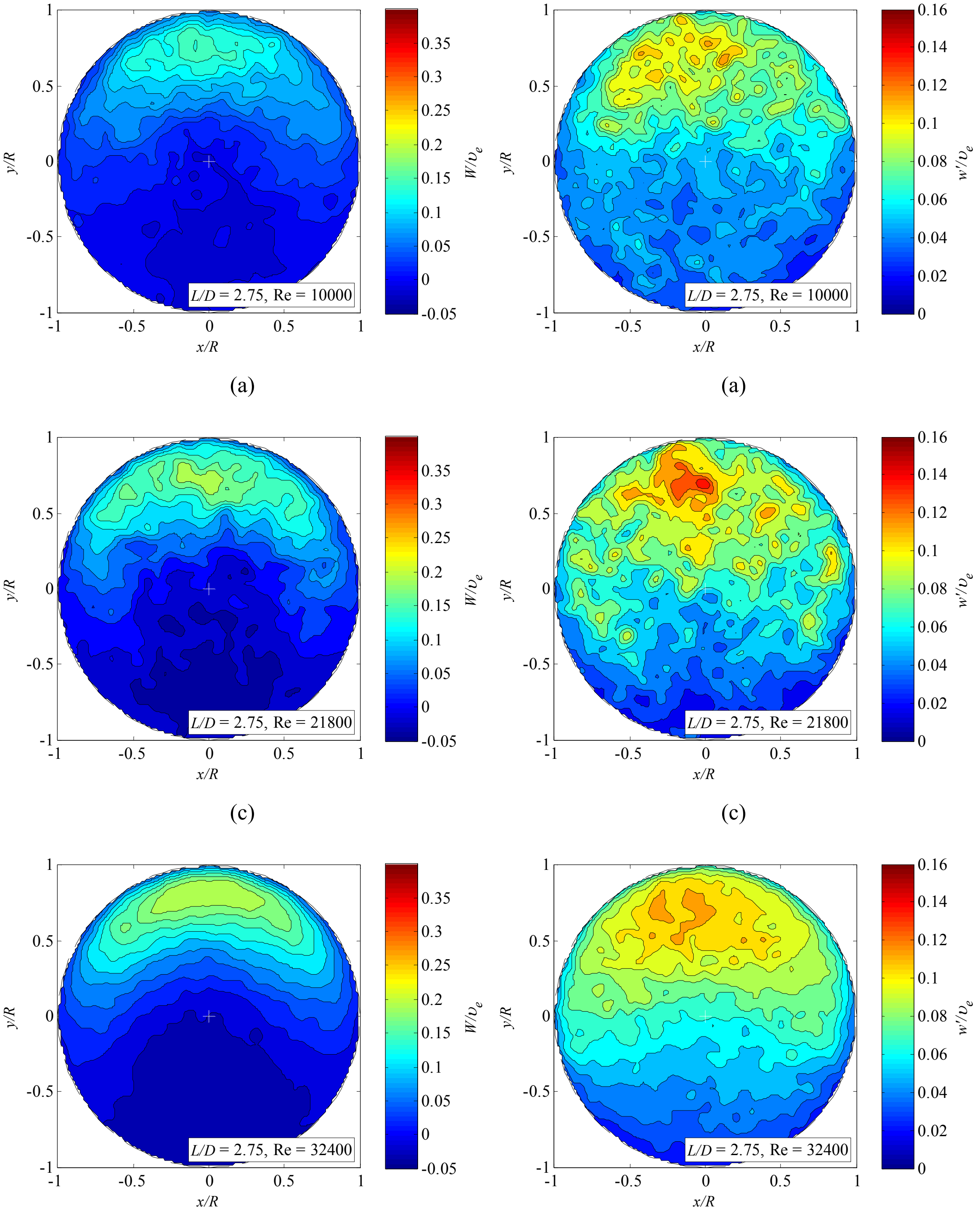

(a) (a)

(c) (c)

(e) (f)

Figure 4.19 Average and RMS axial velocity contours for chamber length *L/D* = 2.75.

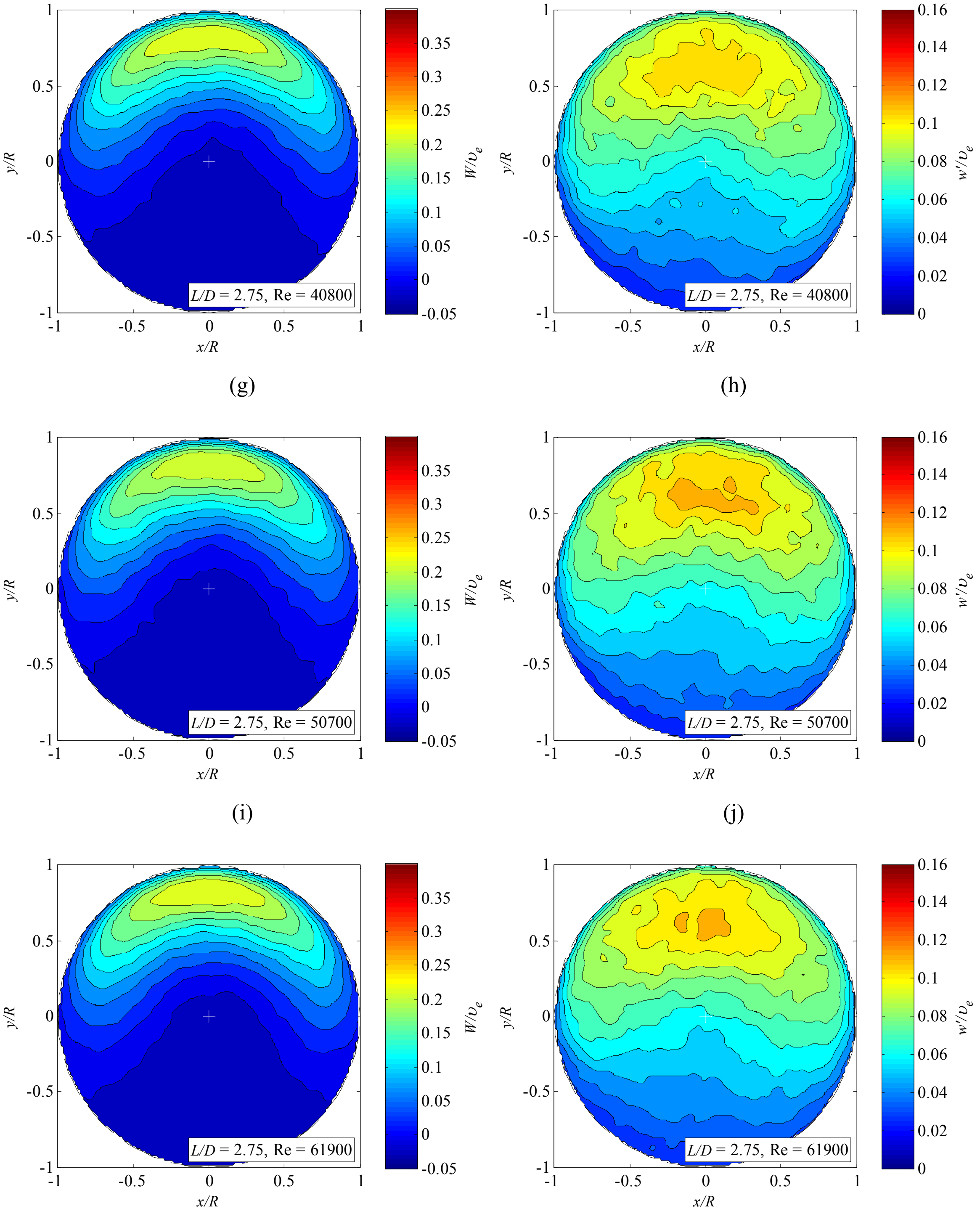

(g) (h)

(i) (j)

(k) (l)

Figure 4.19 Average and RMS axial velocity contours for chamber length *L/D* = 2.75.

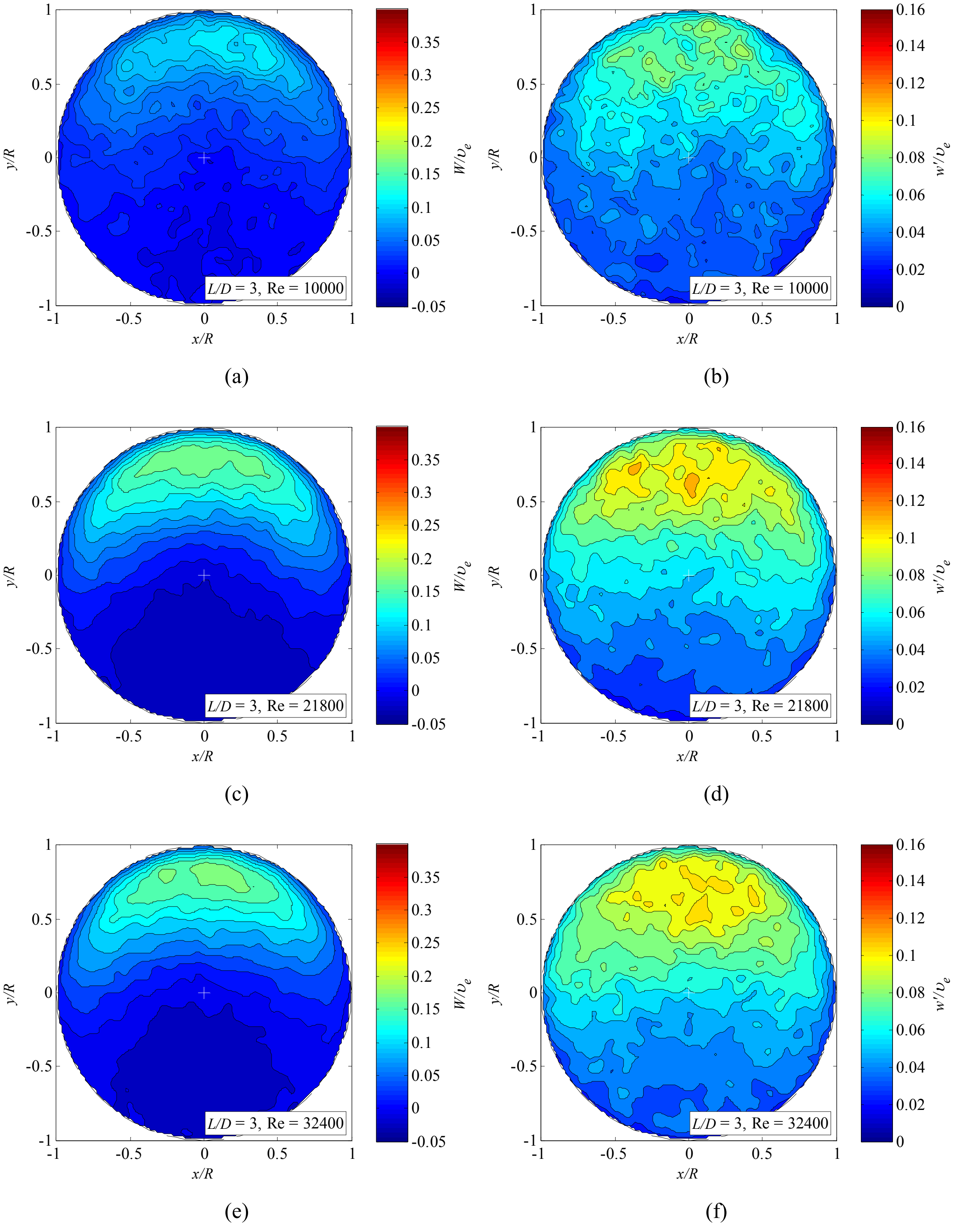

(a) (b)

(c) (d)

(e) (f)

Figure 4.20 Average and RMS axial velocity contours for chamber length *L/D* = 3.

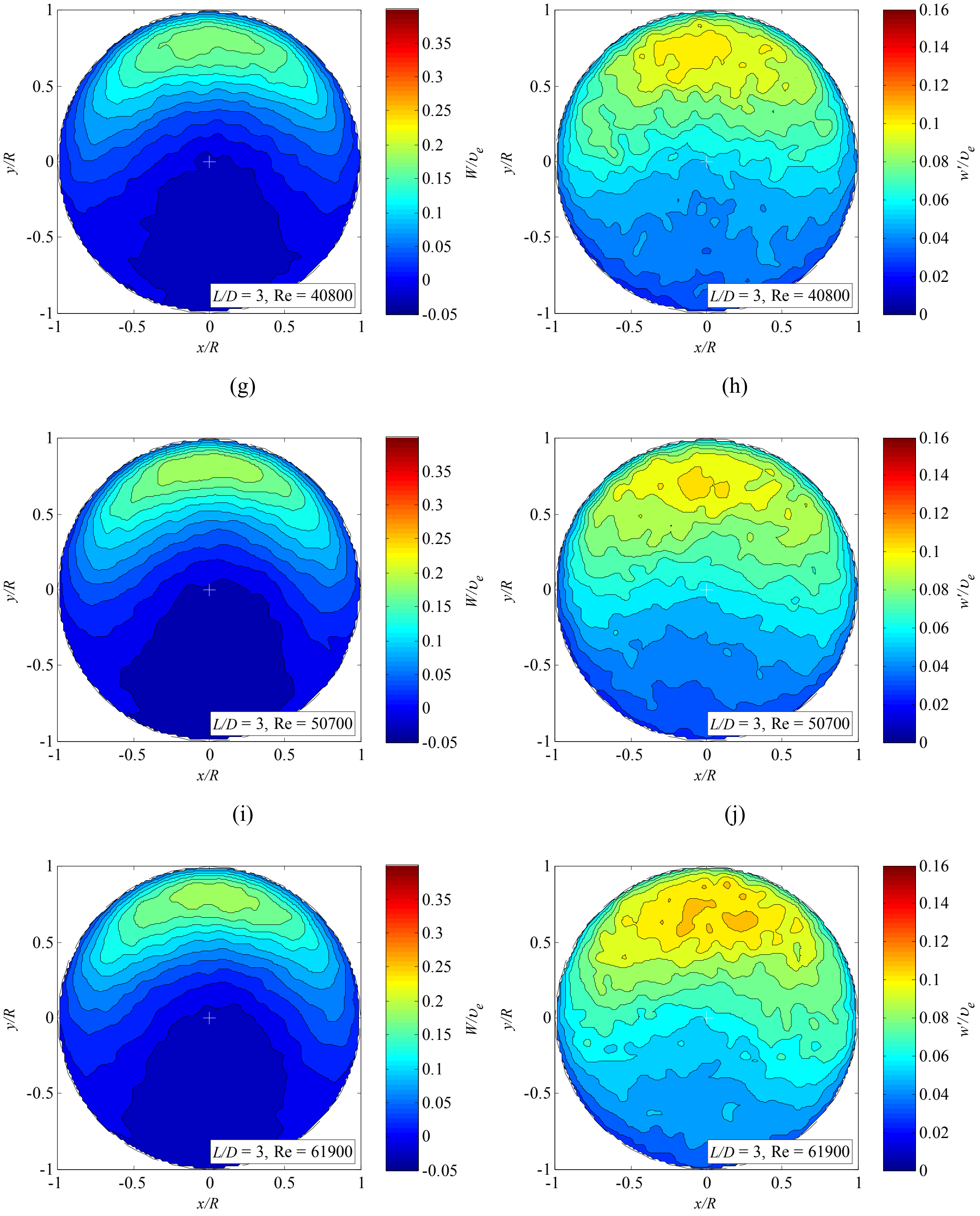

(g) (h)

(i) (j)

(k) (l)

Figure 4.20 Average and RMS axial velocity contours for chamber length *L/D* = 3.

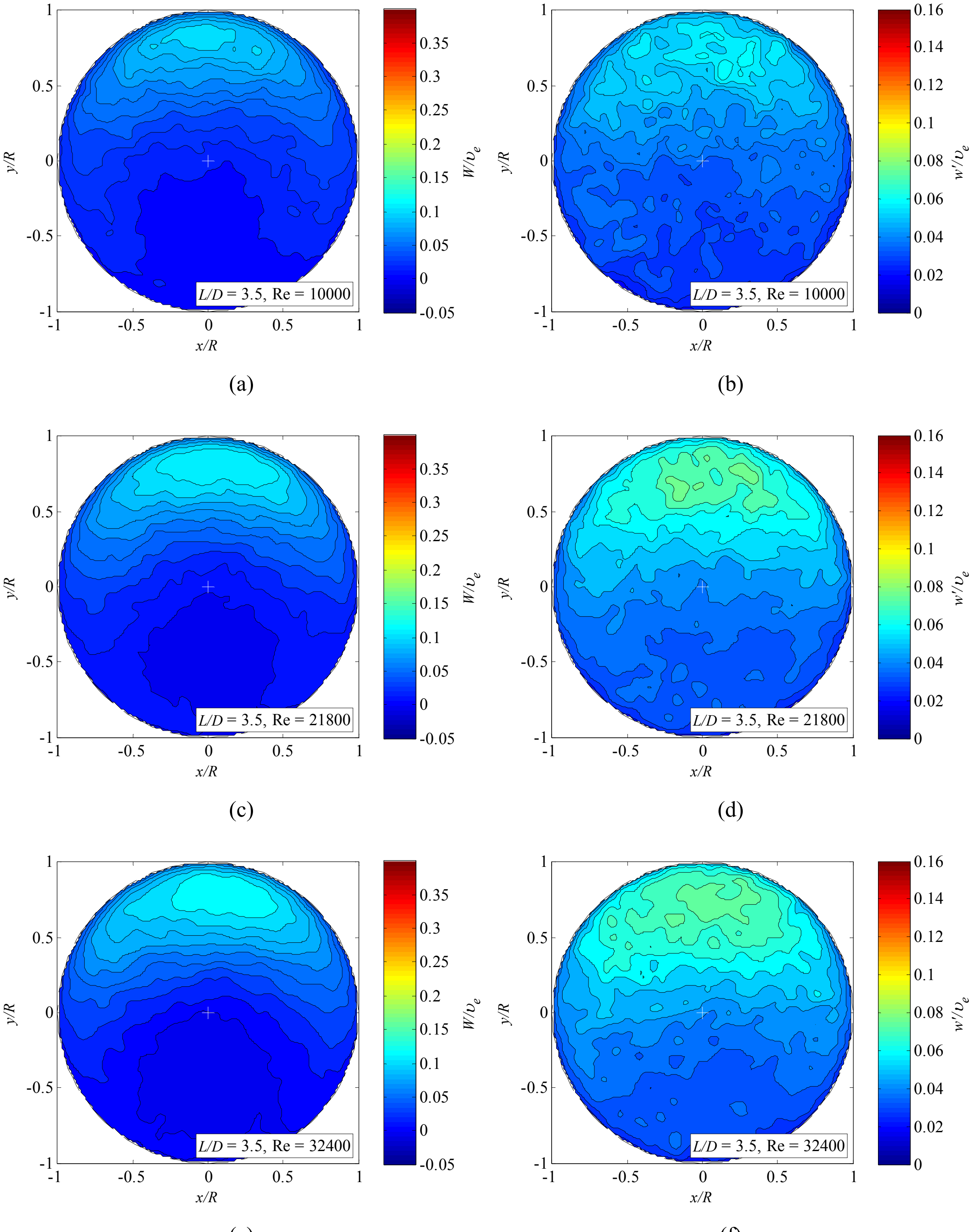

(a) (b) (c) (d) (e) (f)

Figure 4.21 Average and RMS axial velocity contours for chamber length $L/D = 3.5$.

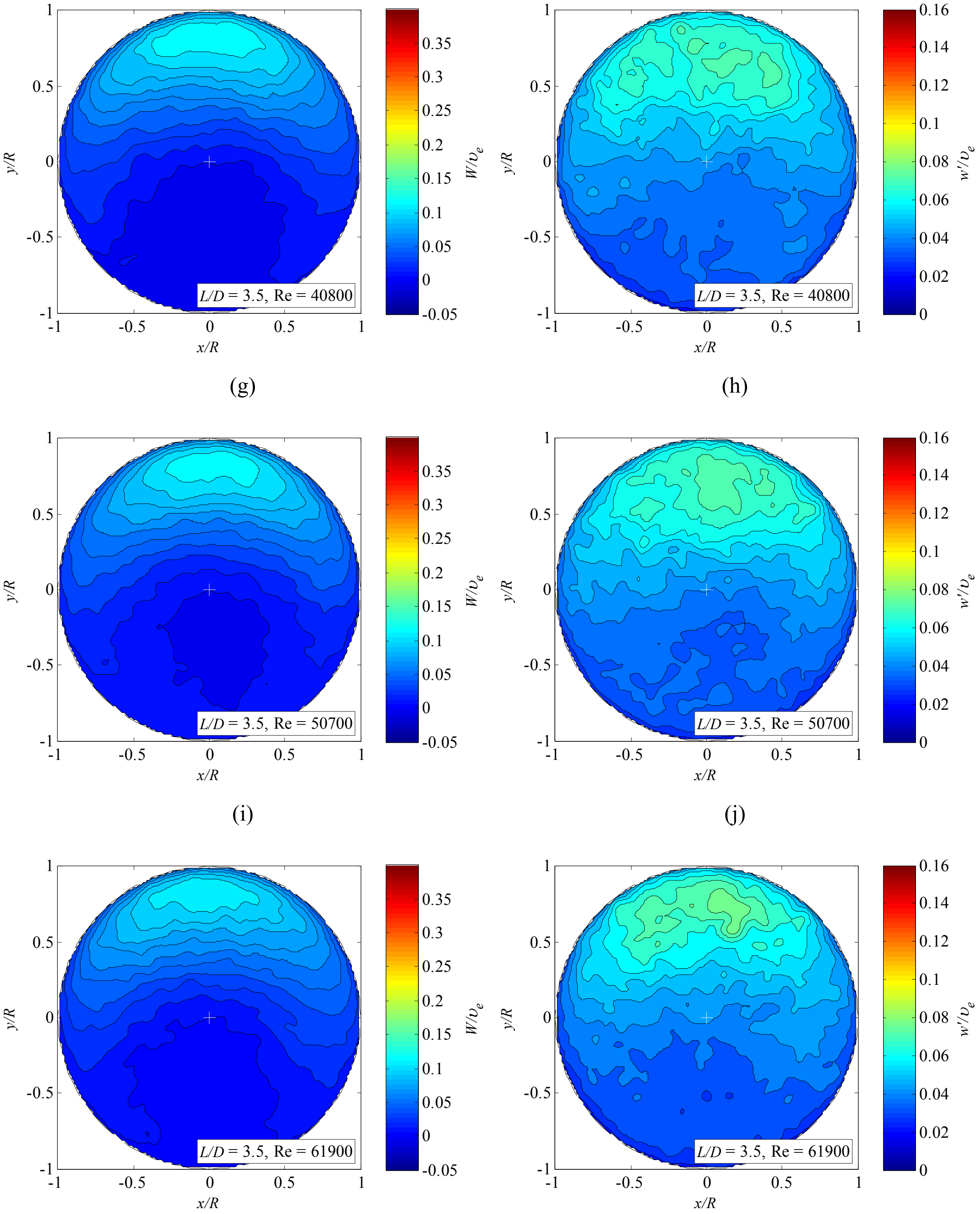

(g) (h)

(i) (j)

(k) (l)

Figure 4.21 Average and RMS axial velocity contours for chamber length $L/D = 3.5$.

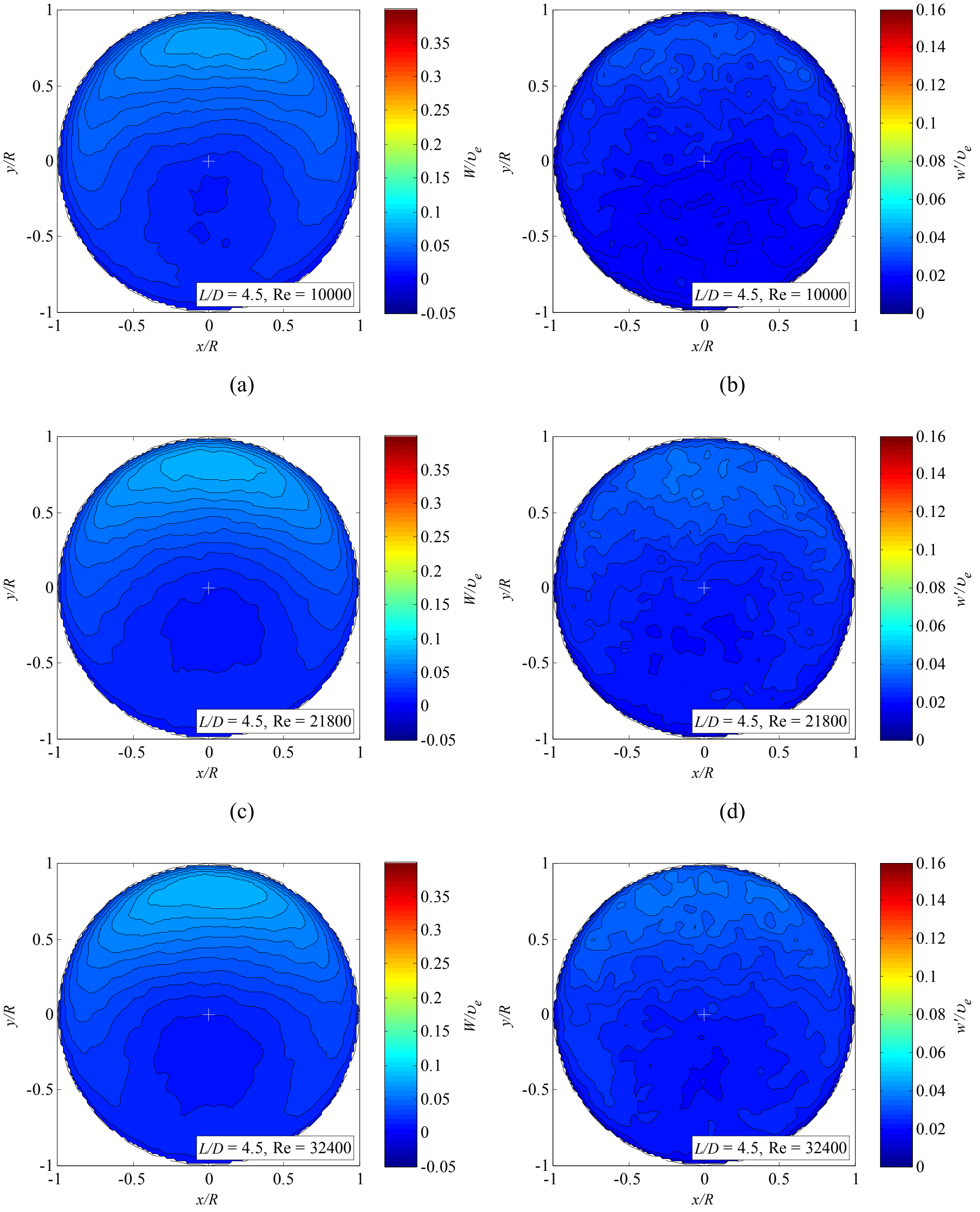

(a) (b)

(c) (d)

(e) (f)

Figure 4.22 Average and RMS axial velocity contours for chamber length *L/D* = 4.5.

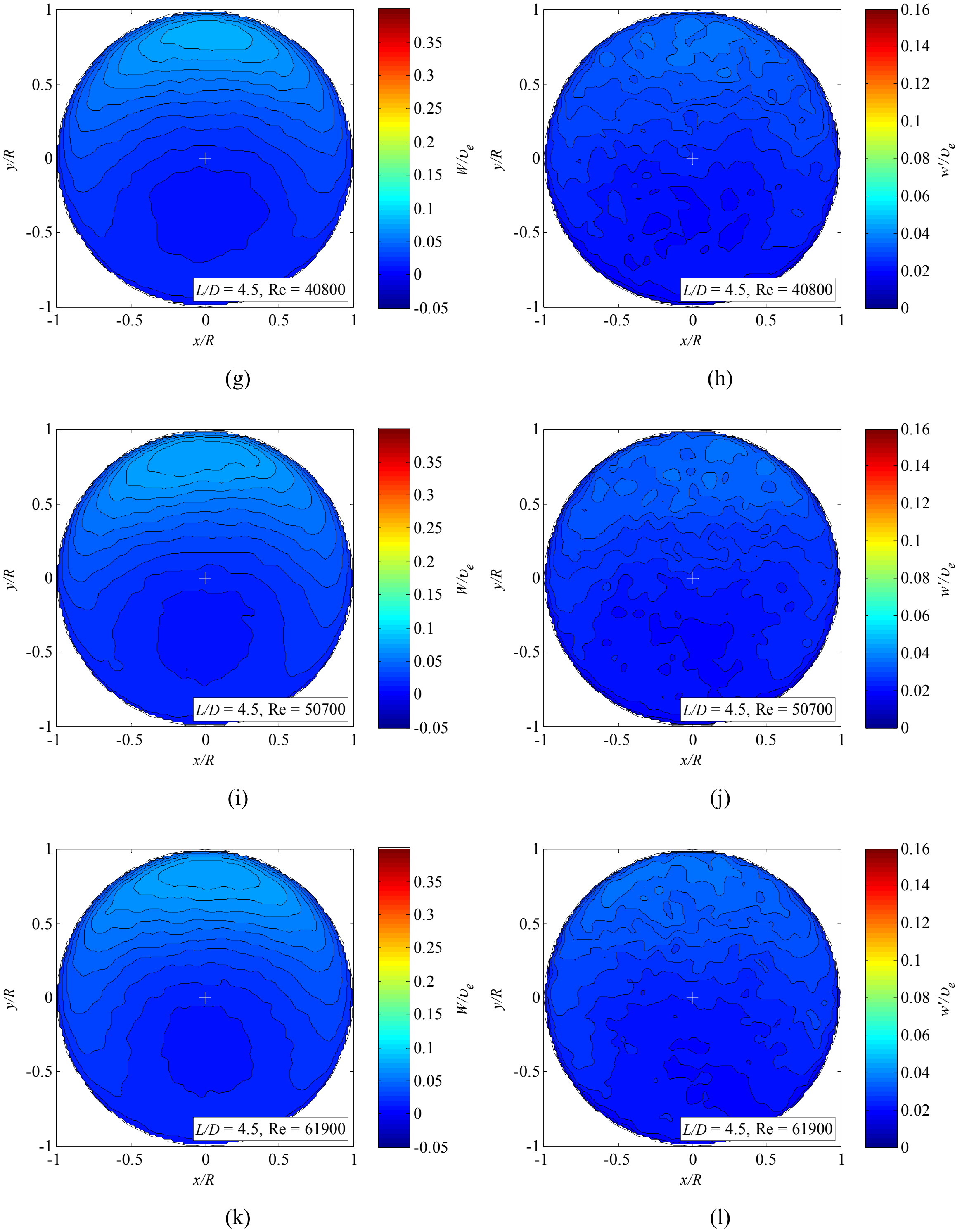

(g) (h)

(i) (j)

(k) (l)

Figure 4.22 Average and RMS axial velocity contours for chamber length $L/D = 4.5$.

Figure 4.23 shows average and RMS velocity profiles along the line $x/D = 0$ for all chamber lengths at which precession mode occurred. The axial velocity data for each Reynolds number is scaled against bulk inlet velocity, υ_e, and all Reynolds numbers are presented for each chamber length. Figure 4.24 shows all average (a) and RMS (b) velocity profiles from the different chamber lengths on one plot. All Reynolds numbers are shown except $\mathrm{Re} = 10{,}000$, which exhibits a different velocity profile than the others for all chamber lengths.

The average and RMS axial velocity data collapse well for all Reynolds numbers except 10,000 (marked with ☆), which is assumed to be a laminar flow. All chamber lengths show a region of positive axial velocity between the chamber center and chamber wall, which reaches a maximum at approximately $r/R = 0.8$. On the opposite side of the chamber center, the region of entrainment back into the chamber is apparent. As chamber length increases from $L/D = 2$, the maximum average positive axial velocity out of the chamber as well as the negative axial velocity decrease in magnitude. At chamber lengths $L/D \geq 3.5$, there is no apparent entrainment back into the chamber, and at a chamber length of $L/D = 4.5$, the axial velocity profile begins to resemble that of a pipe flow. Following this trend, with a sufficiently large chamber length, the axial velocity profile of the exiting jet is assumed to be that of an axisymmetric jet issuing from a long pipe. The RMS profiles of axial velocity reveal high fluctuations in the region of highest positive axial flow, and low fluctuations in the region where fluid is being entrained back into the chamber.

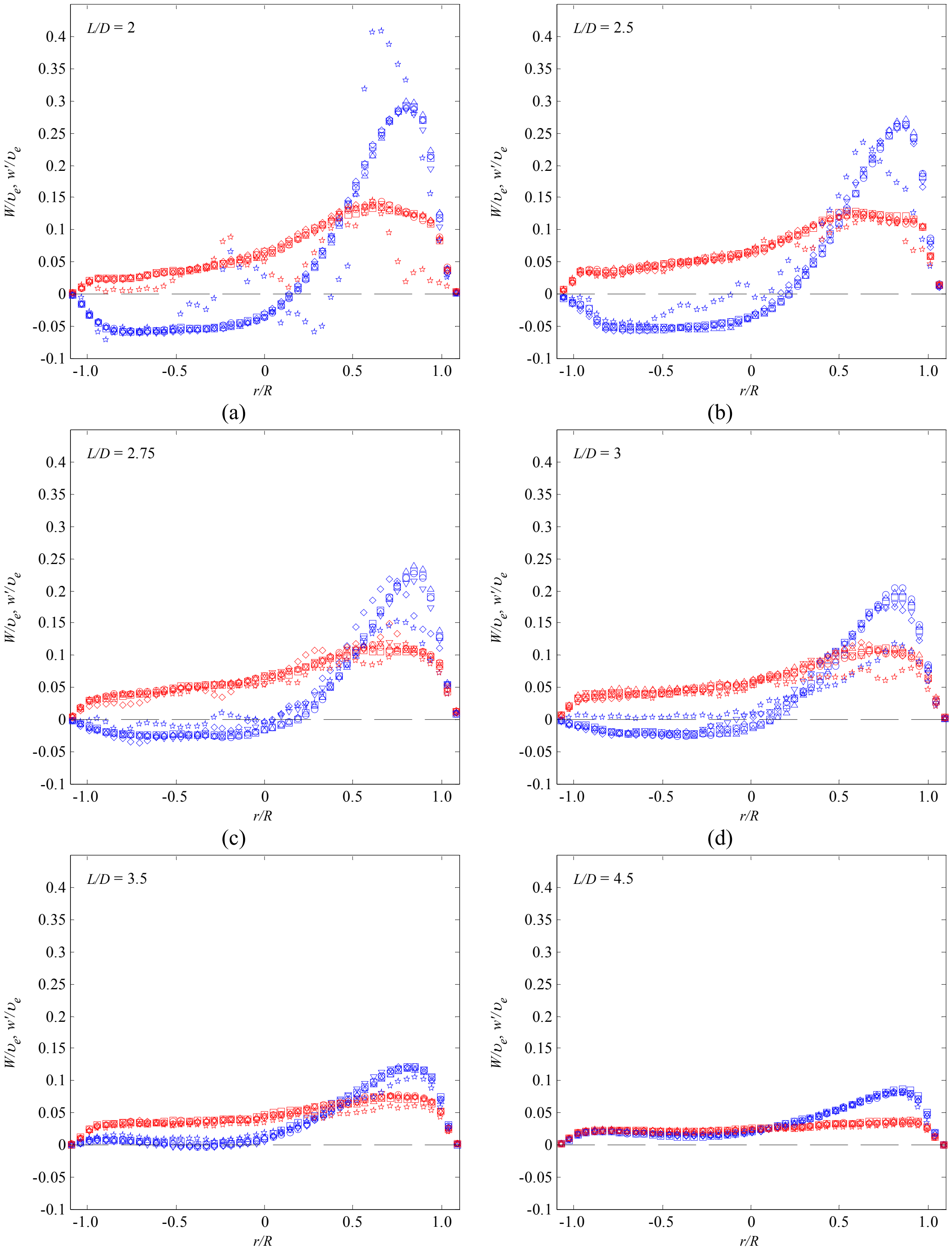

(a) (b) (c) (d) (e) (f)

Figure 4.23 Conditionally averaged axial velocity profiles along *y*-axis for different chamber lengths. Symbols represent the following Reynolds numbers: ☆ - 10,000, ◇ - 21,800, ▽ - 32,300, □ - 40,700, ○ - 50,700, △ - 61,800. Blue points represent average velocity, red represent RMS values.

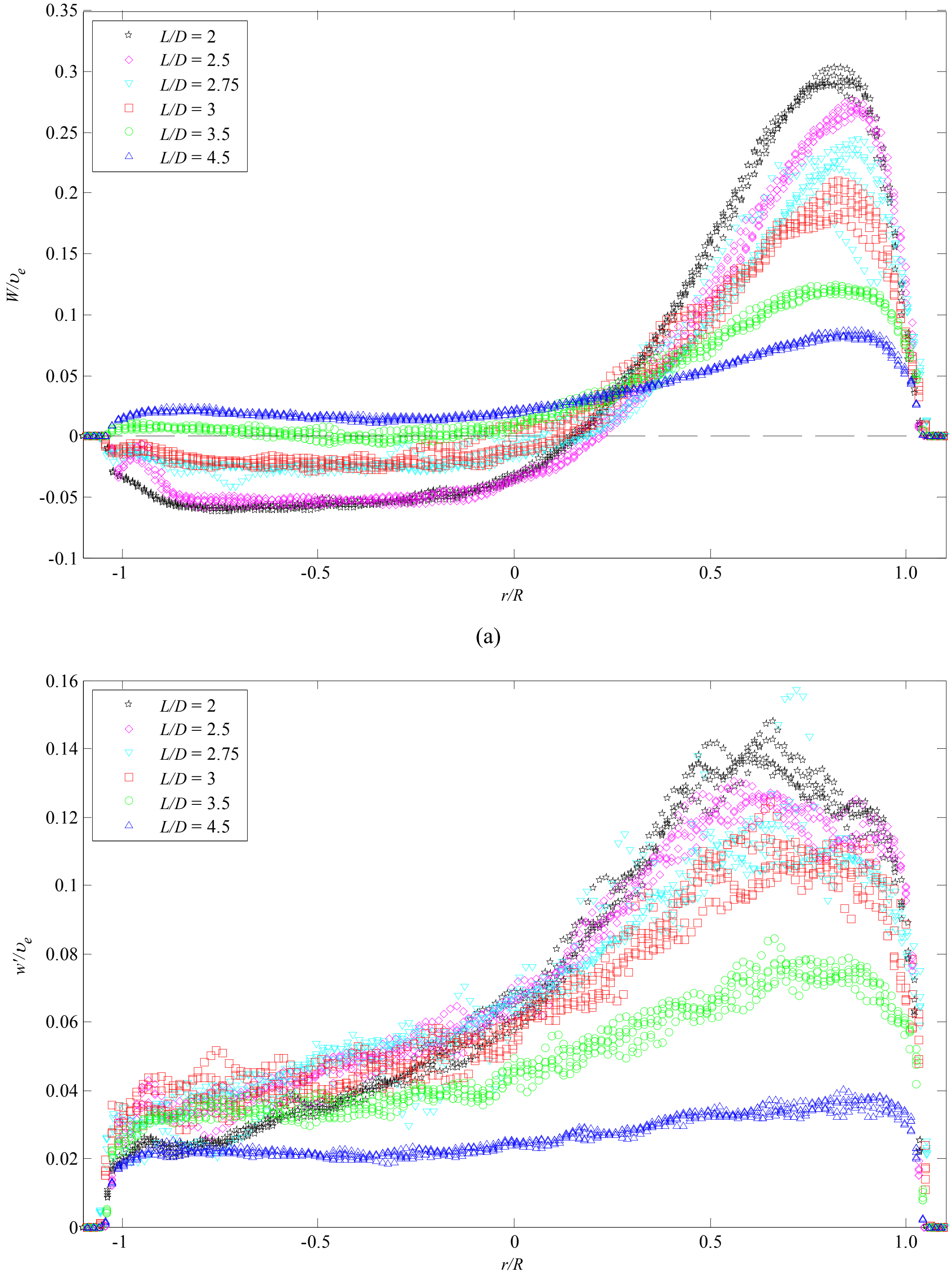

(a)

(b)

Figure 4.24 Profiles of (a) mean and (b) RMS axial velocity for all chamber lengths at all Reynolds numbers, except 10,000.

The effect of Reynolds number on the maximum positive average axial velocity out of the chamber for different chamber lengths is shown in Figure 4.25. The maximum velocity, $W_{\max}$, is scaled against bulk inlet velocity, υ_e, and chamber length is scaled against chamber diameter. Two trends are apparent in this figure. The first occurs at $\mathrm{Re} = 10{,}000$, where maximum axial velocity appears to be inversely proportional to chamber length, i.e. $W_{\max}/\upsilon_e \propto (L/D)^{-1}$. At all higher Reynolds numbers, all points collapse well onto each other, and follow a trend resembling a Gaussian distribution, with scaled maximum outflow velocity decreasing with increasing chamber length. For chamber lengths $L/D \geq 3.5$, maximum velocity values for both trends begin to converge, and at $L/D = 4.5$, they are the same.

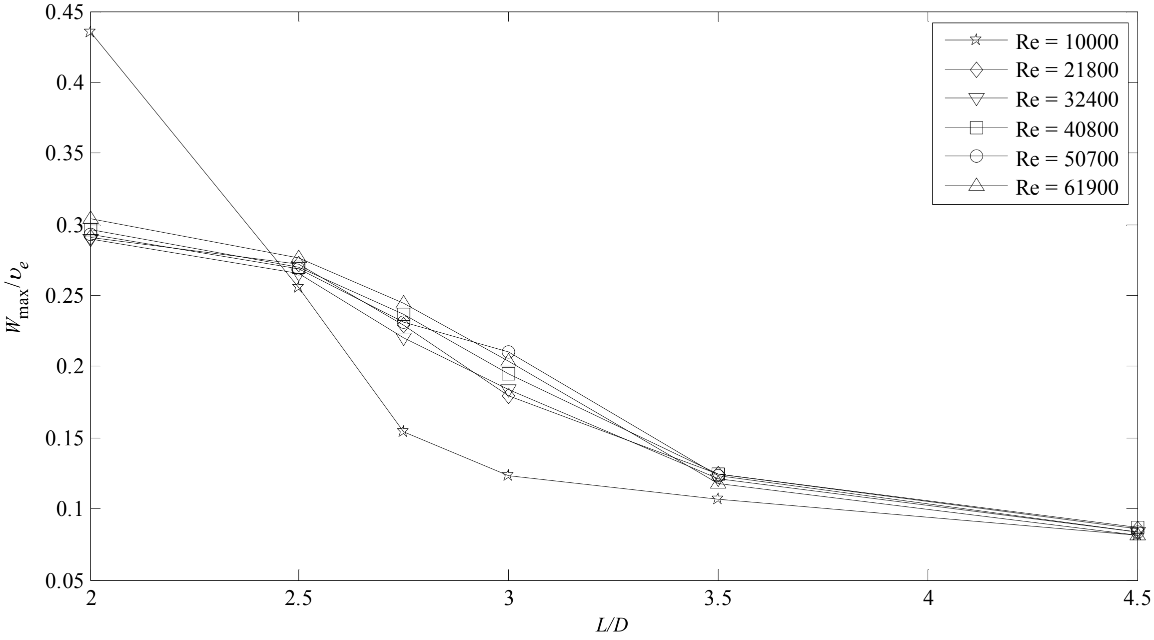

Figure 4.25 Maximum average jet velocity at different chamber lengths and Reynolds numbers

4.7.4 Chamber Length and Reynolds Number Effects on Jet Cross-Sectional Area

The influence of Reynolds number and chamber length on the area ratio, γ_c, defined in Section 4.6.3, is presented in Figure 4.26. The area ratio characterizes the relative size of the issuing jet with respect to the chamber exit area: As γ_c increases, so does the cross-sectional area of the chamber occupied by the jet. At a value of $\gamma_c = 1$, the jet occupies the entire chamber exit area and there is no entrainment back into the chamber. The figure shows an increase in γ_c with chamber length, with the area ratios reaching unity for all Reynolds numbers when $L/D = 4.5$. Two trends are apparent. One occurs at $\mathrm{Re} = 10{,}000$, where γ_c increases almost linearly over the range $2 \le L/D \le 3$, then reaches its asymptotic value of $\gamma_c = 1$ at a chamber length beyond 3.5. For all higher Reynolds numbers, the area ratios are similar in value, increasing in value more sharply in value as chamber length increases up to $L/D = 3.5$, after which they converge to unity.

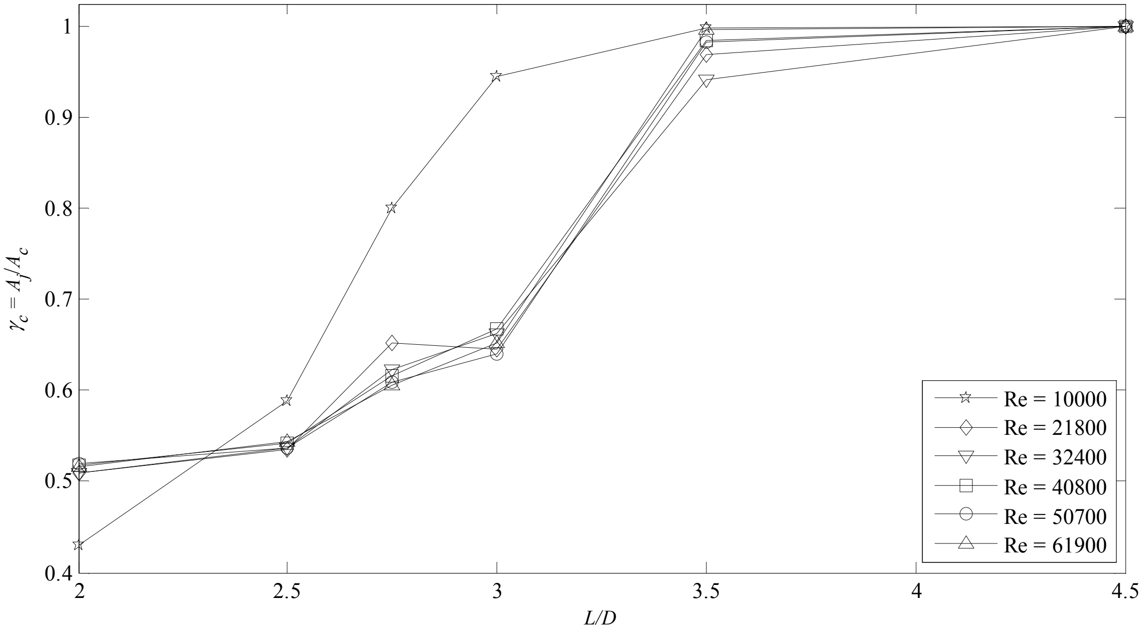

Figure 4.26 The effect of chamber length on area ratio in precessing mode at various Reynolds numbers.

4.8 Conclusions

The velocity field in the chamber exit plane of the precessing jet was studied over a range of Reynolds numbers and chamber lengths to determine the effect of these two parameters on the flow. Instantaneous velocity vector fields reveal the existence of three modes. Precessing mode is characterized by a kidney-bean shaped jet which hugs the chamber wall, with a pair of dominant, counter-rotating vortices. Axial mode is characterized by a round jet whose axis is near to the chamber axis, and no dominant vortical structure. A third mode, deemed 'transitioning mode', occurs as the jet switches between axial and precession mode. It possesses characteristics of these two modes, but is clearly neither one nor the other.

The probability of precession was found to be dependent on Reynolds number and chamber length, L/D. The probability increases with Reynolds number for all chamber lengths except $L/D=1$, at which there is no precession. The optimum chamber length to generate precession has been found to be $2 \le L/D \le 2.75$, which contradicts the optimal chamber length of Newbold (1997), who found it to be $L/D = 2.75$. The entrainment ratio, which compares the mass flux of fluid being entrained back into the chamber to the amount being discharged by the jet, was found to have a strong L/D dependence and a weak Reynolds number dependence. There is little variation in ratio between axial and precessing mode at a given Reynolds number and chamber length. The largest entrainment back into the chamber occurs at $L/D=2$, which is most desirable for burner applications.

Conditionally averaged mean axial velocity distributions reveal a smooth, crescent shaped jet, whose maximum outflow velocity is near to the chamber wall. The RMS distributions of axial velocity show highest velocity fluctuations nearest to the region of greatest outflow, which diminish gradually moving away from it in the radial direction. At a short chamber length of $L/D = 1$, there is no precession at any Reynolds number, and the jet issuing from the precession chamber is always in axial mode. At intermediate chamber lengths, $2 \leq L/D \leq 3$, the size and maximum outflow velocity behave differently for low ($\mathrm{Re} = 10{,}000$) and high ($\mathrm{Re} \geq 21{,}800$) Reynolds numbers, which implies two different flow regimes for these ranges. For high Reynolds numbers, the jet in precessing mode occupies between approximately 50% and 65% of the chamber area, increasing with chamber length and showing little Reynolds number dependence. This range is 43% to 95% at $\mathrm{Re} = 10{,}000$. For long chamber lengths, $3.5 \leq L/D \leq 4.5$ the jet occupies almost the entire cross-sectional area of the chamber, resulting in no entrainment back into the chamber, and resembles a pipe flow with higher axial velocity at one azimuthal position and lower axial velocity opposite to it.

CHAPTER 5: CONCLUSION

A parametric study was performed, which examined the effect of chamber length and Reynolds number on the stability and behavior of the flow field generated by a fluidic precessing jet nozzle. As this flow is driven by an axisymmetric jet upstream of the precession chamber, a preliminary study was performed on this fundamental flow. It addressed the universality of the self-similar solutions used to model these flows, and examined whether initial conditions continue to have an affect far downstream.

5.1 The Effect of Initial Condition on Self-Similar Behavior in an Axisymmetric Jet

The preliminary experimental investigation of the effect of initial conditions on the downstream behavior of an axisymmetric jet concludes that initial conditions remain present far downstream from the source in the self-similar region of the jet. Traditional scaling theory dictates that all jets are universal, regardless of their initial condition, and therefore are expected to spread and decay at the same rate. This study shows that jets issuing from different round nozzles, each with the same mass and momentum fluxes at a given Reynolds number, but differing in their velocity profiles at their exits and the turbulent structures which they generate, exhibit different spread and decay rates. At Reynolds numbers greater than 25,000, the coefficients corresponding to the spread and decay rates reach asymptotic values, and therefore it is concluded that the jets are fully turbulent above this Reynolds number. However, these asymptotic values are unique to the nozzle and not universal. The orifice nozzle has been shown to spread and decay the fastest, while the smooth contraction the slowest.

5.2 The Effect of Chamber Length and Reynolds Number Jet Precession

Study of the three-component flow field beyond the exit plane of the precession nozzle confirms the existence of precessing and axial flow modes. The former is characterized by a kidney-bean shaped jet exiting the precession chamber and a pair of dominant counter-rotating vortices, while axial mode resembles closely an axisymmetric jet. A third, transitioning mode, was also observed, which exhibited characteristics of both precessing and axial modes.

The chamber lengths which produce the highest probability of precession have been found to be in the range $2 \leq L/D \leq 2.75$, with the probability increasing with Reynolds number. There was no precession at any Reynolds number at $L/D = 1$. The highest entrainment of fluid back into the chamber has been found to be at a chamber length of $L/D = 2$. Entrainment was found to be independent of Reynolds number above $\mathrm{Re} \geq 21{,}800$, and flow mode.

Conditionally averaged mean and RMS axial velocity distributions were obtained for each Reynolds number and chamber length combination studied. The size of the jet as well as the maximum velocity within it were found to have a strong dependence on chamber length and follow two trends at low ($\mathrm{Re} = 10{,}000$) and high ($\mathrm{Re} \geq 21{,}800$) Reynolds numbers. It is therefore concluded that there exist two flow regimes, and the parameters examined in this thesis behave differently at high and low Reynolds numbers.

At long chamber lengths ($L/D \geq 3.5$), the issuing jet occupies more than 90% of the chamber exit area and has little or no entrainment of fluid back into the chamber. At this chamber length, the jet is precessing in the sense that is possesses a crescent-shaped region of high flow velocity which is close to the chamber wall; however, there is no entrainment back into the chamber.

5.3 Future Work

5.3.1 Axisymmetric Jet

In industrial applications, mixing and precession occur in the near-field of the nozzle, and therefore the flow phenomena occurring in this region should be further investigated. A more detailed study of the transition region for the long pipe, as well as the other nozzle configurations, is recommended, due to the presence of distinct flow instabilities that were found in this study.

5.3.2 Precessing Jet

The flow field measurements of the precessing jet were only along a two-dimensional plane at the chamber exit. This flow is highly three-dimensional, so a study of the three-component velocity field over a three-dimensional volume is recommended, using a measurement technique such as tomographic particle image velocimetry. This study would also reveal the transition from precessing to axial modes in the downstream region of the nozzle reported by Wong et al. (2008), and how the shape of the issuing jet changes in the near-field region.

The effect of chamber length on jet precession has been studied using a single configuration. As the type of nozzle (smooth contraction, orifice, etc.), as well as the presence of a lip and center body in the precession chamber, has been shown to affect the stability of precession (Wong et al., 2004), the effect of chamber length on different configurations should be examined.

REFERENCES

1. Adrian, R. J. (2005). Twenty years of particle image velocimetry. *Experiments in Fluids*, *39*, 159-169.

2. Anton, H. & Rorres, C. (2000). *Elementary linear algebra* (8th ed.). New York, NY: John Wiley & Sons.

3. Antonia, R. A., and Zhao, Q. (2001). Effect of initial conditions on a circular jet. *Experiments in Fluids*, 31, 319-323.

4. Birder, C. H., Kalt, P. A. M., & Nathan, G. J. (2009). The influences of jet precession on near field particle distributions. *International Journal of Multiphase Flow*, *35*, 288-296.

5. Carazzo, G., Kaminski, E., & Tait, S. (2006). The route to self-similarity in turbulent jets and plumes. *Journal of Fluid Mechanics*, *547*, 137-148.

6. Cohen, J. & Wygnanski, I. (1987). The evolution of instabilities in the axisymmetric jet. Part 1. The linear growth of disturbances near the nozzle. *Journal of Fluid Mechanics*, *176*, 191-219.

7. England, G., Kalt, P. A. M., Nathan, G. J., & Kelso, R. M. (2010). The effect of density ration on the near field on a naturally occurring oscillating jet. *Experiments in Fluids*, *48*(1), 69-80.

8. Fellouah, H., Ball, C. G., & Pollard, A. (2009). Reynolds number effects within the development region of a turbulent round free jet. *International Journal of Heat and*

9. George, W. K. (1989). The self-preservation of turbulent flows and its relation to initial conditions and coherent structures. In R. E. A. Arndt & W. K. George (Eds.), *Recent advances in turbulence*. New York: Hemisphere.

10. Guo, B., Langrish, T. A. G., & Fletcher, D. F. (1999). Simulation of precession in axisymmetric sudden expansion flows. *Second International Conference on CFD in the Minerals and Process Industries* (pp. 329-334). Melbourne, Australia: CSIRO.

11. Hussein, H. J., Capp, S. P., & George, W. K. (1994). Velocity measurements in a high-Reynolds-number, momentum-conserving, axisymmetric, turbulent jet. *Journal of Fluid Mechanics*, *258*, 31-75.

12. Kelso, R. M. (2001). A mechanism for jet precession in axisymmetric sudden expansions. *14th Australasian Fluid Mechanics Conference* (vol. 2, pp. 829-832). Adelaide, Australia.

13. Malmström, T. G., Kirkpatrick, A. T., Christensen, B., & Knappmiller, K. D. (1997). Centerline velocity decay measurements in low-velocity axisymmetric jets. *Journal of Fluid Mechanics*, *246*, 363-377.

14. Manias, C. G. (1994). Low NO_x clinker production. *World Cement*, *25*(5), 54-56.

15. Manias, C. G., Balendra, A., & Retallack, D. (1996). New combustion technology for lime production. *World Cement*, *27*(12), 34-39.

16. Matsuda, T. & Sakakibara, J. (2005). On the vortical structure in a round jet. *Physics of Fluids*, *17*(2).

17. Melling, A. (1997). Tracer particles and seeding for particle image velocimetry. *Measurement Science and Technology*, *8*, 1406-1416.

18. Mi, J. & Nathan, G. J. (2006). The influence of inlet flow condition on the frequency of self-excited jet precession. *Journal of Fluids and Structures*, *22*, 129-133.

19. Mi, J. & Nathan, G. J., (2004). Self-excited jet-precession Strouhal number and its influence on downstream mixing field. *Journal of Fluids and Structures*, *19*, 851-862.

20. Mi, J. Nathan, G. J., & Nobes, D. S. (2001b). Mixing characteristics of axisymmetric free jets issuing from a contoured nozzle, an orifice plate, and a pipe. *Journal of Fluids Engineering*, *123*, 878-883.

21. Mi, J., Kalt, P., Nathan, G. J., & Wong, C. Y. (2007). PIV measurements of a turbulent jet issuing from round sharp-edged plate. *Experiments in Fluids*, *42*, 625-637.

22. Mi, J., Nathan, G. J., & Luxton, R. E. (2000). Centerline mixing characteristics of jets from nine differently shaped nozzles. *Experiments in Fluids*, *28*(1), 93-94.

23. Mi, J., Nathan, G. J., & Luxton, R. E. (2001c). Mixing characteristics of a flapping jet from a self-exciting nozzle. *Flow, Turbulence, and Combustion*, *67*, 1-23.

24. Mi, J., Nathan, G. J., & Nobes, D. S. (2001a). Mixing characteristics of axisymmetric free jets from a contoured nozzle, an orifice plate, and a pipe. *Journal of Fluids Engineering*, *123*, 878-883.

25. Mi, J., Nobes, D. S., & Nathan, G. J. (2001b). Influence of jet exit conditions on the passive scalar field of an axisymmetric free jet. *Journal of Fluid Mechanics*, *432*, 91-125.

26. Nathan, G. J., Hill, S. J., & Luxton, R. E. (1998). An axisymmetric 'fluidic' nozzle to generate jet precession. *Journal of Fluid Mechanics*, *370*, 347-380.

27. Nathan, G. J., Mi, J., Alwahabi, Z. T., Newbold, G. J. R., & Nobes, D. S. (2006). Impacts of a jet's exit flow pattern on mixing and combustion performance. *Progress in Energy and Combustion Science*, *32*, 496-538.

28. Newbold, G. J. R. (1997). *Mixing and combustion in precessing jet flows*. Doctoral dissertation, Department of Mechanical Engineering, University of Adelaide, Adelaide, Australia.

29. Panchapakesan, N. R. & Lumley, J. L. (1993). Turbulence measurements in axisymmetric jets of air and helium. Part 1. Air jet. *Journal of Fluid Mechanics*, *246*, 197-223.

30. Panton, R. L. (2005). *Incompressible flow*. Hoboken, NJ: John Wiley & Sons.

31. Papadoupulos, G. and Pitts, W. M. (1998). Scaling the near-field centerline mixing behavior of axisymmetric turbulent jets. *AIAA Journal*, *36*(9), 1635-1642.

32. Peterson, J. & Bayazitoglu, Y. (1992) Measurements of velocity and turbulence in vertical axisymmetric isothermal and buoyant jets. *Journal of Heat Transfer*, *114*, 135-142.

33. Picano, F. & Casciola, C. M. (2007). Small-scale isotropy and universality of axisymmetric jets. *Physics of Fluids*, *19*, 1-4.

34. Pope, S. P. (2000). *Turbulent flows*. Cambridge, United Kingdom: Cambridge University Press.

35. Prasad, A. K. (2000). Stereoscopic particle image velocimetry. *Experiments in Fluids*, *29*, 103-116.

36. Pratt, V. (1987). Direct least-squares circle fitting. *Computer Graphics*, *6*(4), 145-152.

37. Raffel, M., Willert, C., Wereley, S., and Kompenhans, J. (1998). *Particle image velocimetry: A practical guide*. New York, NY: Springer-Verlag.

38. Rajaratnam, N. (1976). *Turbulent jets*. New York, NY: Elsevier.

39. Schneider, G. M., Froud, D., Syred, N., Nathan, G. J., & Luxton, R. E. (1997). Velocity measurements in a precessing jet flow using a three dimensional LDA system. *Experiments in Fluids*, *23*, 89-98.

40. Shineeb, A. M., Bugg, J. D., & Balachandar, R. (2008). Quantitative investigation of vortical structures in the near-exit region of an axisymmetric turbulent jet. *Journal of Turbulence*, *9*(19), 1-20.

41. Townsend, A. A. (1976). *The structure of turbulent shear flows* (2nd ed.). Cambridge, United Kingdom: Cambridge University Press.

42. Tso, J. & Hussain, F. (1989). Organized motions in a fully developed turbulent axisymmetric jet. *Journal of Fluid Mechanics*, *203*, 425-448.

43. Uddin, M., & Pollard, A. (2007). Self-similarity of coflowing jets: The virtual origin. *Physics of Fluids*, *19*, 428-431.

44. van Doorne, C. W. H. & Westerweel, J. (2007). Measurement of laminar, transitional, and turbulent pipe flow using Stereoscopic-PIV. *Experiments in Fluids*, *42*, 259-279.

45. van Doorne, C. W. H., Westerweel, J. & Nieuwstadt, F. T. M. (2003). Measurement uncertainty of Stereoscopic-PIV for flow with large out-of-plane motion. In M. Stanislas, J. Westerweel, & J. Kompenhans (Eds.), *Particle image velocimetry: Recent improvements* (pp. 213-227). Berlin, Germany: Springer.

46. Weisgraber, T. H. & Liepmann, D. (1998). Turbulent structure during transition to self-similarity in a round jet. *Experiments in Fluids*, *24*, 210-224.

47. White, F. M. (2003). *Fluid Mechanics* (5th ed.). New York, NY: McGraw Hill.

48. Wieneke, B. (2005). Stereo-PIV using self-calibration on particle images. *Experiments in Fluids*, *39*, 267-280.

49. Willert, C. E. & Gharib, M. (1991). Digital particle image velocimetry. *Experiments in Fluids*, *10*, 181-193.

50. Wong, C. Y., Lanspeary, P. V., Nathan, G. J., Kelso, R. M., & O'Doherty, T. (2003). Phase averaged velocity in a fluidic precessing jet nozzle and in its near external field. *Experimental Thermal and Fluid Science*, *27*, 515-524.

51. Wong, C. Y., Nathan, G. J, & O'Doherty, T. (2004). The effect of initial conditions on the exit flow from a fluidic precessing jet nozzle. *Experiments in Fluids*, *36*, 70-81.

52. Wong, C. Y., Nathan, G. J., & Kelso, R. M. (2008). The naturally oscillating flow emerging from a fluidic precessing jet nozzle. *Journal of Fluid Mechanics*, *606*, 153-188.

53. Wygnanski, I. & Fiedler, H. E. (1969). Some measurements in the self-preserving jet. *Journal of Fluid Mechanics*, *38*, 577-612.

54. Xu, G., & Antonia, R. A. (2002). Effect of different initial conditions on a turbulent round free jet. *Experiments in Fluids*, *33*, 677-683.

55. Zaman, K. B. M. Q. (1999). Spreading characteristics of compressible jets from nozzles of various geometries. *Journal of Fluid Mechanics*, *383*, 197-228.

APPENDIX A: DERIVATION OF THE SELF-SIMILAR SOLUTIONS FOR THE AXISYMMETRIC JET

A-1 Simplified Equations of Motion

The derivation of the self-similar solutions for the round jet begins with the Reynolds-averaged Navier-Stokes equations in a cylindrical coordinate system, shown for the three components in equations (A.1)-(A.3). With the assumption of axisymmetry, and therefore no azimuthal variation in the velocity field, all azimuthal derivates are null ($\partial/\partial\theta = 0$). Here, x, r, and θ are positional coordinates in the axial, radial, and azimuthal directions, respectively, and U_x, U_r, and U_θ are their respective averaged velocity components. The corresponding fluctuating velocity components are u_x', u_r', and u_θ'. The continuity equation in this coordinate system is given in equation (A.4). Pressure and viscosity are represented with p and ν, respectively.

$$\begin{aligned} U_r \frac{\partial U_r}{\partial r} + U_x \frac{\partial U_r}{\partial x} - \frac{U_\theta^2}{r} &= -\frac{1}{\rho}\frac{\partial p}{\partial r} + \nu\left(\frac{\partial^2 U_r}{\partial r^2} + \frac{1}{r}\frac{\partial U_r}{\partial r} - \frac{U_r}{r^2} + \frac{\partial^2 U_r}{\partial x^2}\right) \\ &\quad - \left(\frac{\partial}{\partial r}\overline{u_r'^2} + \frac{\partial}{\partial x}\overline{u_r' u_x'} + \frac{\overline{u_r'^2}}{r} - \frac{\overline{u_\theta'^2}}{r}\right) \end{aligned} \tag{A.1}$$

$$\begin{aligned} U_r \frac{\partial U_\theta}{\partial r} + U_x \frac{\partial U_\theta}{\partial x} + \frac{U_r U_\theta}{r} &= -\frac{1}{\rho}\frac{\partial p}{\partial \theta} + \nu\left(\frac{\partial^2 U_\theta}{\partial r^2} + \frac{1}{r}\frac{\partial U_\theta}{\partial r} - \frac{U_\theta}{r^2} + \frac{\partial^2 U_\theta}{\partial x^2}\right) \\ &\quad - \left(\frac{\partial}{\partial r}\overline{u_r' u_\theta'} + \frac{\partial}{\partial x}\overline{u_\theta' u_x'} + 2\frac{\overline{u_r' u_\theta'}}{r}\right) \end{aligned} \tag{A.2}$$

$$U_x \frac{\partial U_x}{\partial x} + U_r \frac{\partial U_x}{\partial r} = -\frac{1}{\rho}\frac{\partial p}{\partial x} + \nu\left(\frac{\partial^2 U_x}{\partial r^2} + \frac{1}{r}\frac{\partial U_x}{\partial r} + \frac{\partial^2 U_x}{\partial x^2}\right) - \left(\frac{\partial}{\partial r}\overline{u'_r u'_x} + \frac{\partial}{\partial x}\overline{u'^2_x} + \frac{\overline{u'_r u'_x}}{r}\right) \tag{A.3}$$

$$\frac{\partial}{\partial r} rU_r + \frac{\partial}{\partial x} rU_x = 0 \tag{A.4}$$

Rajaratnam (1976) simplifies the above equations of motion with the following assumptions:

1. There is no swirl in the flow; therefore, $U_\theta = 0$.
2. Turbulent shear stresses are much larger than their corresponding viscous stresses, resulting in the removal of viscous terms.
3. Axial velocity is much larger than radial velocity, resulting in larger velocity gradients in the radial direction than in the axial one.
4. Turbulent normal stresses are approximately equal in the radial and azimuthal directions, $\overline{u'^2_r} \approx \overline{u'^2_\theta}$.
5. The pressure gradient in the axial direction is negligible, $\partial p/\partial x \approx 0$.

These assumptions yield equations (A.5) and (A.6), which are the simplified equations for the round jet. Since the three-dimensional problem has been reduced to two dimensions, let *U* and *V* represent the axial and radial average velocity components, and u' and v' their corresponding fluctuating components.

$$U\frac{\partial U}{\partial x} + V\frac{\partial U}{\partial r} = -\frac{1}{r}\frac{\partial}{\partial r}\left(r\overline{u'v'}\right) \tag{A.5}$$

$$\frac{\partial U}{\partial x} + \frac{1}{r}\frac{\partial rV}{\partial r} = 0 \tag{A.6}$$

Equation (A.6) becomes equation (A.7), which is the momentum equation for the flow, by multiplying by ρr and integrating. Solving the terms of this equation yields equation (A.11), which dictates that there is no variation in momentum in the axial direction, and therefore momentum is conserved.

$$\int_0^\infty \rho U r \frac{\partial U}{\partial x} dr + \int_0^\infty \rho V r \frac{\partial U}{\partial r} dr = -\int_0^\infty \frac{\partial}{\partial r}\left(r\overline{u'v'}\right) dr \tag{A.7}$$

$$\int_0^\infty \rho U r \frac{\partial U}{\partial x} dr = \frac{1}{4\pi}\frac{d}{dx}\int_0^\infty 2\pi\rho u^2 r dr \tag{A.8}$$

$$\int_0^\infty \rho V r \frac{\partial U}{\partial R} dr = \left|\rho U V r\right|_0^\infty - \int_0^\infty \rho U \frac{\partial r V}{\partial r} dr = \frac{1}{4\pi}\frac{d}{dx}\int_0^\infty 2\pi\rho u^2 r dr \tag{A.9}$$

$$\int_0^\infty \frac{\partial}{\partial r}\left(r\overline{u'v'}\right) dr = \left|r\overline{u'v'}\right|_0^\infty = 0 \tag{A.10}$$

$$\frac{d}{dx}\int_0^\infty 2\pi\rho r U^2 dr = 0 \tag{A.11}$$

Integrating equation (A.11) with respect to *x* results in equation (A.12), which defines the momentum flux of the jet, $\dot{M}_0$. This quantity is a constant, and represents the rate at which momentum is added.

$$\dot{M}_0 = 2\pi\int_0^\infty \rho r U^2 dr \tag{A.12}$$

A-2 Self-Similarity Analysis

As $U = U(x,r)$ is a function of two independent variables, a self-similar solution is sought, as per Section 1.3.1. Here, the velocity along the jet's centerline, $U_{cl}(x)$ is used to scale *U*, while the radial position is scaled with $\delta = \delta(x)$, resulting in the dimensionless parameter η, defined in equation (A.13). Length scale δ is for now arbitrary, provided that it yields a self-similar solution. The axial velocity now holds the form of equation (A.14), where $f = f(\eta)$ accounts for any radial variation in axial velocity. The power-law relationship of the scaling variables U_{cl} and δ to the independent variable, *x*, is shown in equations (A.15) and (A.16). Exponents *p* and *q* are to be determined.

$$\eta = \frac{r}{\delta(x)} \tag{A.13}$$

$$\frac{U(x,r)}{U_{cl}(x)} = f(\eta) \tag{A.14}$$

$$U_{cl} \sim x^p \tag{A.15}$$

$$\delta \sim x^q \tag{A.16}$$

Substituting equations (A.13) and (A.14) into (A.11) results in:

$$2\pi \frac{d}{dx}\left[\rho U_{cl}^2 \delta^2 \int_0^\infty f^2 \eta d\eta\right] = 0 \tag{A.17}$$

The value of the integral is constant, and therefore:

$$U_{cl}^2 \delta^2 \sim x^0 \tag{A.18}$$

$$p + q = 0 \tag{A.19}$$

One more equation is necessary to evaluate *p* and *q*. Consider equation (A.6) and define $\tau = \tau(x,r)$ with equation (A.20). τ represents the Reynolds shear stress in the axial-radial direction, and is scaled in a similar manner to $U(x,y)$ in equation (A.14), resulting in equation (A.21). Similarly to $f(\eta)$, $g = g(\eta)$ accounts for any variation in τ

in the radial direction. ρU_{cl}^2 is chosen as the scaling parameter for τ as it carries the same dimensions, ensuring that g is dimensionless.

$$\tau(x,r) \equiv -\rho\overline{u'v'} \tag{A.20}$$

$$\frac{\tau}{\rho U_{cl}^2} = g(\eta) \tag{A.21}$$

The terms of equation (A.5) are then replaced with their self-similar representations ($U = U_{cl} f$, $r = \delta\eta$) and evaluated. Derivates of functions of only one variable are be expressed in prime notation, i.e. $df/d\eta = f'$, $dU_{cl}/dx = U'_{cl}$, etc.

$$\frac{\partial U}{\partial x} = U_{cl}\frac{df}{d\eta}\frac{\partial\eta}{\partial\delta}\frac{d\delta}{dx} + f\frac{dU_{cl}}{dx} = fU'_{cl} - U_{cl}\eta f'\frac{\delta'}{\delta} \tag{A.22}$$

$$U\frac{\partial U}{\partial x} = U_{cl}U'_{cl}f^2 - U_{cl}^2\eta f f'\frac{\delta'}{\delta} \tag{A.23}$$

$$\frac{\partial U}{\partial r} = \frac{\partial}{\partial r}\left(U_{cl}f\right) = \frac{1}{\delta}\frac{d}{d\eta}\left(U_{cl}f\right) = \frac{U_{cl}f'}{\delta} \tag{A.24}$$

In order to determine $V\,\partial U/\partial r$, the value of V is determined from equation (A.6), and solved in equations (A.25) - (A.27).

$$\frac{\partial}{\partial r}\left(rV\right) = -r\frac{\partial U}{\partial x} = U_{cl}\delta'\eta^2 f' - U'_{cl}\delta\eta f \tag{A.25}$$

$$\begin{aligned} rV &= \int_0^r \frac{\partial}{\partial r}\left(rV\right)dr = \int_0^r \left[U_{cl}\delta'\eta^2 f' - U'_{cl}\delta\eta f\right]dr \\ &= U_{cl}\delta'\delta\int_0^\eta \eta^2 f' d\eta - \delta^2 U'_{cl}\int_0^\eta \eta f d\eta \end{aligned} \tag{A.26}$$

$$V = \frac{U_{cl}\delta'}{\eta}\int_0^\eta \eta^2 f' d\eta - \frac{\delta U'_{cl}}{\eta}\int_0^\eta \eta f d\eta \tag{A.27}$$

For simplicity, the integrals in equation (A.27) are replaced with $F_1(\eta)$ and $F_2(\eta)$, which are defined in equations (A.28) and (A.29). Equation (A.27) then becomes (A.30).

$$F_1(\eta) \equiv \frac{1}{\eta}\int_0^\eta \eta^2 f' \mathrm{d}\eta \tag{A.28}$$

$$F_2(\eta) \equiv \frac{1}{\eta}\int_0^\eta \eta f \mathrm{d}\eta \tag{A.29}$$

$$V = U_{cl}\delta' F_1(\eta) - U'_{cl}\delta F_2(\eta) \tag{A.30}$$

$$V\frac{\partial U}{\partial r} = \frac{U_{cl}^2 \delta' f'}{\delta} F_1(\eta) - U_{cl}U'_{cl} f' F_2(\eta) \tag{A.31}$$

The right hand term in equation (A.5) is determined in equation (A.32).

$$\begin{aligned} -\frac{1}{r}\frac{\partial}{\partial r}\left(r\overline{u'v'}\right) &= \frac{1}{\rho}\frac{1}{r}\frac{\partial}{\partial r}\left(r\tau\right) = \frac{1}{r}\frac{\partial}{\partial r}\left(rU_{cl}^2 g\right) \\ &= \frac{U_{cl}^2}{r}\left(g + \frac{rg'}{\delta}\right) = \frac{U_{cl}^2}{\delta}\left(\frac{g}{\eta} + g'\right) \end{aligned} \tag{A.32}$$

Once again, to simplify the appearance of equations, $G(\eta)$ is defined in equation (A.33) and substituted into (A.29) to give equation (A.34).

$$G(\eta) \equiv \frac{g}{\eta} + g' \tag{A.33}$$

$$-\frac{1}{r}\frac{\partial}{\partial r}\left(r\overline{u'v'}\right) = \frac{U_{cl}^2}{\delta} G(\eta) \tag{A.34}$$

Substituting equations (A.23), (A.31), and (A.34) into (A.5) gives:

$$\left[U_{cl}U'_{cl} f^2 - U_{cl}^2 \eta f f' \frac{\delta'}{\delta}\right] + \left[\frac{U_{cl}^2 \delta' f'}{\delta} F_1(\eta) - U_{cl}U'_{cl} f' F_2(\eta)\right] = \frac{U_{cl}^2}{\delta} G(\eta)$$

$$G = \frac{\delta U'_{cl}}{U_{cl}}\left(f^2 - f'F_2\right) - \delta'\left(\eta f f' - f'F_1\right) \tag{A.35}$$

Since $G = G(\eta)$, all terms on the right hand of side of equation must also be functions of η. $\left(f^2 - f'F_2\right)$ and $\left(\eta f f' - f'F_1\right)$ are already only functions of η, and so equations (A.36) and (A.37) must hold true.

$$\frac{\delta U'_{cl}}{U_{cl}} \sim x^0 \tag{A.36}$$

$$\delta' \sim x^0 \tag{A.37}$$

Considering the exponents in equation (A.36) gives equation (A.38), which, when evaluated, results in $q = 1$. Substituting this value into equation (A.19) gives $p = -1$.

$$q + (p-1) - p = 0 \tag{A.38}$$

Therefore, for an axisymmetric jet, centerline velocity U_{cl} and length scale δ have the dependencies of x shown in equations (A.39) and (A.40).

$$U_{cl} \sim 1/x \tag{A.39}$$

$$\delta \sim x \tag{A.40}$$

A-3 Dimensional Analysis

The self-similar equations of the round jet can be derived by applying the Buckingham-Pi theorem (Panton, 2005) to the system. Here, the two length scales U_{cl} and δ are scaled with other known quantities of the system. These are the momentum flux of the jet, M_0, which is constant and is defined in equation (A.12), the density of the fluid, ρ, and the axial distance from the point source of momentum, x. For high

Reynolds numbers, greater than a few thousand, viscous effects may be neglected (Rajaratnam, 1976).

Solutions are sought for length scales U_{cl} and δ of the form of equations (A.41) and (A.42), respectively.

$$U_{cl} = f_1\left(\dot{M}_0, \rho, x\right) \tag{A.41}$$

$$\delta = f_2\left(\dot{M}_0, \rho, x\right) \tag{A.42}$$

The dimensional matrix of the system is shown in Table A-1. Here, M, L, and T are the primary dimensions of mass, length, and time, respectively.

Table A-1 Dimensional matrix for an axisymmetric jet

	M_0	ρ	x	U_{cl}	δ
M	1	1	0	0	0
L	1	-3	1	1	1
T	-2	0	0	-1	0

The dimensional analysis is performed below. See Panton (2005) for a detailed overview of this method.

$$\hat{\Pi}_1 = \hat{U}_{cl}\left(\hat{\dot{M}}_0\right)^{\alpha}(\hat{\rho})^{\beta}(\hat{x})^{\gamma} \tag{A.43}$$

$$\Pi_1\mathrm{M}^0\mathrm{L}^0\mathrm{T}^0 = U_{cl}\mathrm{M}^0\mathrm{L}^1\mathrm{T}^{-1} \cdot \dot{M}_0^{\alpha}\left(\mathrm{M}^1\mathrm{L}^1\mathrm{T}^{-2}\right)^{\alpha} \cdot \rho^{\beta}\left(\mathrm{M}^1\mathrm{L}^{-3}\mathrm{T}^0\right)^{\beta} \cdot x^{\gamma}(\mathrm{M}^0\mathrm{L}^1\mathrm{T}^0)^{\gamma} \tag{A.44}$$

$$\begin{array}{l} \mathrm{M}: \\ \mathrm{L}: \\ \mathrm{T}: \end{array} \begin{cases} 0 = \alpha + \beta \Rightarrow \alpha = -\beta \\ 0 = 1 + \alpha - 3\beta + \gamma \Rightarrow \gamma = 3\beta - \alpha - 1 \\ 0 = -1 - 2\alpha \Rightarrow \beta = \frac{1}{2} \end{cases} \tag{A.45}$$

Solving the system of equations in (A.45) produces $\alpha = -\frac{1}{2}$, $\beta = \frac{1}{2}$, and $\gamma = 1$. Substituting these values into equation (A.44) gives the first Π-group, as shown in equation (A.46). K_1 is a constant which can be determined experimentally, and represents the decay rate of the jet.

$$\Pi_1 = U_{cl} x \sqrt{\frac{\rho}{\dot{M}_0}} = K_1 \tag{A.46}$$

Assuming uniform axial velocity throughout the nozzle exit plane, momentum flux, can be expressed in terms of the centerline velocity at the jet nozzle, U_0, as in equation (A.47). Here, *d* is the diameter of the nozzle.

$$\dot{M}_0 = \frac{\pi}{4} \rho d^2 U_0^2 \tag{A.47}$$

Substituting equation (A.47) into (A.46) and rearranging yields equation (A.48), which relates centerline velocity to downstream distance from a point source of momentum. Note that $\pi/4$ is absorbed into K_1.

$$\frac{U_0}{U_{cl}} = \frac{1}{K_1} \frac{x}{d} \tag{A.48}$$

The length scale δ is has its functional dependency determined in a similar manner.

$$\hat{\Pi}_2 = \delta \left(\hat{\dot{M}}_0 \right)^{\alpha} (\hat{\rho})^{\beta} (\hat{x})^{\gamma} \tag{A.49}$$

$$\Pi_2 \mathrm{M}^0\mathrm{L}^0\mathrm{T}^0 = \delta \mathrm{M}^0\mathrm{L}^1\mathrm{T}^0 \cdot \dot{M}_0^{\alpha} \left(\mathrm{M}^1\mathrm{L}^1\mathrm{T}^{-2}\right)^{\alpha} \cdot \rho^{\beta} \left(\mathrm{M}^1\mathrm{L}^{-3}\mathrm{T}^0\right)^{\beta} \cdot x^{\gamma} \left(\mathrm{M}^0\mathrm{L}^1\mathrm{T}^0\right)^{\gamma} \tag{A.50}$$

$$\begin{array}{ll} \mathrm{M}: & \multirow{3}{*}{} \\ \mathrm{L}: & \\ \mathrm{T}: & \end{array} \begin{cases} 0 = \alpha + \beta \Rightarrow \alpha = -\beta \\ 0 = 1 + \alpha - 3\beta + \gamma \Rightarrow \gamma = 3\beta - \alpha - 1 \\ 0 = 0 - 2\alpha \Rightarrow \beta = 0 \end{cases} \tag{A.51}$$

Solving the system of equations in (A.45) gives $\alpha = 0$, $\beta = 0$, and $\gamma = -1$, yielding the second Π-group, shown in equation (A.52). K_2 is another constant, which is also determined experimentally, and represents the spreading rate of the jet. Rearranging produces equation (A.53).

$$\Pi_2 = K_2 = \frac{\delta}{x} \tag{A.52}$$

$$\frac{\delta}{x} = K_2 \tag{A.53}$$

As the distance from the idealized point source of momentum (i.e. virtual origin) to the nozzle is not necessarily zero, equations (A.54) and (A.55) may be expressed in terms of the axial distance from the nozzle. Let x' represent this distance. The nozzle and point source of momentum are separated by $x_o = x' - x$, which is the location of the virtual origin of the jet relative to the nozzle. This value can be determined experimentally. The axial distance from the point source of momentum can then be expressed in terms of the distance from the nozzle and the virtual origin, x_o, as shown in equation (A.56). Substituting (A.56) into (A.48) and (A.53) yields equations (A.57) and (A.58).

$$x = x' - x_0 \tag{A.56}$$

$$\frac{U_0}{U_{cl}} = \frac{1}{K_1}\frac{x' - x_0}{d} \tag{A.57}$$

$$\frac{\delta}{x' - x_0} = K_2 \tag{A.58}$$

A final simplification to the equations is made. The dimensionless axial distance, χ, is defined in equation (A.59). Substituting it into equations (A.57) and (A.58) results in equations (A.60) and (A.61).

$$\chi \equiv \frac{x' - x_o}{d} \tag{A.59}$$

$$\frac{U_0}{U_{cl}} = \frac{1}{K_1}\chi \tag{A.60}$$

$$\frac{\delta}{d} = K_2 \chi \tag{A.61}$$

APPENDIX B: DERIVATION OF THE SELF-SIMILAR EQUATIONS - THE APPROACH OF GEORGE (1989)

This appendix contains an alternate derivation of the self-similarity solution for an axisymmetric jet, as presented by George (1989). The modified derivation begins with the simplified equations of motion for the round jet, shown in equations (B.1) and (B.2) and derived in Appendix A-1. The momentum integral is shown in equation (B.3), and is identical to (A.12).

$$U\frac{\partial U}{\partial x}+V\frac{\partial U}{\partial r}=-\frac{1}{r}\frac{\partial}{\partial r}\left(r\overline{u'v'}\right) \tag{B.1}$$

$$\frac{\partial U}{\partial x}+\frac{1}{r}\frac{\partial rV}{\partial r}=0 \tag{B.2}$$

$$\dot{M}_0=2\pi\rho\int_0^\infty U^2 r dr \tag{B.3}$$

In the same manner as the traditional approach to a self-similar solution for the jet derived in Appendix A, self-similar solutions are sought for $U(x,r)$ and $\tau(x,r)=-\rho\overline{u'v'}$. Differing slightly from the traditional approach, let the length scales for $U(x,r)$ and $\tau(x,r)$ be $U_s(x)$ and $R_s(x)$, respectively, which for the time being remain arbitrary. The self-similar equations are then (B.4) and (B.5). Length scale η is defined in equation (B.6).

$$\frac{U(x,r)}{U_s(x)}=f(\eta) \tag{B.4}$$

$$\frac{\tau(x,r)}{R_s(x)}=g(\eta) \tag{B.5}$$

$$\eta = \frac{r}{\delta(x)} \tag{B.6}$$

In a similar manner to Appendix A-2, equations (B.2)-(B.6) are substituted into (B.1) and solved, yielding:

$$\begin{aligned} U_s U_s' f^2 - U_s \eta f f^2 \frac{\delta'}{\delta} + \frac{U_s f'}{\delta}\left[\frac{U_s \delta'}{\eta}\int_0^{\eta} f'\eta^2 d\eta - \delta U_s' \int_0^{\eta} f\eta d\eta\right] \\ = \frac{R_s}{\delta}\left(\frac{g}{\eta} + g'\right) \end{aligned} \tag{B.7}$$

Rearranging and multiplying by δ / U_{cl}^2 gives equation (B.8)

$$\frac{\delta}{U_s} U_{cl}' f^2 - \left[\frac{\delta}{U_s} U_s' + 2\delta'\right]\frac{f'}{\eta}\int_0^{\eta} f\eta d\eta = \left[\frac{R_s}{U_s}\right]\left(\frac{g}{\eta} + \eta'\right) \tag{B.8}$$

The momentum integral is obtained similarly, by substituting equations (B.4) and (B.6) into (B.3).

$$\dot{M}_0 = \left[U_s^2 \delta^2\right] 2\pi\rho \int_0^{\infty} f^2 \eta d\eta \tag{B.9}$$

Equations (B.8) and (B.9) are the same as those derived in Appendix A-2; however, their functional dependencies have not yet been assumed and must still be determined. Owing to the momentum flux being constant, $U_s \propto 1/\delta$. Let then U_s be defined as in equation (B.10). Here, B is an arbitrary parameter.

$$U_s = \frac{B}{\delta}\sqrt{\frac{\dot{M}_0}{\rho}} \tag{B.10}$$

Substituting equation (B.10) into (B.8) and (B.9) gives equations (B.11) and (B.12).

$$\delta'\left(f^2 + \frac{f'}{\eta}\int_0^\eta f\eta d\eta\right) = \frac{R_s}{U_s^2}\left(\frac{g}{\eta} + g'\right) \tag{B.11}$$

$$2\pi\int_0^\infty f^2 d\eta = \frac{1}{B^2} \tag{B.12}$$

Considering that the bracketed terms in equation (B.11) are functions of only η, then equation (B.13) must be satisfied for a self-similar solution.

$$\delta' \sim \frac{R_s}{U_s^2} \tag{B.13}$$

If initial conditions do affect the self-similar solutions, then their influence must be through δ, R_s, and U_s. George (1989) avoids a point-source of momentum solution, and instead considers a point-source of mass, $\dot{m}_0$, as well as a point-source of momentum, $\dot{M}_0$. Functional dependencies of δ, R_s, and U_s are sought which are functions of axial distance, *x*, fluid density, ρ, as well as $\dot{m}_0$ and $\dot{M}_0$, as shown in equations (B.14)-(B.16).

$$U_s = f\left(x, \rho, \dot{m}_0, \dot{M}_0\right) \tag{B.14}$$

$$R_s = f\left(x, \rho, \dot{m}_0, \dot{M}_0\right) \tag{B.15}$$

$$\delta = f\left(x, \rho, \dot{m}_0, \dot{M}_0\right) \tag{B.16}$$

A new length scale can be defined, as per equation (B.17). No longer is *x* the only length scale.

$$L \equiv \frac{\dot{m}_0}{\dot{M}_0^{1/2}} \tag{B.17}$$

On dimensional grounds, solutions which reduce to the equivalent point-source of momentum solutions as the mass flux approaches zero can be written as equations (B.18)-(B.20). $F_1 = F_1(x/L)$, $F_2 = F_2(x/L)$, and $F_3 = F_3(x/L)$ are arbitrary functions.

$$U_s = \frac{\sqrt{\dot{M}_0/\rho}}{x} F_1\left(\frac{x}{L}\right) \tag{B.18}$$

$$R_s = \frac{\dot{M}_0}{\rho x^2} F_2\left(\frac{x}{L}\right) \tag{B.19}$$

$$\delta = x F_3\left(\frac{x}{L}\right) \tag{B.20}$$

Allowing the initial momentum flux to approach zero, i.e. $\dot{m}_0 \to 0$ resulting in $x/L \to \infty$, as would be the case when considering equations (B.18)-(B.20) as a point-source of momentum, they take the form of equations (B.21)-(B.23).

$$\lim_{\frac{x}{L}\to\infty} F_1\left(\frac{x}{L}\right) \to 1 \tag{B.21}$$

$$\lim_{\frac{x}{L}\to\infty} F_2\left(\frac{x}{L}\right) \to 1 \tag{B.22}$$

$$\lim_{\frac{x}{L}\to\infty} F_3\left(\frac{x}{L}\right) \to A \tag{B.23}$$

George (1989) states that $A = d\delta/dx$ must be a universal constant (which was previously chosen as unity), and if this is correct, then the substitution of equations (B.18)-(B.20) into the modified momentum equations (B.11) and (B.12) should yield differential forms of the x-dependent coefficients. The solutions to these must asymptote to equations (B.21)-(B.23), regardless of initial condition.

Differentiating equation (B.20) and substituting it and equations (B.18) and (B.19) into (B.11) yields the condition for self-similarity, given in equation (B.24). This equation is not only satisfied by the limiting case of the point-source of momentum approach, but instead by all solutions satisfying equation (B.25).

$$1+\left(\frac{x}{L}\right)\frac{F_3'}{F_3}\sim\frac{F_2}{F_3F_1^2} \tag{B.24}$$

$$F_3\sim\frac{F_2}{F_1^2}\sim\left(\frac{x}{L}\right)^k \tag{B.25}$$

In equation (B.25), the constants of proportionality, as well as exponent k, are arbitrary, resulting in a myriad of self-similar solutions. George (1989) concludes that for the case of $k=0$, which corresponds to the x-dependence of the point-source of momentum solution of Appendix A, there are many source-dependant possibilities for the constants of proportionality, and therefore different jets can spread and decay at different rates.

APPENDIX C: SCHEMATIC DRAWINGS OF THE NOZZLES AND CHAMBERS USED

This appendix presents the schematic drawings of the supply pipe, nozzles and precession chamber used in this thesis.

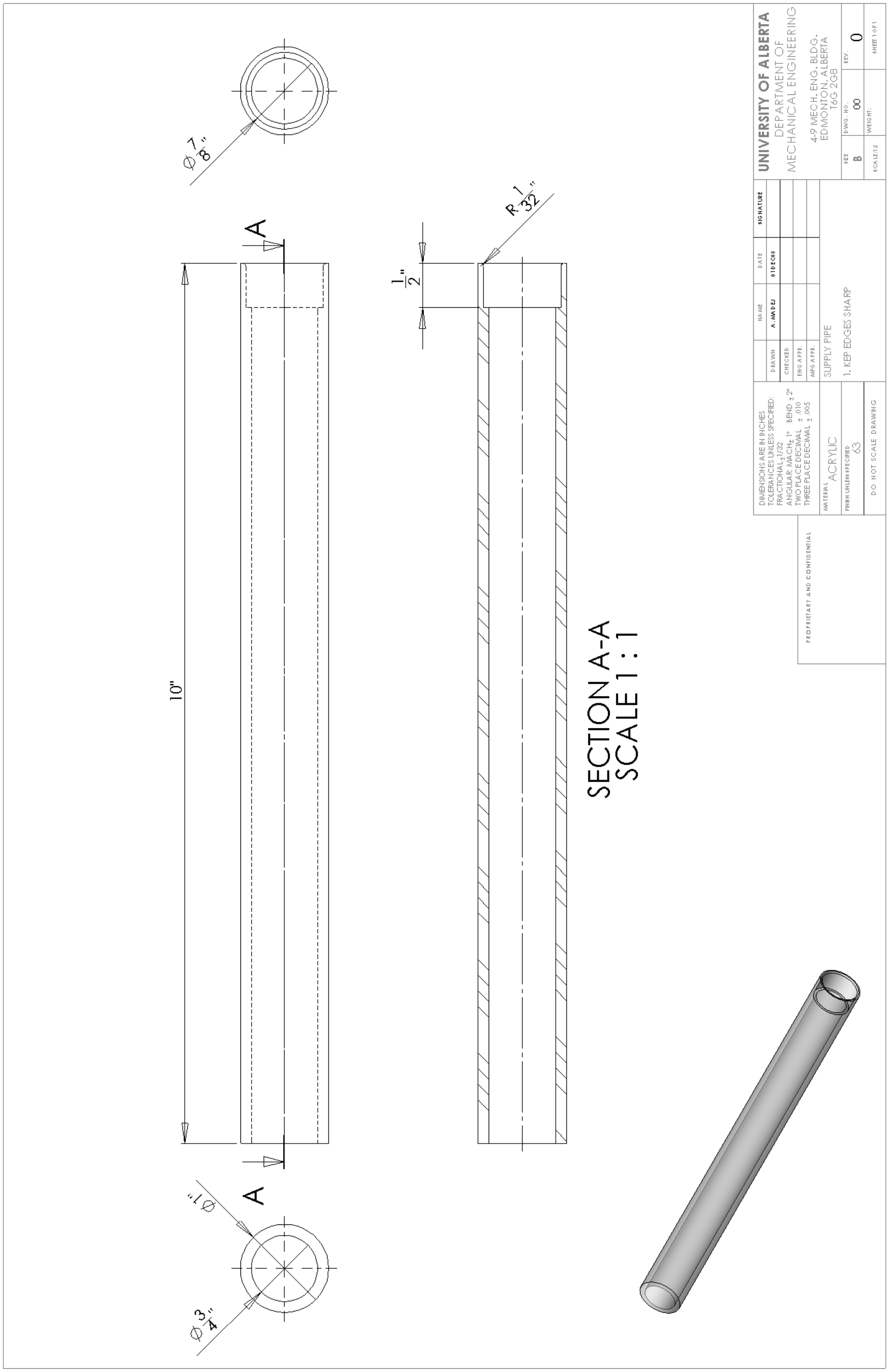

Figure C.1 Schematic drawing of the supply pipe connecting the nozzle and plenum.

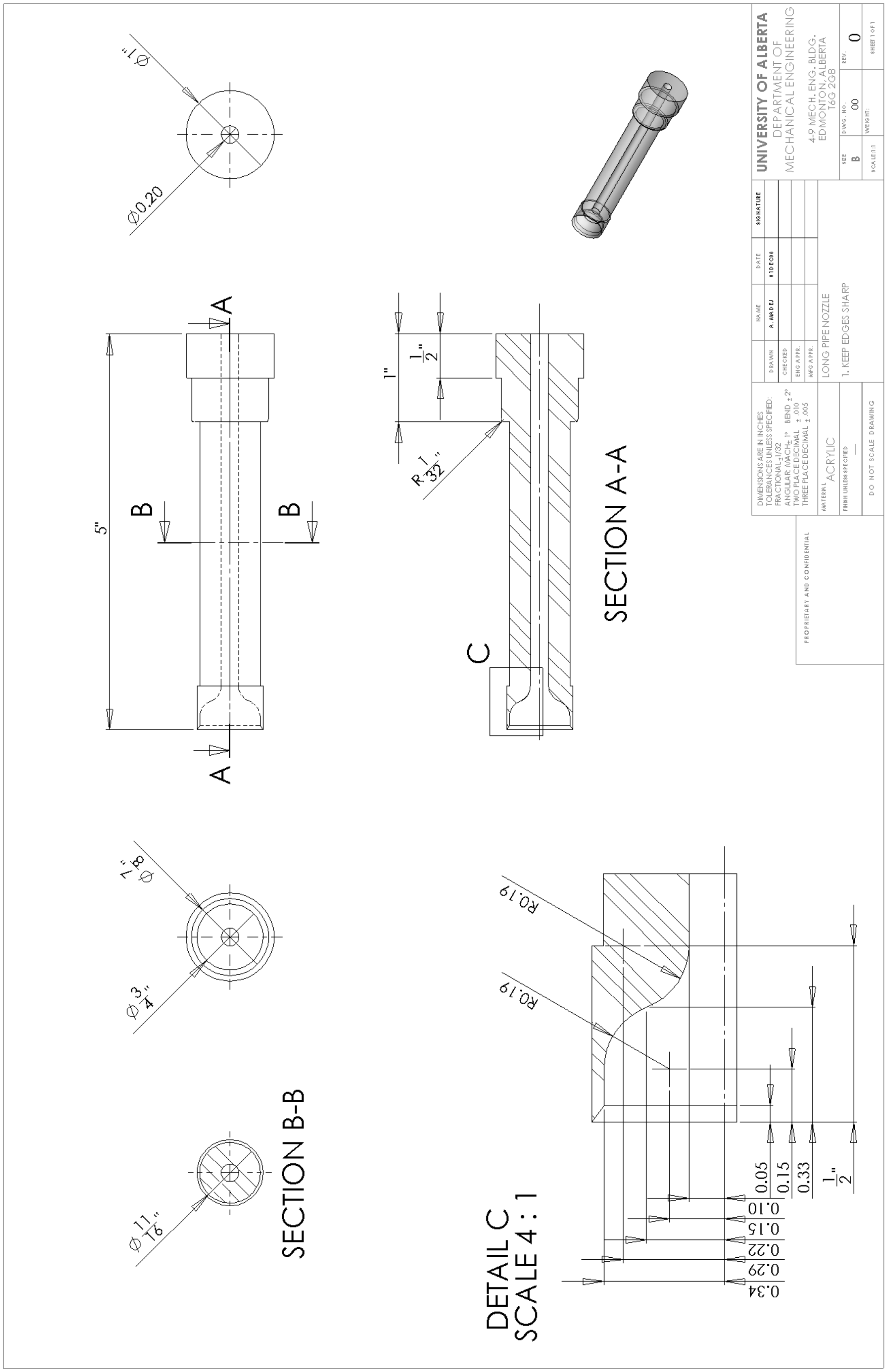

Figure C.2 Schematic drawing of long pipe nozzle.

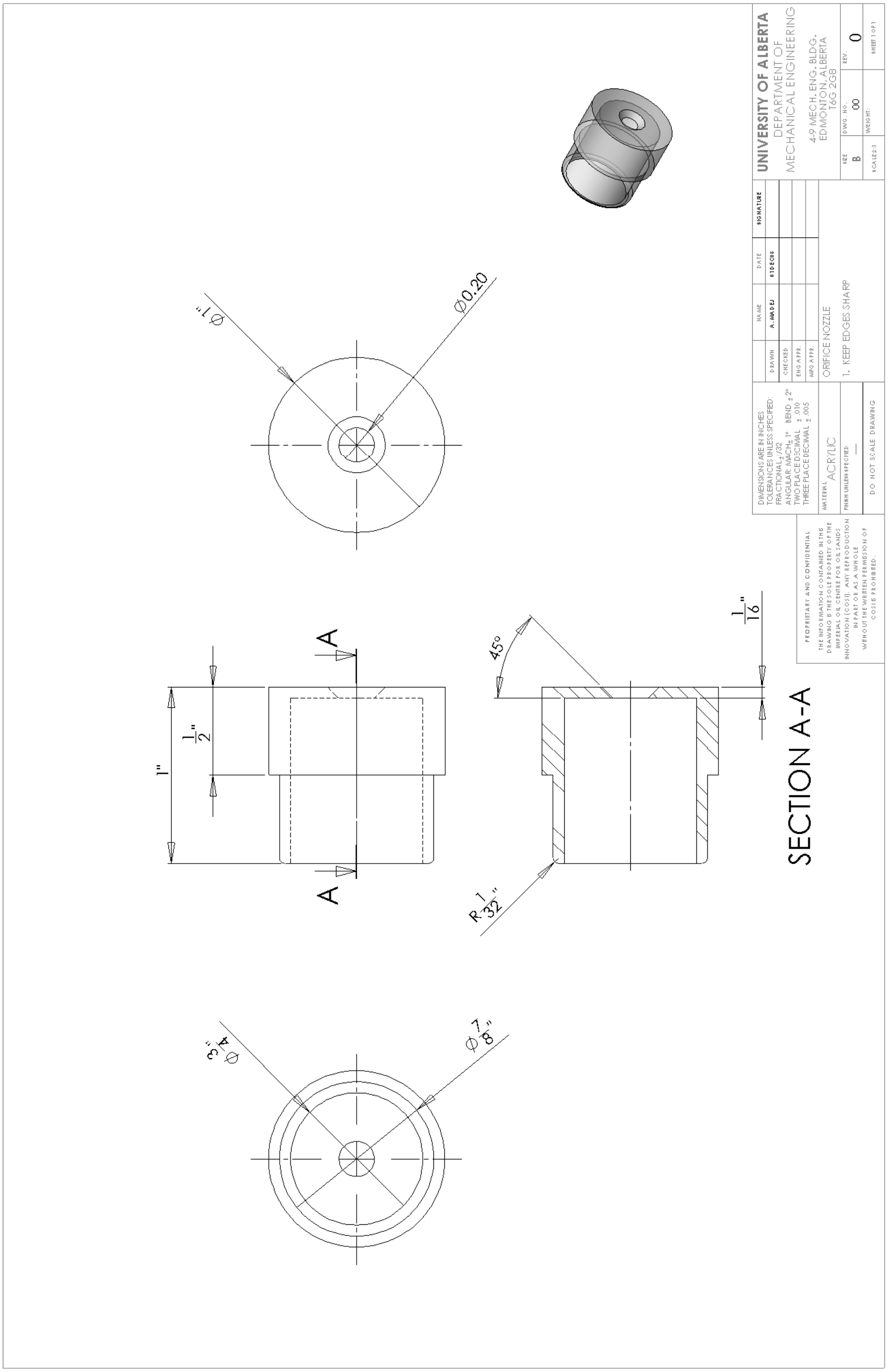

Figure C.3 Schematic drawing of orifice nozzle.

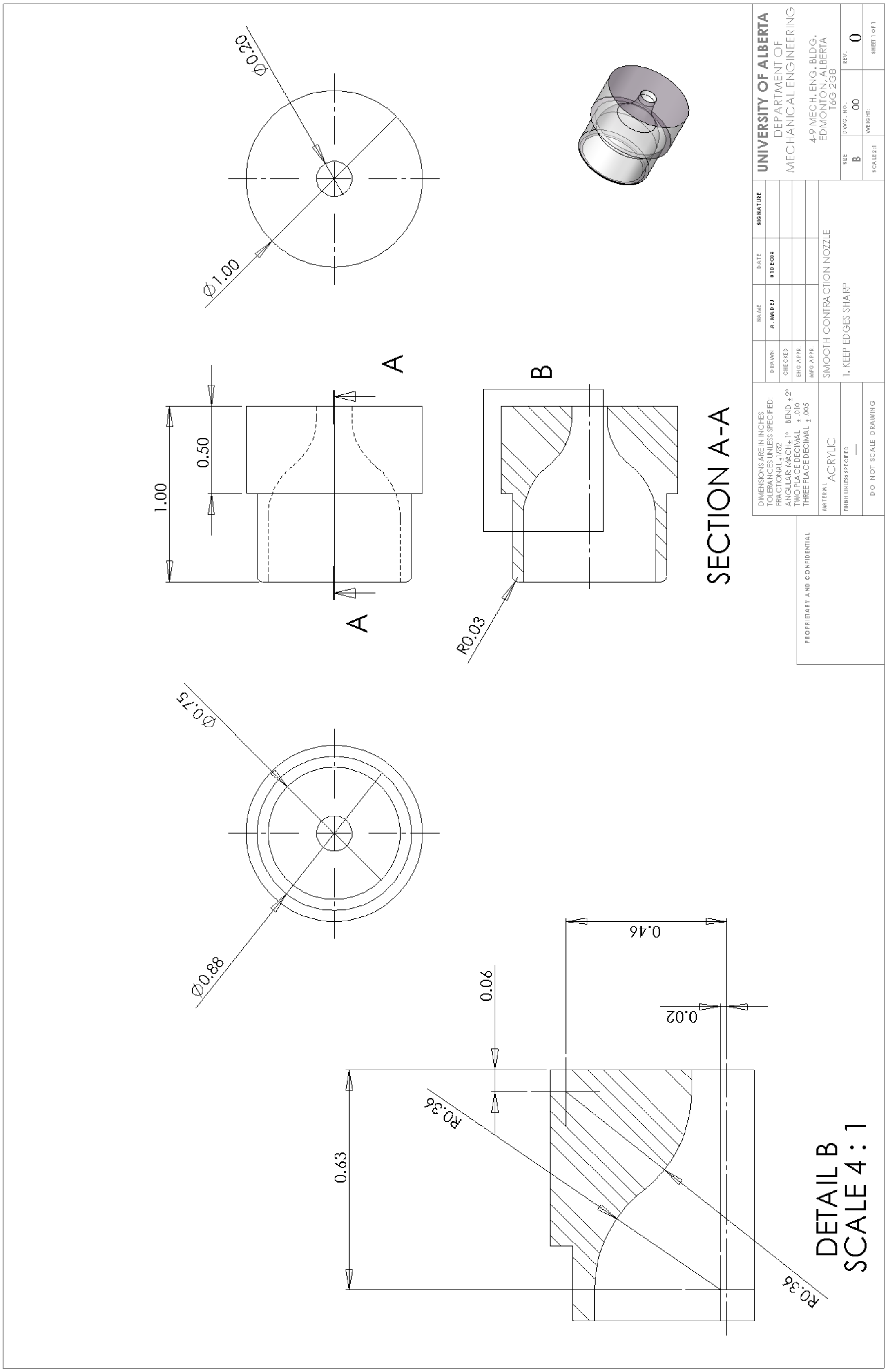

Figure C.4 Schematic drawing of smooth contraction nozzle.

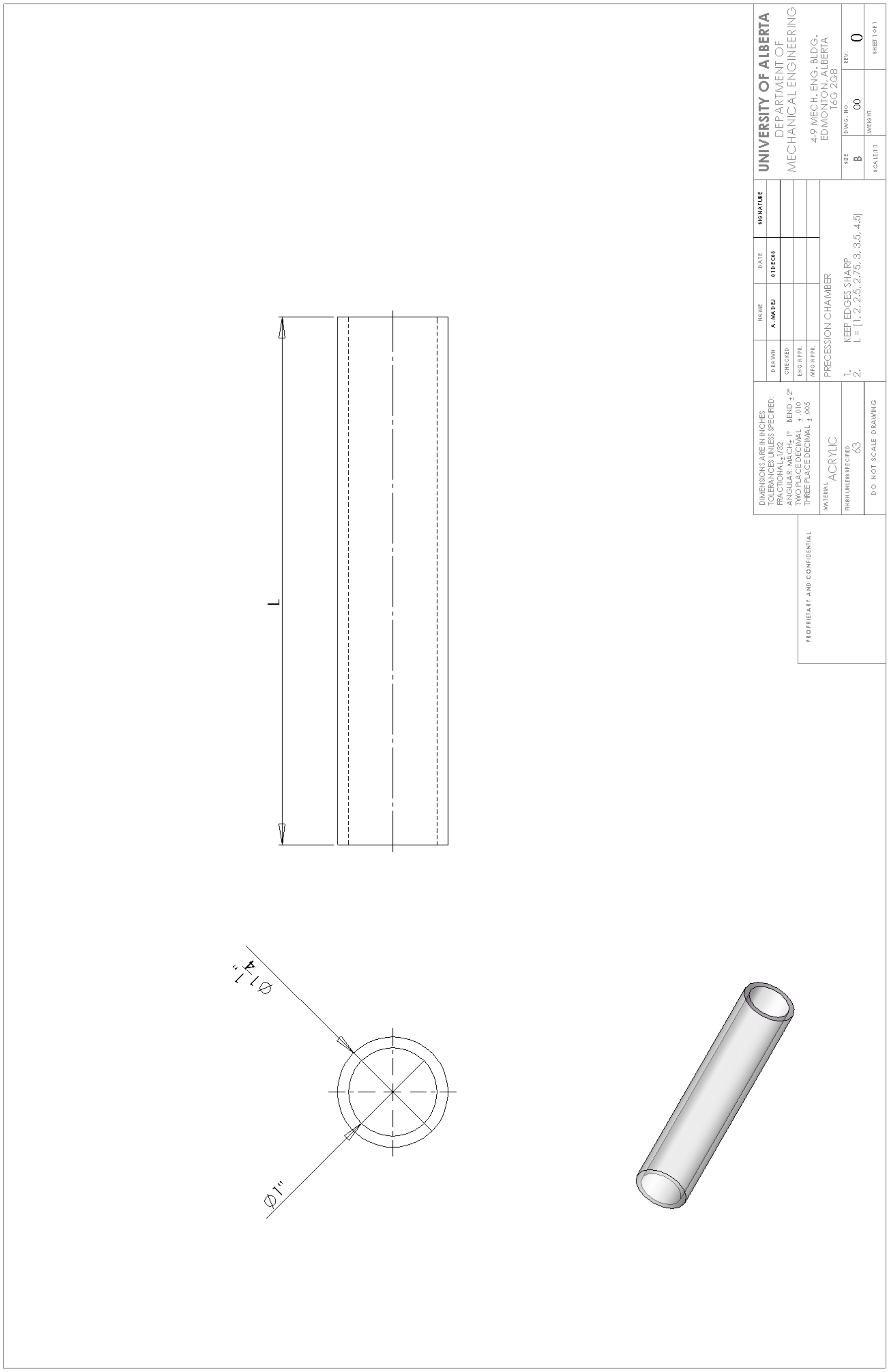

Figure C.5 Schematic drawing of the precession chamber.

APPENDIX D: CENTERLINE VELOCITY DECAY AND HALF SPREAD PROFILES

Dimensionless centerline velocity decay profiles determined for the jets generated with the long pipe, orifice, and smooth contraction nozzles are presented in this appendix. Figure D.1, Figure D.2, and Figure D.3 show the centerline velocity decay profiles for the long pipe, orifice, and smooth contraction nozzles, respectively, at all Reynolds numbers studied. Figure D.4, Figure D.5, and Figure D.6 show the jet half-spread profiles for these nozzles in that same order.

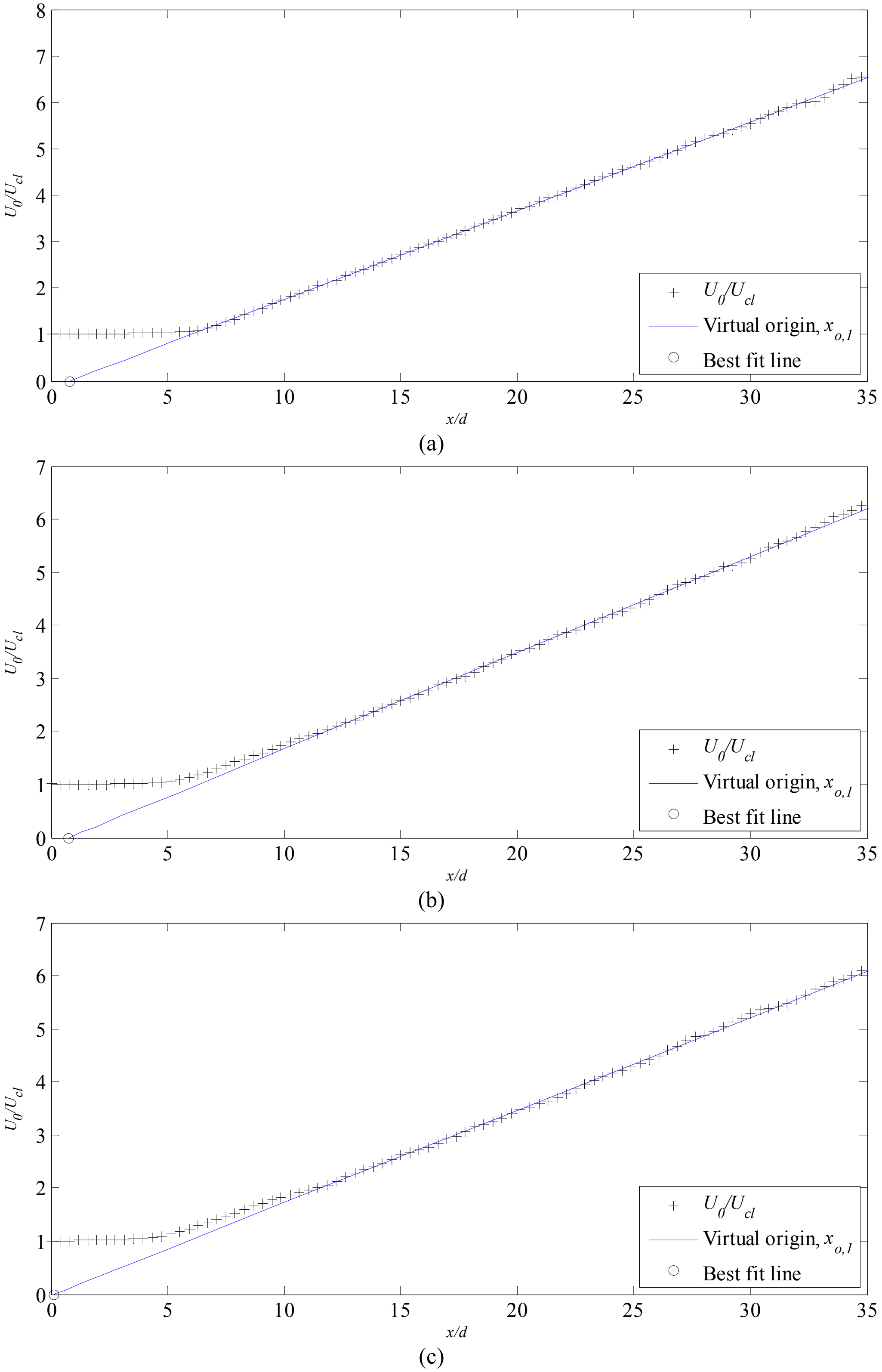

Figure D.1 Nondimensionalized centerline velocity decay profiles for the long pipe nozzle at Reynolds numbers of: (a) 5,800, (b) 10,000, (c) 21,800, (d) 32,400, (e) 50,700, (f) 61,900.

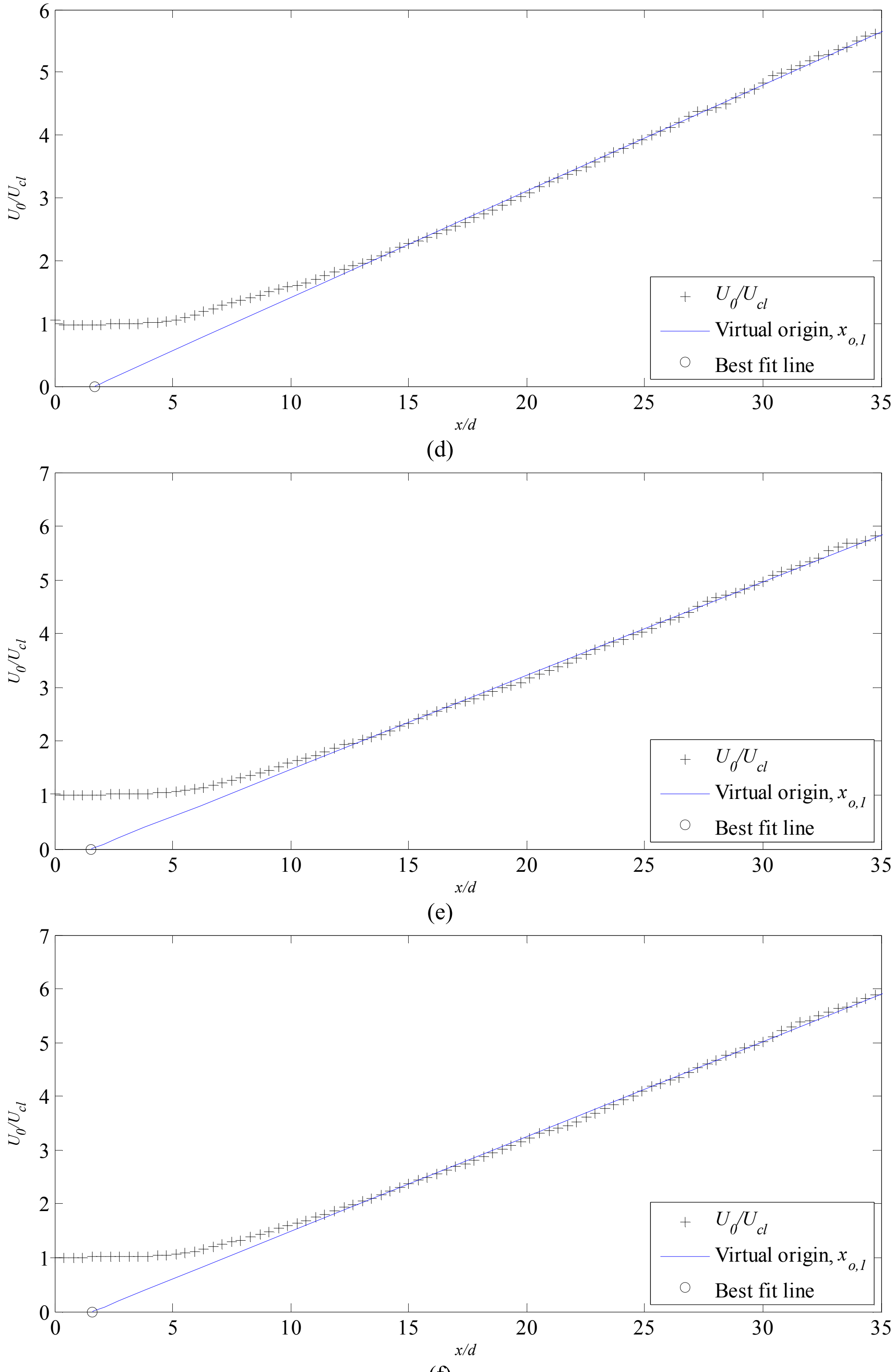

(d)

(e)

(f)

Figure D.1 Nondimensionalized centerline velocity decay profiles for the long pipe nozzle at Reynolds numbers of: (a) 5,800, (b) 10,000, (c) 21,800, (d) 32,400, (e) 50,700, (f) 61,900.

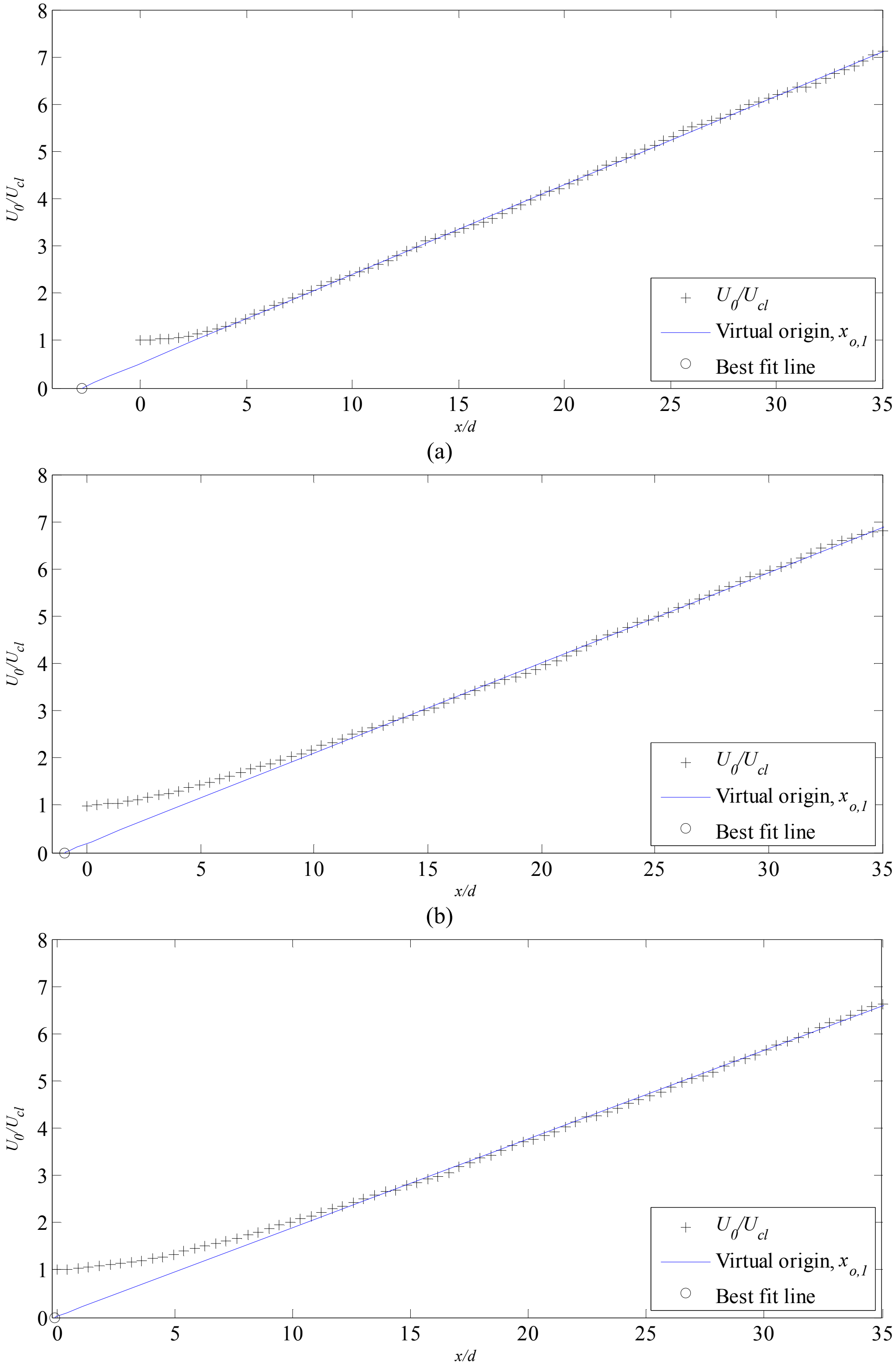

(a)

(b)

(c)

Figure D.2 Nondimensionalized centerline velocity decay profiles for the orifice nozzle at Reynolds numbers of: (a) 5,800, (b) 10,000, (c) 21,800, (d) 32,400, (e) 50,700, (f) 61,900.

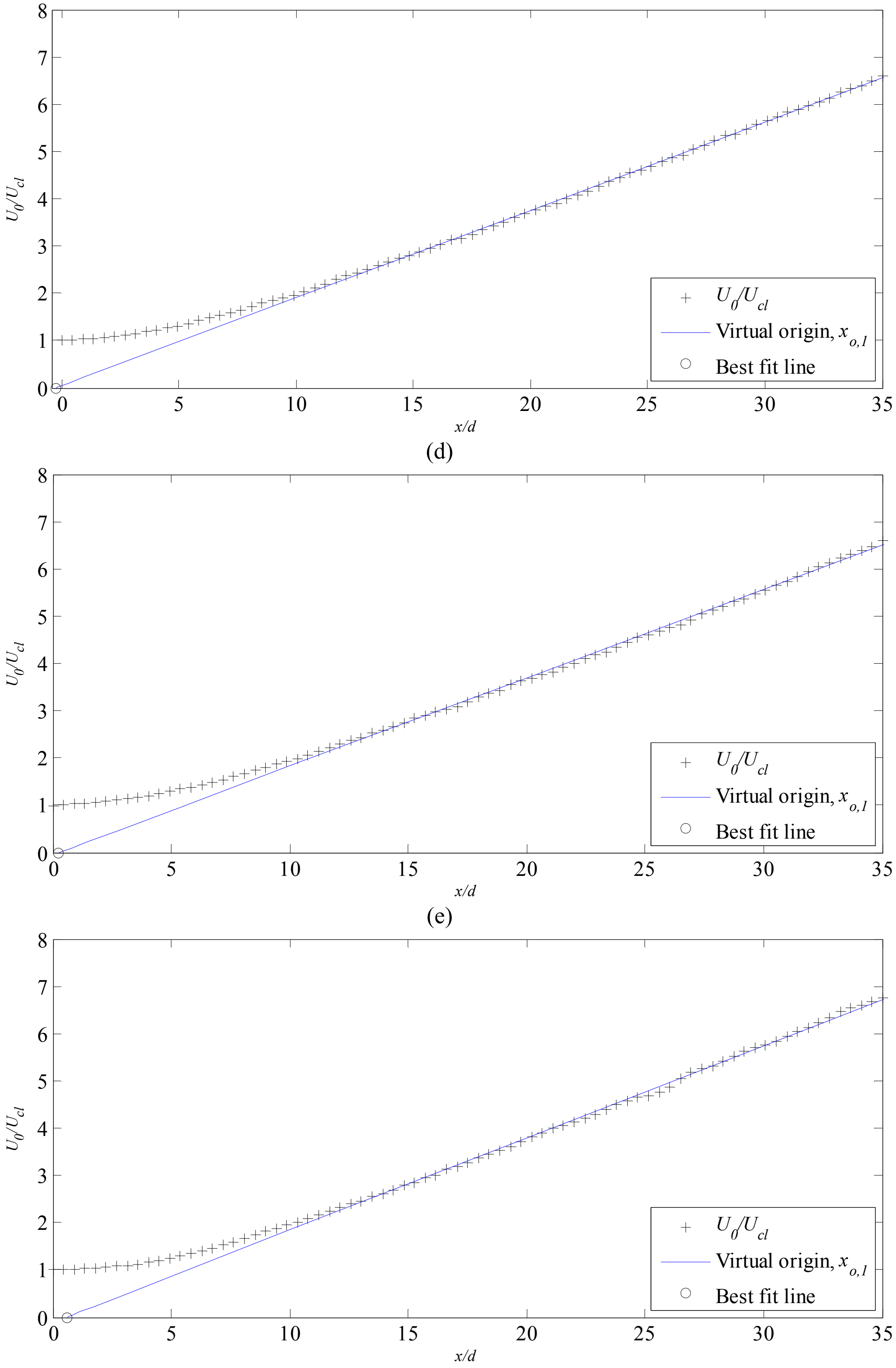

(d)

(e)

(f)

Figure D.2 Nondimensionalized centerline velocity decay profiles for the orifice nozzle at Reynolds numbers of: (a) 5,800, (b) 10,000, (c) 21,800, (d) 32,400, (e) 50,700, (f) 61,900.

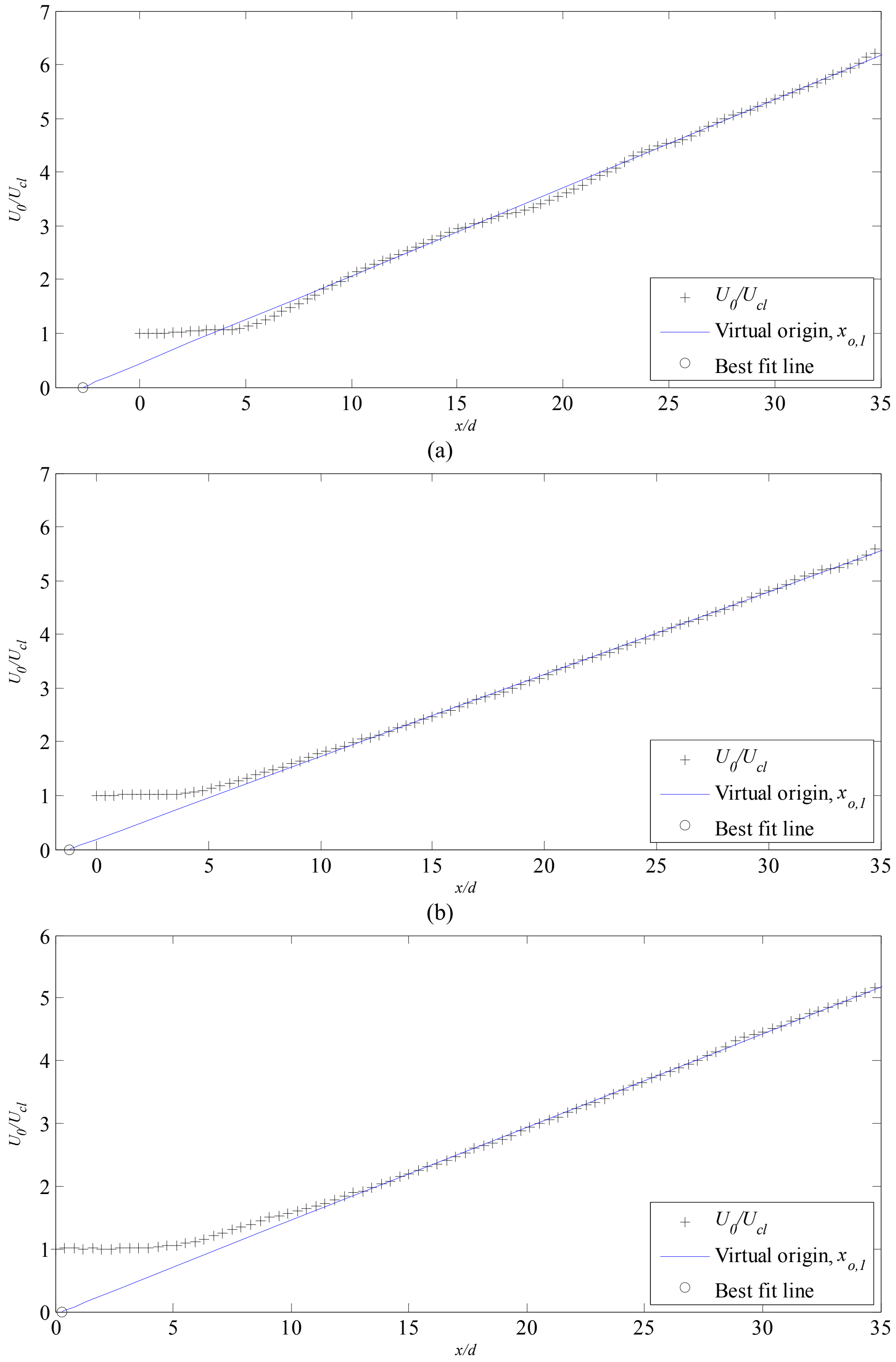

(a)

(b)

(c)

Figure D.3 Nondimensionalized centerline velocity decay profiles for the smooth contraction nozzle at Reynolds numbers of: (a) 5,800, (b) 10,000, (c) 21,800, (d) 32,400, (e) 50,700, (f) 61,900.

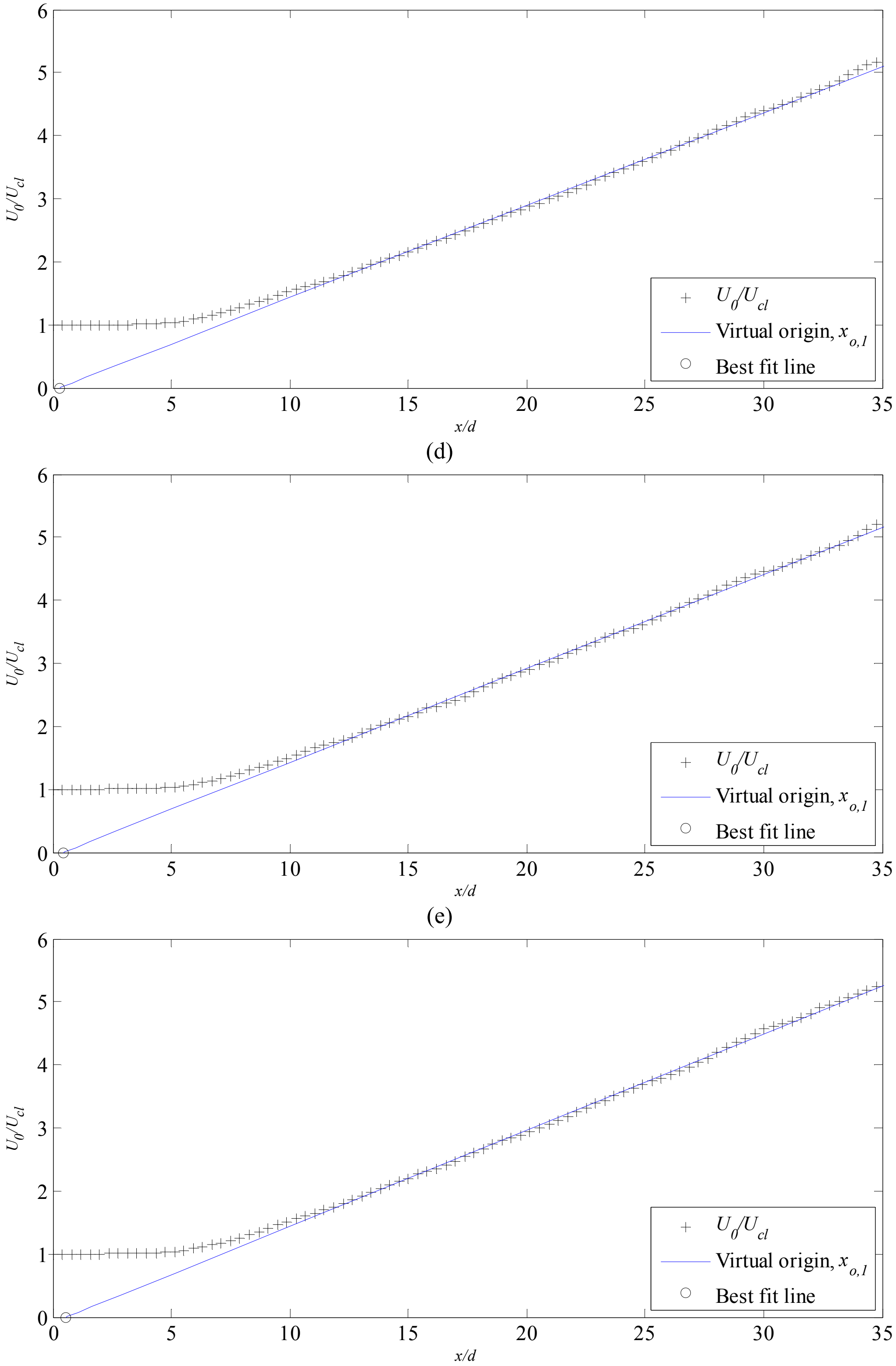

(d)

(e)

(f)

Figure D.3 Nondimensionalized centerline velocity decay profiles for the smooth contraction nozzle at Reynolds numbers of: (a) 5,800, (b) 10,000, (c) 21,800, (d) 32,400, (e) 50,700, (f) 61,900.

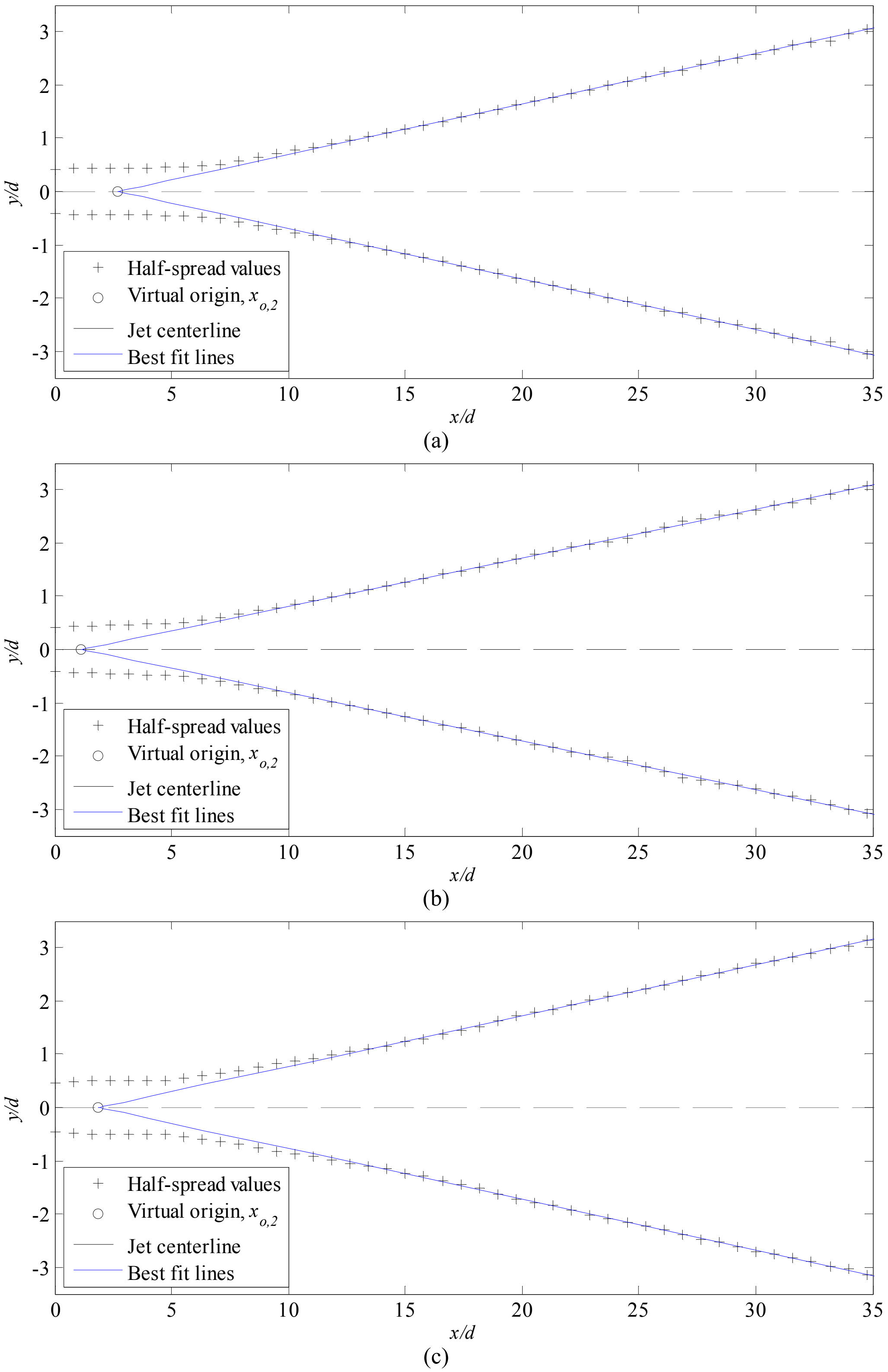

Figure D.4 Half-width profiles for the long pipe nozzle at Reynolds numbers of: (a) 5,800, (b) 10,000, (c) 21,800, (d) 32,400, (e) 50,700, (f) 61,900.

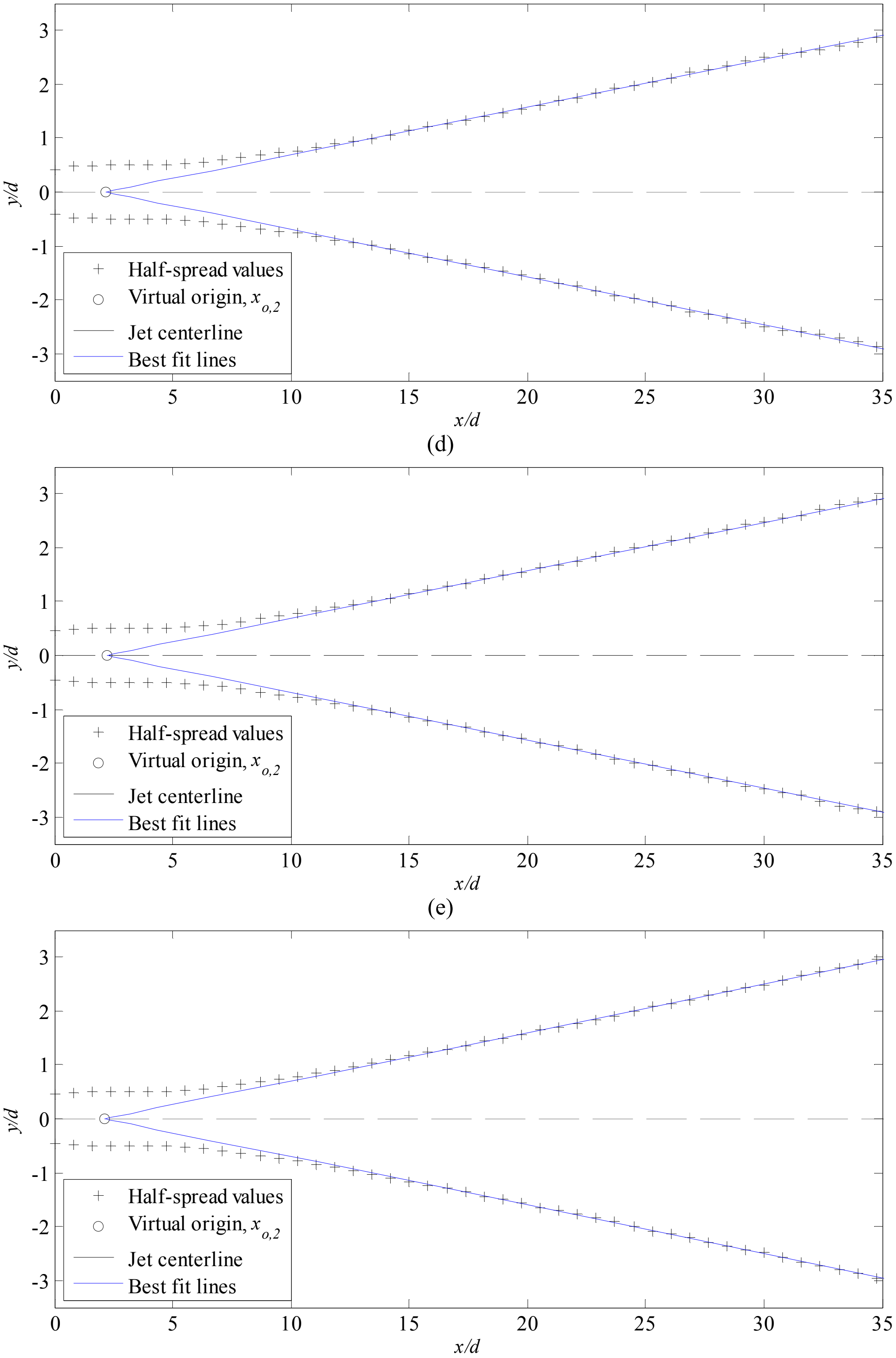

(d)

(e)

(f)

Figure D.4 Half-width profiles for the long pipe nozzle at Reynolds numbers of: (a) 5,800, (b) 10,000, (c) 21,800, (d) 32,400, (e) 50,700, (f) 61,900.

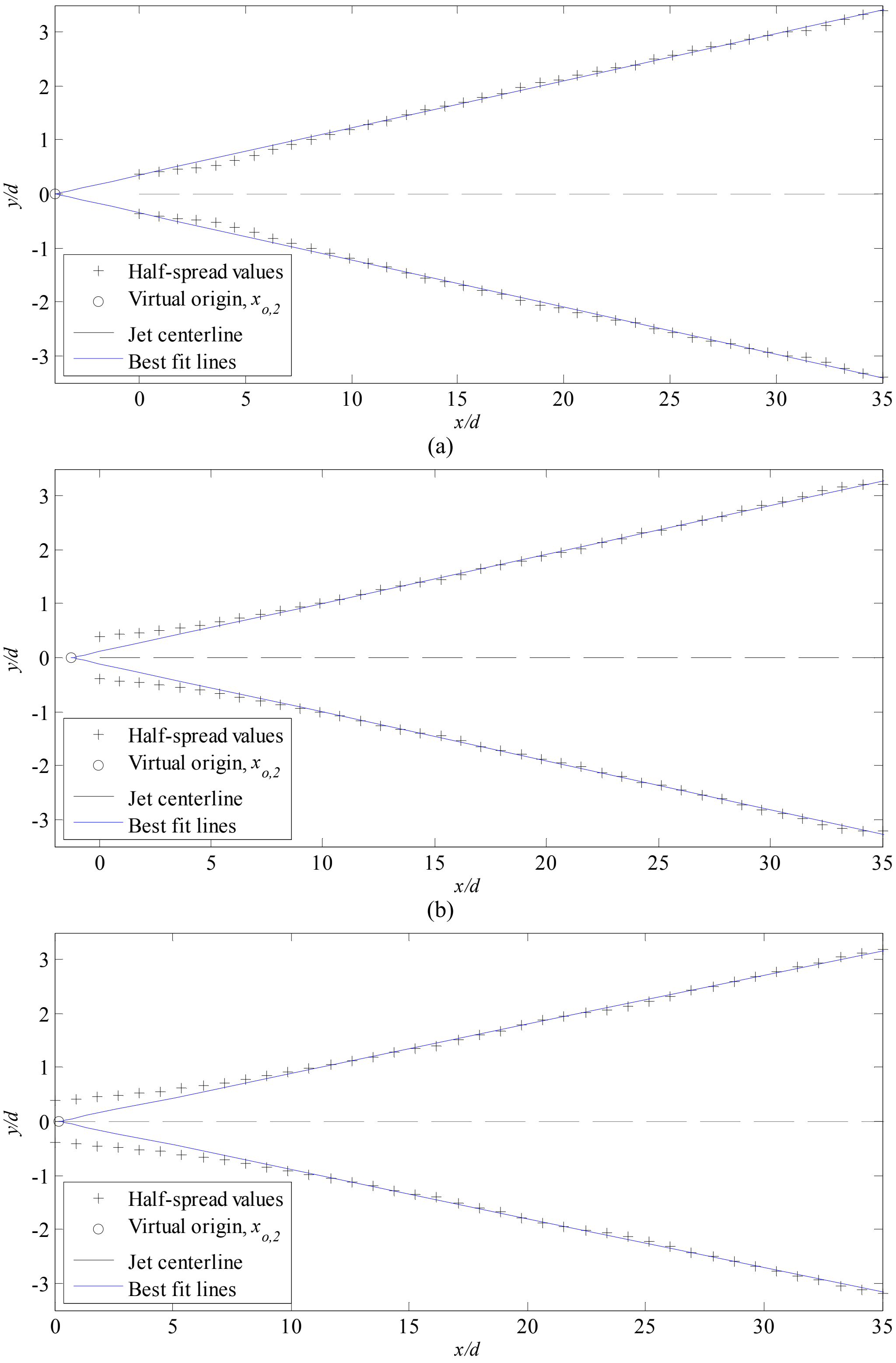

Figure D.5 Half-width profiles for the orifice nozzle at Reynolds numbers of: (a) 5,800, (b) 10,000, (c) 21,800, (d) 32,400, (e) 50,700, (f) 61,900.

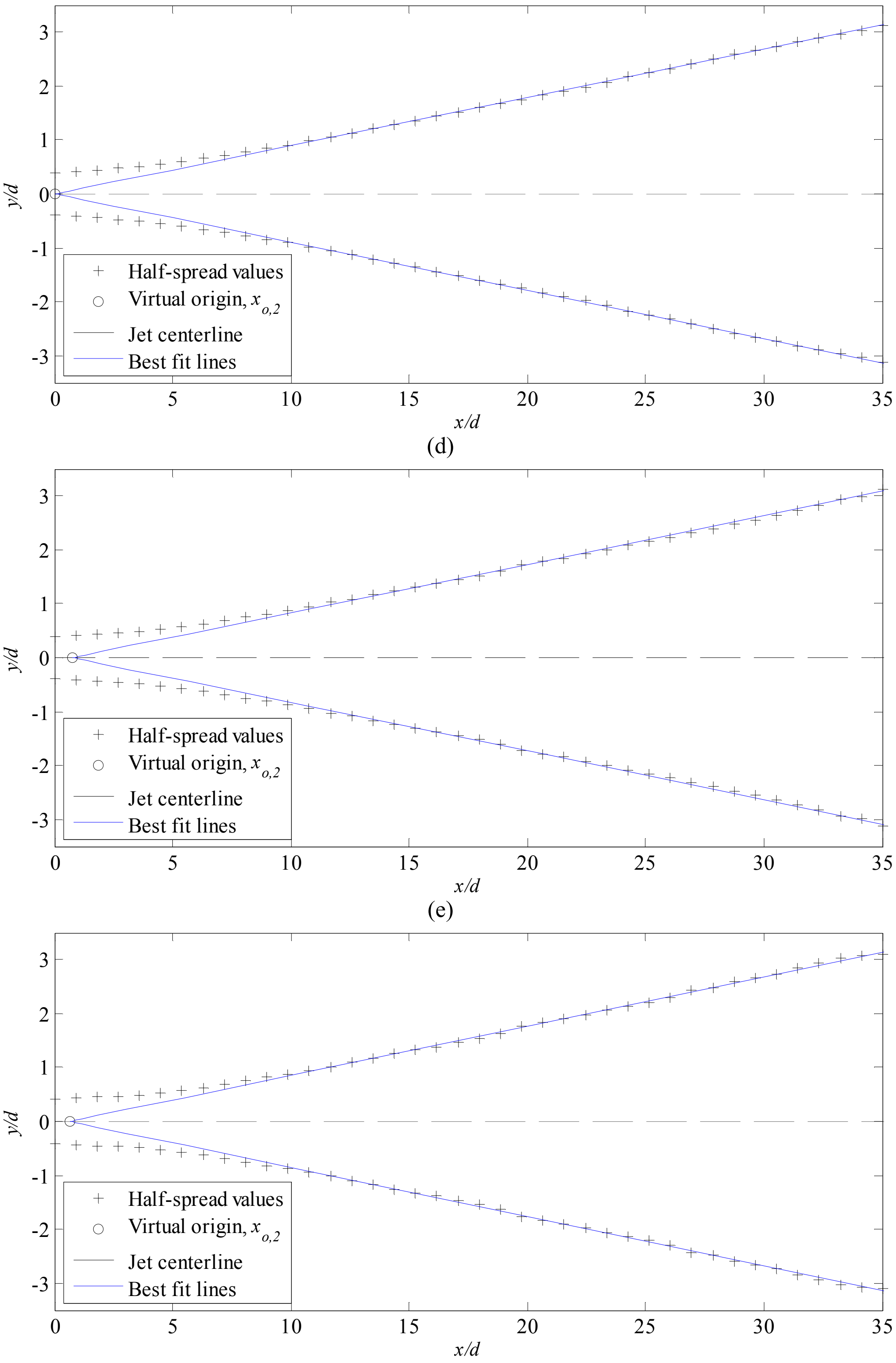

(d)

(e)

(f)

Figure D.5 Half-width profiles for the orifice nozzle at Reynolds numbers of: (a) 5,800, (b) 10,000, (c) 21,800, (d) 32,400, (e) 50,700, (f) 61,900.

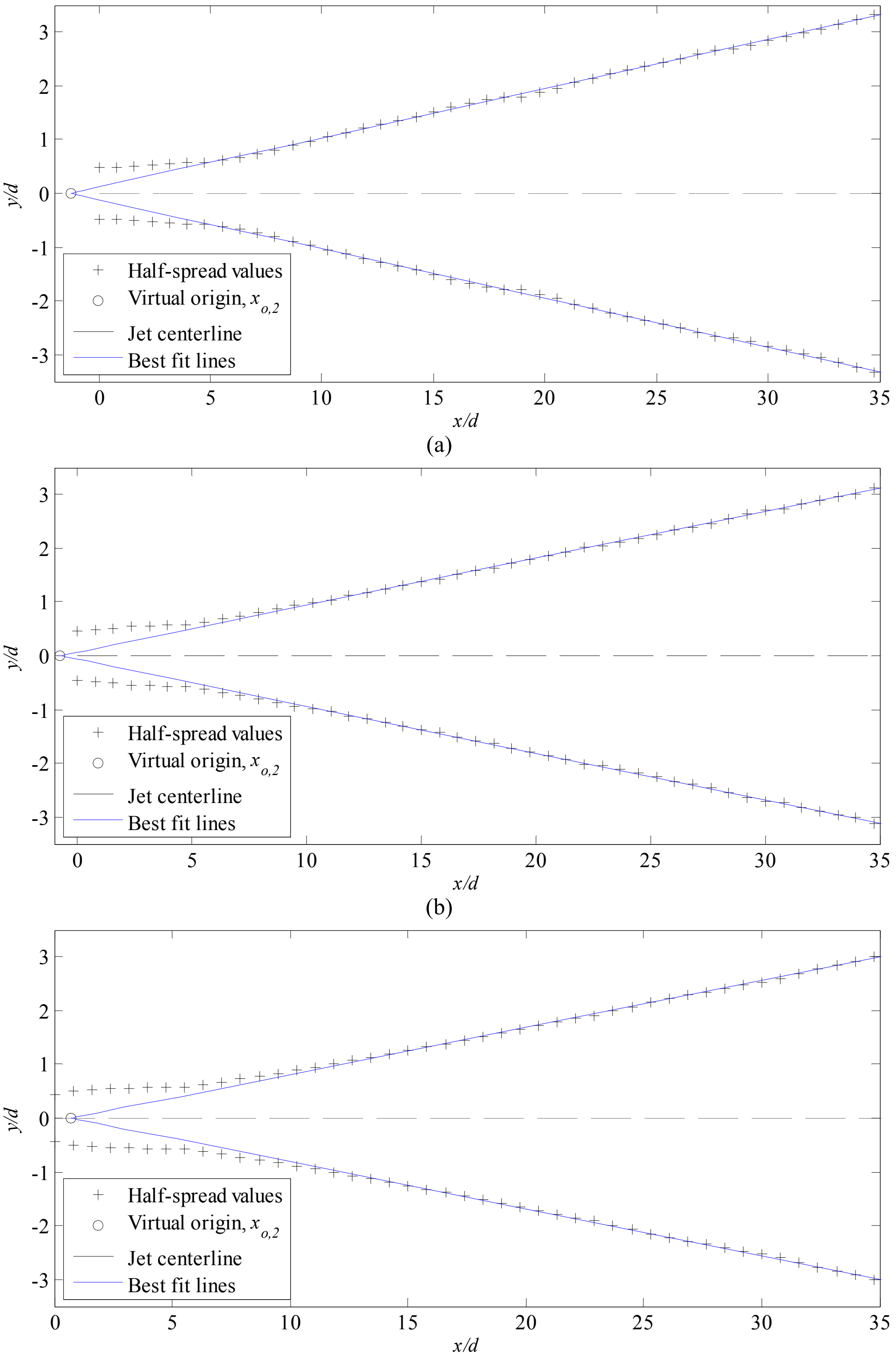

(a)

(b)

(c)

Figure D.6 Half-width profiles for the smooth contraction nozzle at Reynolds numbers of: (a) 5,800, (b) 10,000, (c) 21,800, (d) 32,400, (e) 50,700, (f) 61,900.

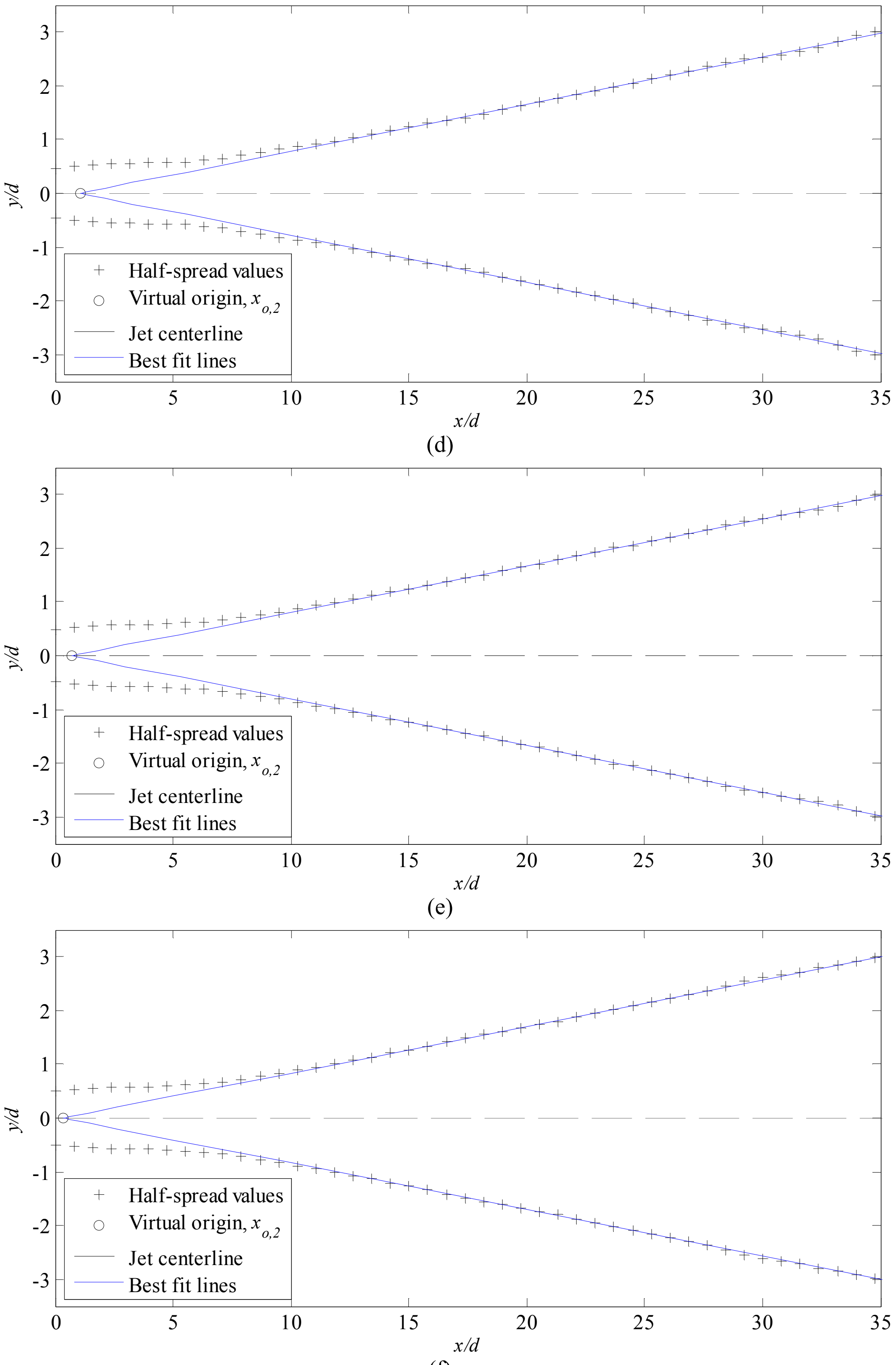

(d)

(e)

(f)

Figure D.6 Half-width profiles for the smooth contraction nozzle at Reynolds numbers of: (a) 5,800, (b) 10,000, (c) 21,800, (d) 32,400, (e) 50,700, (f) 61,900.